The Mechanical Alloying of Aluminum and Zirconium

Thesis by
Zezhong Fu

In Partial Fulfillment of the Requirements
for the Degree of
Doctor of Philosophy

California Institute of Technology
Pasadena, California
1993
(Submitted October 14, 1992)

To my parents, my husband and my little daughter

Acknowledgments

Studying at Caltech has been one of the most important and most memorable experiences in my life. I would like to acknowledge many people for their instruction, help, support, and friendship during my stay at Caltech.

First and foremost, I would like to express my deep appreciation to my advisor, Bill Johnson, for providing me the opportunity to study in his group and for creating such an exciting environment for doing research. Bill has taught me new ways to think about materials science and the techniques used to study it. I am grateful to Bill for his creative ideas, his guidance, his enthusiasm, his support, and his encouragement throughout my graduate study. These were invaluable to me. I am especially indebted to Bill for his patience in critical reading, proofing and editing of my thesis.

I have benefited greatly from the courses offered by Dr. B. Fultz and Dr. C. Ahn. I owe special thanks to C. Garland for teaching me how to operate the TEM 430 and for assisting me in the analysis of TEM pictures. I gratefully acknowledge carol's help and friendship.

I would also like to thank Dr. H. J. Fecht and Dr. R. Birringer for many stimulating discussions and for extensive advice. Hans and Rainer have some direct contributions to this thesis.

Certainly many thanks must go to my officemate Dr. C. E. Krill III. Chuck has helped me in many ways, not only scientifically, but also in language, writing and cultural adjustments. I have been a stranger in a strange land. Chuck was always willing to answer my questions in this area.

I would like to thank the past and present members of the Johnson group, especially Dr. E. J. Cotts, Dr. E. Hellstern, G. Han, Y. Abé, D. S. Lee, Dr. J. Eckert, Dr. J. Holzer, Mo Li, A. Peker, and J. Li, for research collaborations and discussions, and for making my stay in the group more meaningful. I would also like to thank Dr. C.-J. Tsai, Z. Gao, L. Anthony, and Dr. H. Ouyang, for their help and friendship.

I am deeply grateful to my former research advisor, Prof. Muyu Zhao (Jilin University, China), for introducing me to scientific research, and for his continual encouragement.

My special thanks go to Qiang, Xiaoming, Mei and Yuhua for their friendship and invaluable assistance as my best friends.

Finally, I want to thank my parents and my husband Yuejin, for their love, constant support and encouragement. I thank my little daughter, Audrey, for making my life more colorful.

Abstract

Over the last several years, mechanical alloying/milling (MA/MM) process has been applied to produce different types of metastable or non-equilibrium materials such as metallic glasses, quasi-crystalline materials, nanocrystalline metals, compounds and supersaturated solid solutions. It appears that MA offers greater latitude in controlling the microstructure than other non-equilibrium processing methods such as rapid solidification. Despite a considerable number of experiments using MA/MM, many questions regarding the mechanisms of phase transformations induced by MA, especially the mechanism of amorphization, remain to be answered. In this thesis, the sequence of phase transformations induced by the mechanical alloying of aluminum and zirconium has been studied. The structural analysis indicated that none of the thermodynamically stable intermetallic compounds found in the phase diagram are formed during MA of the Al-Zr system. Instead, the nanocrystalline supersaturated α-Zr solid solution and amorphous phase are synthesized depending on the initial composition of the powder mixture. The thermodynamic and structural properties of these ball-milled materials have been characterized by x-ray diffraction (XRD), transmission electron microscopy (TEM) and differential scanning calorimetry (DSC).

As we know, one of the crucial aspects of nanophase and amorphous phase materials is the stability against grain growth and crystallization. In Chapter 4, the metastability of nanocrystalline materials based on the thermodynamics and grain boundary segregation arguments proposed by Johnson has been discussed. The thermal stabilities of the nanostructured

α-Zr solid solutions and amorphous materials have also been studied. The experiments found that the grain size of nanocrystalline supersaturated solid solution is stable under heat treatment until reaching a temperature where the crystallization of an equilibrium compound phase occurs.

In Chapter 5, the temperature effects on the mechanical alloying of Al and Zr have been studied by milling at different ambient temperatures. The experiments reveal that the ultimate grain size of nanostructured materials prepared by ball milling is determined by two main factors. One is densities of structural defects which depends on the competition between the severe plastic deformation induced by MA and the recovery behavior of the materials. Another is chemical effects which are related to the composition of the sample and the interactions among the components. Obviously, the recovery or relaxation behavior is temperature dependent, so the milling temperature could influence the average grain size. The chemical effects on grain size may also change with the milling temperature. The experimental results suggest that the steady state obtained by ball milling at higher temperature is much closer to a chemical equilibrium state compared with the state formed by milling at room temperature. A faster alloying rate is obtained at higher temperature milling. This is consistent with the solid state reaction mechanism by MA.

The mechanisms of amorphizations by MA of aluminum and zirconium under different experimental conditions have been discussed in Chapter 6. The emphasis is to argue the possibility of polymorphic amorphization.

Contents

List of Figures

Chapter Two

Chapter Three

Chapter Four

Chapter Five

Chapter Six

Chapter 1

Introduction

Mechanical alloying/milling (MA/MM) was first developed by Benjamin and coworkers at the International Nickel Company in the late 1960s [1]. The technique was originally used for developing oxide dispersion strengthened superalloys, later for producing composite metallic powders and for preparing homogeneous alloyed powders with a fine, controlled structure. The process occurs by the repeated welding and fracturing of a mixture of metallic or nonmetallic powders in a highly activated ball charge. Therefore, the process is also called ball milling. During ball milling, powder particles trapped between colliding balls or between a ball and the container surface undergo severe plastic deformation, causing them to flatten, work harden, or develop modified microstructures and phases. It is clear that the greatest numbers of collision events in the milling system are of the ball-powder-ball type as shown in Fig. 1.1 [2]. These competing fracture and coalescence events continue throughout the milling processing and have been the basis for qualitative descriptions of the mechanical alloying. Fig. 1.2 [3] describes the three common devices used for the mechanical attrition. Commercial mills usually have one of these three basic configurations or the mix of them. A vertical ball mill is shown in Fig. 1.2(a), and a vibration mill is shown in Fig. 1.2(b) as a second configuration exemplified by the SPEX shaker mill. A third type is a conventional horizontal ball mill as shown in Fig. 1.2(c). Milling of metal powders produces external shapes and textural changes and internal structural

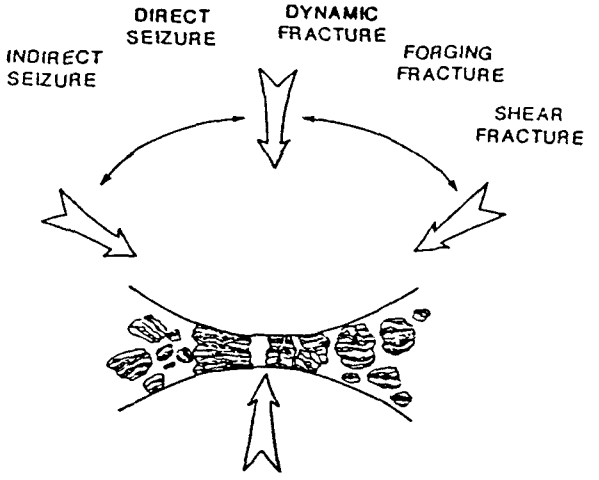

Fig. 1.1 The schematic drawing for explaining the repeated fragmentation and coalescence processes presented between two collision balls during MA.

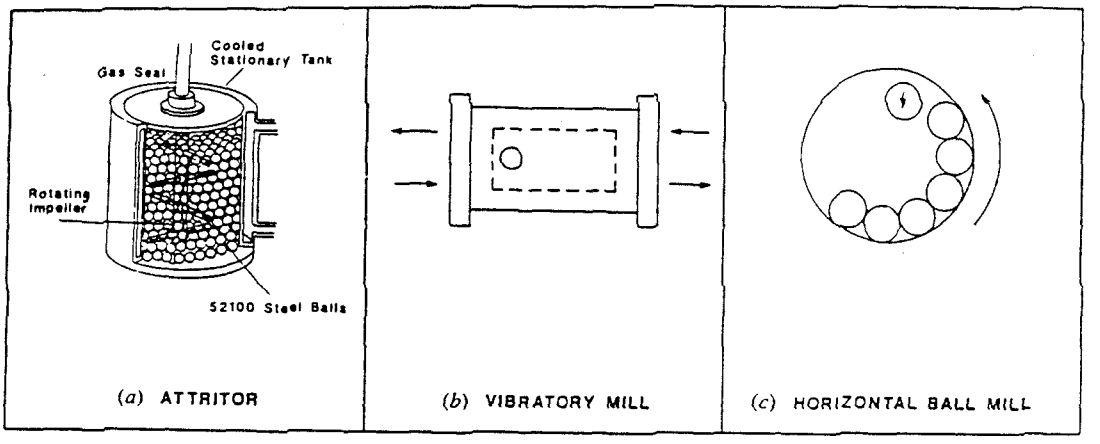

Fig. 1.2 Three common types of devices used for mechanical milling: (a) an attritor contains hardened balls which are driven by means of a central impeller shaft; (b) a vibratory mill which is examplified by the Spex shaker mill; (c) a conventional horizontal ball mill which can produce large volumes of powder.

changes. The internal structural changes could involve the reduction of crystalline grain size (down to the order of several nanometers), and the formation of amorphous phase, quasi-crystalline phase, or other metastable or non-equilibrium phases. The extent of these changes is determined mainly by milling parameters, milling environment, and physical and chemical properties of the metal or alloy being milled. These changes in turn affect the physical properties of the metal or alloy being processed.

The synthesis of an amorphous phase by mechanical alloying/milling was first reported by Yermakov *et al.* [4] for the Co-Y system. Later in 1983, Koch *et al.* [5] reported a similar but better characterized experiment on amorphous phase formation from a mixture of elemental powders of Ni and Nb with the composition $Ni_{60}Nb_{40}$. Since then, many investigations of mechanical alloying have been focused on amorphous phase formation (see Ref.[6] for a review) by ball milling of either an intermetallic compound or a mixture of elemental powders. In addition to metallic glass formation, more recently, the mechanical milling process has been applied to produce other types of metastable and non-equilibrium materials with the controlled microstructures such as nanocrystalline metals, compounds and supersaturated solid solutions [7]. It appears that mechanical alloying offers greater latitude in controlling the microstructure than other non-equilibrium processing methods such as rapid solidification. Despite a considerable number of experiments using mechanical alloying/milling, many questions regarding the mechanisms of phase transformations induced by MA, especially the mechanism of amorphization, remain to be answered [8]. In this thesis, I focus on: (1) investigating the sequence of phase transformations for the mechanically alloyed Al-Zr system and

metastable phase formation under different milling temperatures; (2) characterizing the structures and properties of these metastable phases; (3) studying the thermal stability of each metastable phase; and (4) trying to understand the mechanism of amorphization by mechanical alloying of aluminum and zirconuim.

In the introduction chapter, I will first review the fundamental concepts of stable equilibrium phases, metastable equilibrium phases and non-equilibrium phases, and then discuss the reasons why metastable or configurationally frozen phases can be synthesized through both thermodynamic and kinetic arguments. Regarding the two "metastable" phases studied in the thesis, I will introduce the nanocrystalline phase and the metallic glass phase by discussing their preparation methods, properties and applications.

1.1 Equilibrium phases and non-equilibrium phases

Every known substance exists in several different forms, called phases. A phase can be defined as a portion of the system whose properties and composition are homogeneous and which is physically and structurally distinct from other portions of the system. A simple example is water which can be a vapor phase, a liquid phase, or one of several different solid phases. Under given conditions, a given phase could be stable, metastable or unstable in terms of thermodynamics. Under the conditions of constant temperature and pressure, the relative stability of a phase is determined by its Gibbs free energy. There are two types of thermodynamic states of interest: stable and metastable. As shown in Fig. 1.3, both types require a minimum in the Gibbs free energy at constant temperature and pressure, and in both cases the properties depend only on the external variables.

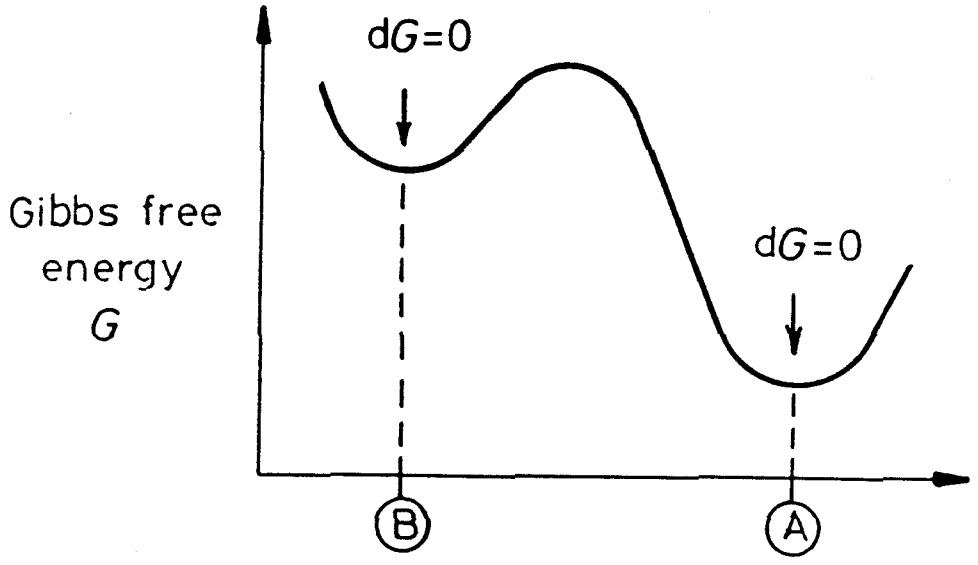

Fig. 1.3 Gibbs free energy curve with stable equilibrium state 'A' and metastable equilibrium state 'B'.

Stable equilibrium refers to the global minimum of Gibbs free energy, while metastable equilibrium refers to a local minimum. Metastable phases are stable against fluctuations, as any transition path implies an increase in free energy. This is in contrast to an unstable state, where no free energy barrier exists. In other words, although a metastable state is stable within certain limits, the metastable state may become unstable after a sufficient deviation. In principle, the system will always leave a metastable state eventually for another state which is more stable, corresponding to a greater possible maxima of the total entropy of the system and its environment. A state is unstable if its free energy can be lowered by localized homophase atomic rearrangement. Therefore, a thermodynamic equilibrium state is defined as a state that a system attains spontaneously under a set of external constraints which are assumed to be constant in time and space. In equilibrium, the system will consist of one or more homogeneous regions, which exhibit no gradients in temperature, concentration or other variables, and no transients. Another important state is called a configurationally frozen state which has properties that depend on history as well as internal energy of the system. Its properties are independent of time under certain conditions, and therefore a frozen state is often called a false equilibrium state. A system in truly metastable equilibrium would not have access to any state of lower free energy by means of a continuous structural change. A good example of such systems is a fully relaxed amorphous phase in which transformation to a lower-free-energy crystalline microstructure can commence only with a discrete nucleation event. A truly metastable equilibrium phase must transform to an equilibrium phase by a first order phase transformation since such a transformation always involves an energy barrier for the

system to leave the metastable state. Some systems (not the truly metastable phases) are actually thermodynamically unstable but are configurationally frozen. They become so-called metastable microstructures. A good example of such systems is a very rapidly quenched material. The structure is "frozen" by rapidly bringing the material into a condition in which the kinetic rearrangements are too sluggish for the long-range-ordered crystal structure to be produced. Some unstable phases have technologically useful lifetimes because they are at a sufficiently low temperature to be configurationally frozen. Types of configurationally frozen metastable structures have been classified by D. Turnbull[9] as compositional, structural and morphological. The degree of metastability is characterized by the free energy excess of the system over that of the equilibrium state. Thus, metastability is measured relative to the stable phase. It seems easy to define the difference between metastable and unstable frozen phases in thermodynamics, but it is often hard to distinguish the two for a system in the real world.

Metastable metallic phases are common elements of today's technology, though not always apparent. Many modern high performance materials such as steel products or aluminum alloys for aeronautical applications are in the form of metastable rather than stable phases. The reason for the extensive use of metastable phases rest in the fact that they provide an extended range of properties compared to that available for stable phases or even show some unique properties. Novel products including metallic glass and nanocrystalline materials are the prominent examples of metastable materials. Metastable or configurationally frozen phases, however, are not well understood compared with stable equilibrium

phases. As we know, a phase diagram is a graphical representation of the equilibrium stable phases when a system is established under a given set of conditions (fixed external variables). While phase diagrams are abundantly used in metallurgy, physics, chemistry, materials science, and technology, they generally do not include information on metastable phases. Moreover, the formation of metastable phases depends on not only thermodynamics but also the kinetics. Therefore, it is interesting and necessary to investigate a given system towards finding the proper processing methods and possible metastable products by direct experiments.

Figure. 1.4 [10] has been used for describing transformation from a metastable crystal to a glass phase by considering free energy relationship and time scales. With this schematic illustration, one can understand, in general, the fundamental principle of metastable phase formation. In Fig. 1.4, labels I, M and F represent initial state, metastable state and stable equilibrium state respectively. G is Gibbs free energy of a system and τ is the time scale for the transition process. The thermodynamic conditions are $G_I > G_M > G_F$, so the driving force for the metastable phase transition is provided. To avoid the metastable phase transforming to the final stable phase in a given time, the time scale $\tau_{M\to F}$ must be longer than $\tau_{I\to M}$. Naturally, it is also possible for the initial state to transform directly to the final stable state since a greater driving force exists for this path. Therefore, the time scale $\tau_{I\to F}$ must be longer than $\tau_{I\to M}$ as well. Thus, to obtain a metastable phase, both thermodynamic conditions and kinetic constraints are required.

Fig. 1.5 shows another case in which the initial state has lower Gibbs free energy than the final metastable state. Labels I, M and F represent the

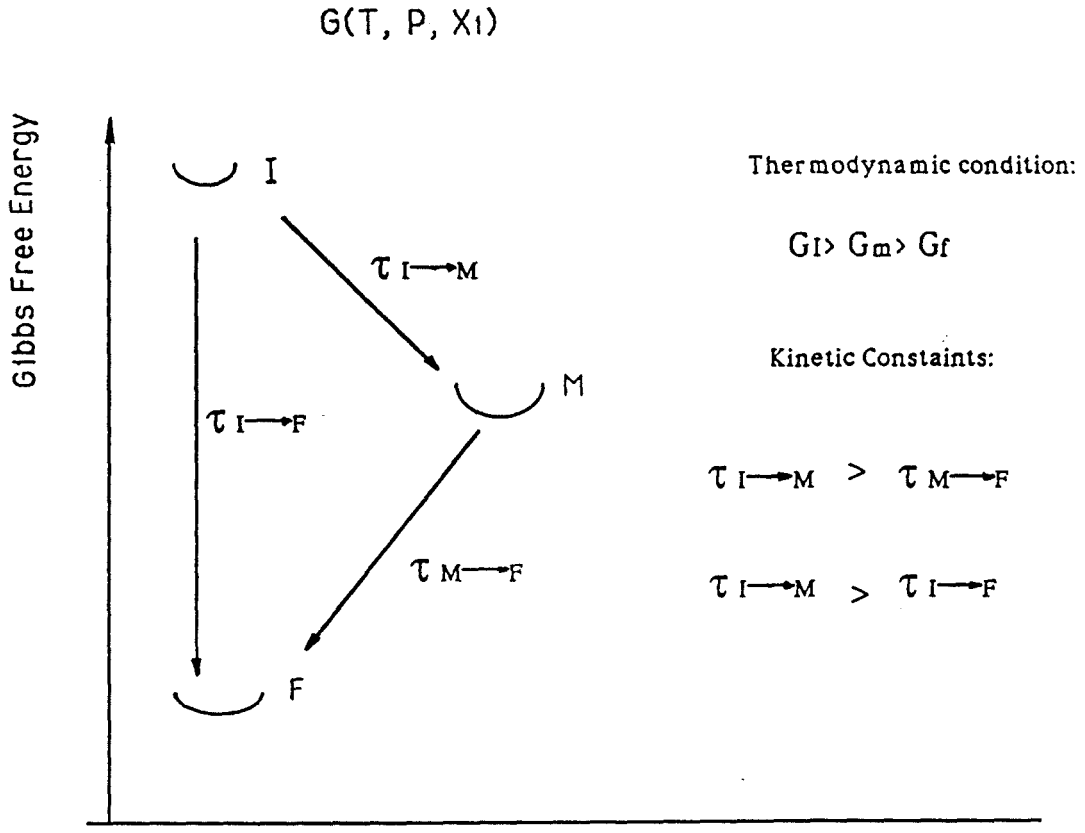

Fig. 1.4 Schematic diagram illustrating the relative free energy relationship and time scales to show the thermodynamic and kinetic conditions for a metastable phase transformation.

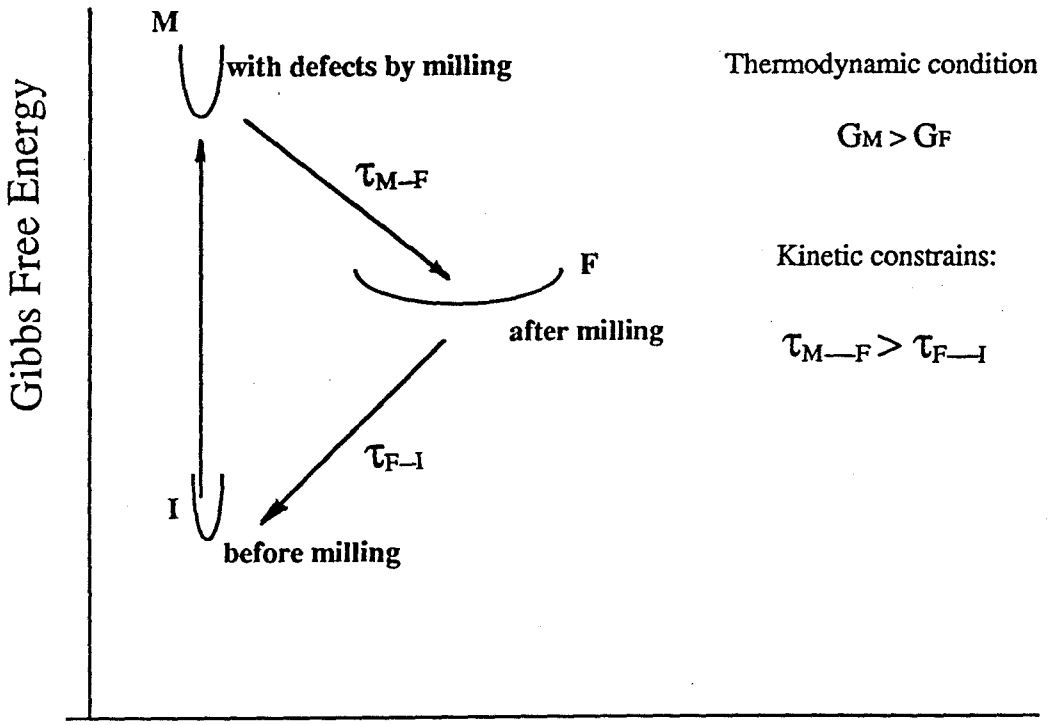

Fig. 1.5 Schematic Gibbs free energy depicting the amorphization of a stable intermetallic compound by the non-equilibrium processes such as ion-irradiation or mechanical milling.

initial crystalline state, intermediate state with higher energy and final metastable state respectively. Forming a final metastable phases first involves increase in the energy of the crystal phase by the addition of some externally provided energy (such as high-energy ball milling or ion irradiation), and the storage of this energy in the crystal. The second event is the actual loss of the initial crystalline structure thereby a highly energized material achieves a lower free energy state by transforming to a different atomic structural arrangement, for instance, an amorphous phase. In short, the path described in Fig. 1.5 involves an increase in the energy of the pre-existent crystal to the point at which it becomes unstable with respect to the final metastable state. This path is believed to pre-dominate in the cases such as irradiation-induced amorphization and mechanical deformation of an intermetallic compound.

On the basis of the above discussions, it is quite clear why metastable phases can be synthesized. How a metastable phase actually transforms, i.e., the mechanisms of the phase transition is not yet understood for processes such as mechanical alloying. In this study, the nanocrystalline solid solution and metallic glass phases have been synthesized by MA. The mechanisms of amorphization and nanophase formation under different experimental conditions are discussed. In the following two sections, I would like to review the preparation methods, the structures, and the properties of nanostructured materials and metallic glasses.

1.2 Nanocrystalline materials

During the last decade, increasing interest has focused on a so-called nanocrystalline material which is a new category of solids first suggested by Gleiter[11]. Nanocrystalline solids are polycrystals, but the crystalline grain

size is in the order of nanometers (typically 5 to 25 nm). Due to the small grain size, a large fraction of the atoms in the material (sometimes 50% or more) are located at incoherent interfaces between crystals of different orientations. Among the atoms in nanophase materials, a significant fraction are associated with grain boundaries. The contribution of boundaries to the properties is thus greatly enhanced for nanocrystalline materials. The grain size itself can also affect the properties significantly. Therefore, the properties of nanostructured materials are affected not only by their reduced grain-size scale, but also by the nature of their grain boundary structures. A novel atomic structure can be expected to exhibit novel properties since the properties of solid materials depend on their atomic structure. Nanocrystalline solids exhibit an atomic structure which differs from either conventional large grain polycrystalline solids or from metallic glasses. In fact, some properties of nanocrystalline solids have been found to differ (sometimes by a few orders of magnitude) from those of glasses or crystals with the same chemical compositions (for review papers, see [12, 13,14,15,16]). It is worth while to note that many earlier experiments on nanophase solids produced by the gas condensation method indicated that the density of nanocrystalline materials varies between 75% and 90% of the density of conventional coarse-grained phases[14]. For example, the density of nanocrystalline Pd with 9 nm grain size is only 90% of that of polycrystalline Pd. Therefore, the property differences between nanophase materials and normal polycrystalline materials may be partially related to this density difference. Obviously, it is important to synthesize bulk nanocrystalline materials with the full densities of conventional materials for property studies and comparisons. It is difficult, however, to prepare

materials that are both dense and fine-grained. The high sintering temperatures generally required to obtain high densities can also lead to grain growth, resulting in a coarse-grained material. Sintering at lower temperatures retains finer grain size, but does not in general yield fully dense material. Recent studies have reported a successful synthesis of dense nanostructured titania, with density > 99% of the theoretical maximum and an average grain size of less than 60 nm[17]. This high-density titania has been prepared by sintering a titanium oxide sol-gel near the anatase-rutile transformation temperature. The increased mobility of the atoms during the phase transformation enhances the sintering rate at lower temperature. This method could be used more generally to produce nanophase materials with near theoretical densities.

In general, the microstructural features of nanophase materials such as grain size, distribution of grain size, morphology, nature of intragrain defects, and nature and morphology of grain boundaries, are important. Although some research has focused on characterizing microstructures of nanophase materials, there are many open questions remaining in regard to the exact atomic scale structure of grain boundaries, and the nature of intragrain defects. In the study of nanocrystalline Cu and Pd[18], it was suggested from the results of extended x-ray absorption fine structure (EXAFS), that the grain boundary component of nanocrystalline materials represents a new solid state structure with a very random atomic arrangement. Merkle *et al.*[19] found that the boundary core density of nanophase oxide NiO is lower than that of liquid or glassy phases and is comparable to the density of highly compressed gas. Such a boundary core region represents a solid-state structure of remarkably low density. Based on

these experiments, Gleiter and Birringer [14,16] have interpreted most of their results in terms of a two-component microstructure, i.e., perfect crystal grains and a grain boundary component. In contrast, with the same synthesis method (gas condensation) for nanophase materials, Siegel's group [20] found from high-resolution electron microscopy observations (combined with image simulations) as well as from Raman spectroscopy and small angle neutron scattering experiments, that grain boundaries of cluster-assembled nanophase materials are similar in structure to those of normal coarse-grained polycrystals. They are commonly observed to be relatively flat and faceted with well-ordered localized structures. It thus seems possible that the grain boundary structures of nanocrystalline phases depend on the synthesis method and could vary from system to system as well. In this thesis, the structural properties of both nanocrystalline and amorphous phases synthesized by MA of Al-Zr system will be discussed in Chapter 3 and Chapter 5.

1.2.1 Synthesis methods

The methods of preparing nanometer-sized crystalline materials can be divided into two categories. One includes two steps: generating nanometer-sized clusters and assembling the clusters by *in situ* consolidation and sintering. The second class of methods does not include the step of pre-generated clusters.

a. Cluster-assembled methods

An example of the two-step method is the synthesis of ultra-fine-grained materials by vapor condensation in an inert gas as described by Gleiter[21]. A typical apparatus consists a gas-condensation chamber and

powder consolidation cell as schematically depicted in Fig. 1.6 [22]. The precursor materials are evaporated from sources A and/or B, then condense into a fine aersol within the inert gas, which is finally transported via convection and thermophoreses to a liquid-nitrogen cooled cold finger. The powders are subsequently scraped from the cold finger, collected via the funnel, and consolidated first in the low-pressure compaction device, and then in the high-pressure compaction device. Many experiments on synthesizing cluster-assembled nanophase materials have been carried out within this type of vacuum chambers. Techniques for generating nanometer-sized clusters may also include sputtering [23], laser ablation [24], flame hydrolysis [25,26], etc. Cluster-assembled nanophase materials can be metals [22,27,28,29], ceramics [30,31], semiconductors [32,33], or composites. Besides the two-step cluster-assembled methods, there are other techniques which can be utilized for making nanophase materials.

b. Other techniques

High-energy ball milling has been used to synthesize nanostructured materials, and many experimental results about preparing nanometer sized metals and alloys have been published with MA or MM methods[34-40]. The grain sizes of powder samples can usually be reduced to 5-15 nm by MM. Mechanical alloying process was found not only refining the grain size but also extending the solute solubility in the solid solution compared with the equilibrium solubility. The advantage of ball milling is that a large amount of nanocrystalline materials can be produced, but one has to consider all the possible contamination which may come from the container, balls and atmosphere. The contamination problem could be

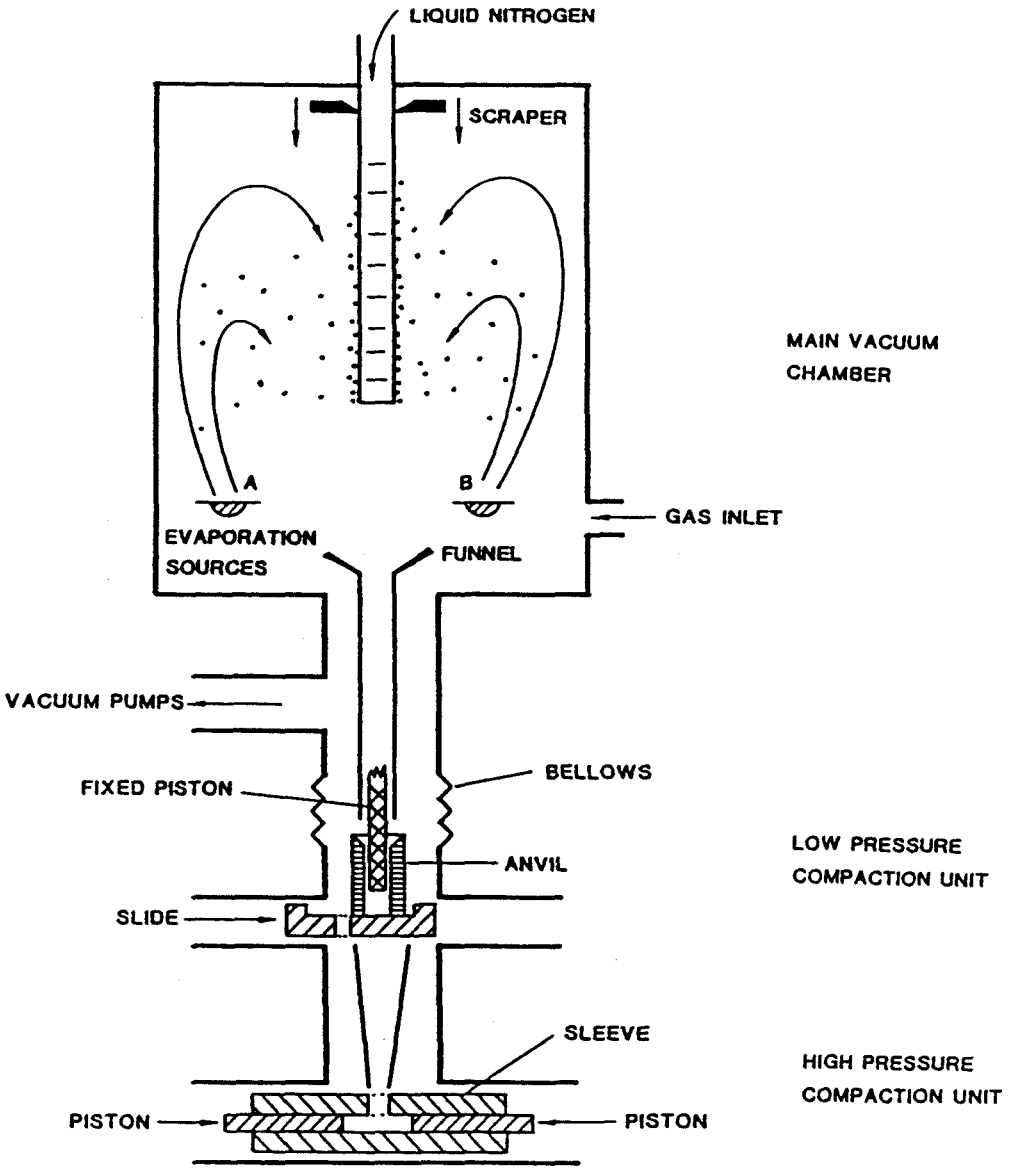

Fig. 1.6 Schematic drawing of a gas-condensation chamber for the synthesis of nanophase materials.

minimized by using the correct medium and ensuring a good sealing of the milling vial.

Chemical vapor deposition (CVD) has been utilized to synthesize nanocrystalline materials, for instance, the nitrides and carbides of titanium and silicon systems [41]. Vapor deposition [42] and Electrodeposition [43] can be used to prepare the nanostructure phases as well. One example is the electrodeposition of Ni-P alloys under suitable conditions leads to nanocrystalline structures [44,45].

Nanometer-sized ceramic materials have been generated by a so called sol-gel technique. The nanostructured materials are obtained by seeding of a ceramic precursor with crystalline sols of the final equilibrium phase to catalyze nucleation [46-49].

Lu *et al.* [50] has prepared several nanometer-sized crystalline materials (for example, 9 nm Ni-P alloys) by crystallization of the rapid quenched amorphous ribbon. The annealing process has to be dynamically controlled to form a polycrystalline material with nanometer-sized grains. The method can be applied only for some special systems in which a reduced growth rate and an accelerated nucleation rate are required. Another obvious drawback for this method is the system has to be pre-prepared as an amorphous phase that will limit the applied system as well.

Some other methods such as electrochemical method [51,52], rapid solidification [53,54,55] and sliding wear of metals [56] have also been demonstrated for pure metals as well as alloys to result in nanocrystalline materials.

1.2.2 Properties and applications

Nanophase materials often have considerably improved mechanical, electrical, optical and magnetic properties in comparison with those of conventional structure materials. For example, nanophase TiO_2 exhibits considerable improvements in the sintering ability and resulting improved mechanical properties relative to normal coarse-grained materials [57]. The sintering temperature has been lowed by 400-600°C. Their formability is another distinct advantage of ultrafine-grained materials due to the increasing of ductility. The ability to produce dense nanometer-sized ceramics that are formable and ductile can have a significant technological impact in a wide variety of applications. Another example for the possible future uses of nanocrystalline materials was discussed by de Wit *et al.* [58] for video recorder heads. In present video recorders, the magnetic material of record head is usually a crystalline ferrite. These materials, however, are not so suitable when substantially finer details on the magnetic tape are required. The nanocrystalline materials combine a high saturation magnetization with a high permeability in the MHz frequency range, allowing video recording at increased information densities.

Because of the large fraction of atoms at grain boundaries, grain boundary diffusion can have an effect on both self diffusion [59] and solute diffusion behavior [60]. In comparing hydrogen diffusion in amorphous alloys to that in nanocrystalline Pd metal, it was found [61] that the average activation energy for hydrogen diffusion in nanocrystalline samples is much less than that in glass phase which suggests a more open structure in the grain boundary than in the glass material. Hence, nanocrystalline materials may be utilized technologically as materials with high

diffusivities. It was also reported that nanocrystalline solids seem to permit the alloying of conventionally immiscible components or in some cases, to enhance the solute solubility in the solid solution significantly [15,62,63]. Enhancements of thermal properties have been observed as well. For instance, the thermal expansion of grain boundaries in copper was measured and compared with copper polycrystals [64]. From the measurements, the thermal expansion coefficient of a grain boundary in copper is about 2.5 to 5 times the expansion coefficient of a conventional copper crystal which suggests large anharmonic atomic vibrations in grain boundaries.

Gleiter summarized [65] that the properties of crystalline and glass phases deviate by about 5% or less, whereas the difference between the nanocrystalline and the crystalline phases varies between 50% and a factor up to 10^{21} for the identical chemical composition materials. However, one must note that some property changes, such as rapid diffusion, appear to be intrinsically coupled with the porous nature of the interfaces in nanophase materials and might be suppressed to conventional values by sintering to full densities[66].

1.3 Amorphous phases

Amorphous alloys or metallic glasses are metal alloys with no long range atomic order, yielding diffuse diffraction patterns and no contrast in transition electron micrographs. In spite of the absence of a long range periodicity, the structure of metallic glass is defined by the local order in a cluster of atoms involving the first, second and perhaps the third neighbors of any given atom. Thus, the amorphous state, in fact, is not a unique state, but exhibits a considerable and continuous variation of its microscopic state.

Such a microscopic state is basically described by the atomic short range order. The most direct characterizations of atomic arrangements in glasses are from x-ray, neutron and electron scattering experiments. Such scattering measurements can be inverted to obtain the radial distribution function (RDF), which is the direct measure of spatial correlation among atoms in amorphous materials. However, the total RDF does not contain enough information to completely characterize the atomic scale structure, and information about the local atomic correlations is lost. To study the short range order of amorphous phase, the derivations of more accurate partial correlation functions for amorphous alloys from various scattering techniques are required [67]. Amorphous phases are metastable with respect to the stable crystalline phases. The properties of an amorphous phase are intimately related to its atomic structure. The world-wide interest in amorphous metals is directly attributable to a world-wide interest in the engineering performance potential of metallic glasses.

1.3.1 Synthesis methods

There are many different techniques that can be used to prepare materials in an amorphous state. Of these, some are commonly used and some actually work under the same or similar principle. With various techniques, amorphous phases can be formed starting from all three phases of matter (vapor, liquid and solid).

a. Amorphous phase formation from gas or liquid phase

The conventional methods to make metallic glasses all involve the rapid solidification of the alloying constituents from the gas or liquid phases by a variety of techniques. The fundamental idea is that solidification

occurs so rapidly that the atoms are frozen in their gas or liquid structure. There is no time for atoms to rearrange from random gas or liquid phase to a periodic ordered equilibrium crystalline phase. A major breakthrough for the synthesis of metallic glass occurred in 1959 when Duwez *et al.* [68] found that amorphous alloys could be produced by rapid quenching from the liquid state at ambient temperature. In this case, the nucleation and growth processes of the thermodynamically stable crystalline phases are suppressed at cooling rates of approximately 10^6 K/sec. This is possible, in particular, for alloys having compositions near the deep eutectics. Fig. 1.7 is a schematic illustration of the different common techniques used to form glassy metallic ribbons from the melts. Some other methods such as thermal evaporation [69,70], sputtering, chemical vapor deposition (CVD), electrolytic deposition, pulsed lasers, etc., are also alternatively utilized to form amorphous phase from gas or liquid phase.

b. Amorphous phase formation in the solid state

Systematically studies on metallic glass formation from solid phases was first started by Yeh *et al.* and involved reaction of hydrogen gas with a metastable crystalline Zr_3Rh alloy [71]. Based on a set of experimental observation, they recognized that certain thermodynamic and kinetic conditions are required for the hydrogen-induced amorphization occurs. This method has since been studied widely for several different systems, especially for C15 Laves phase [72,73,74] and $L1_2$ Cu_3Au [75,76] structures. Soon after the Zr_3Rh hydriding experiment, Schwarz and Johnson [77] reported another solid-state reaction method for inducing a crystal-to-amorphous phase transition. They showed that crystalline multilayed diffusion couples of Au and La can be reacted to form amorphous Au-La

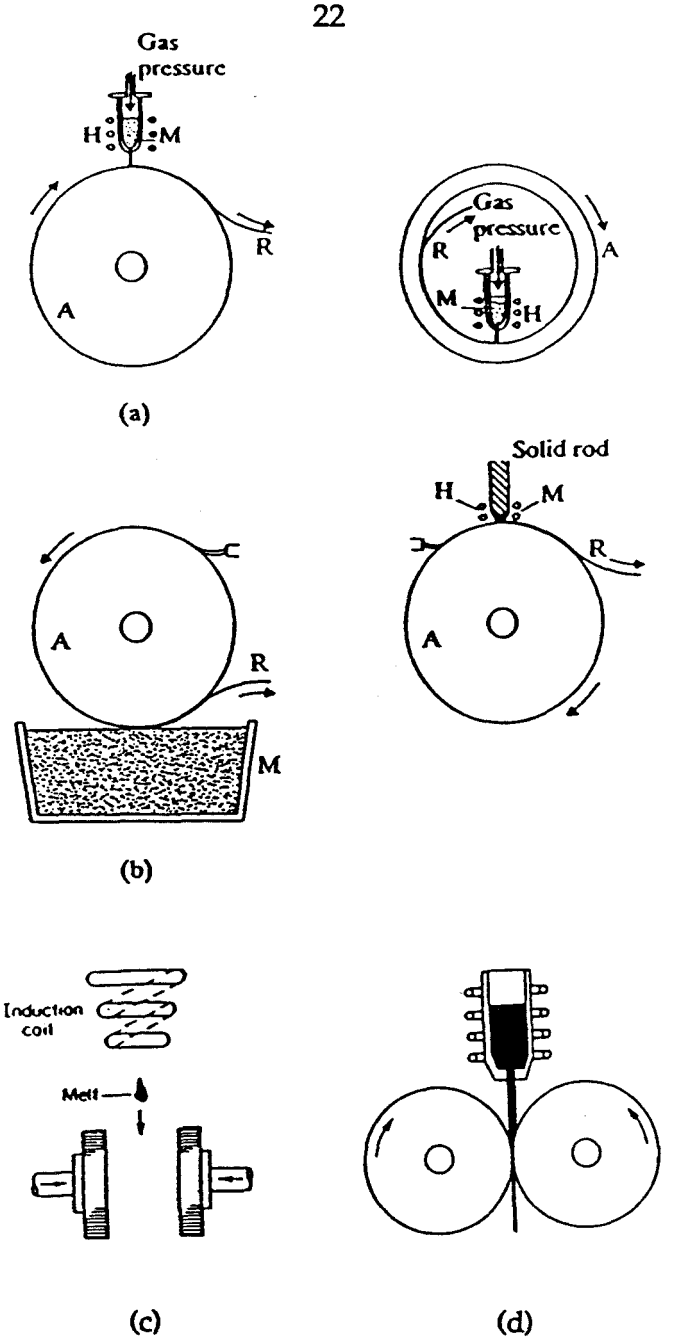

Fig. 1.7 Schematic illustration of the typical techniques to form metallic glass by rapid quenching: (a) melting spinning, both external and internal; (b) melt extraction, both crucible and pendant drop; (c) drop-smasher, using levitation melting by induction; (d) twin-roller quenching device.

alloy by isothermal annealing at a low enough temperature. Similar to the mechanism of hydriding process, the thermodynamic driving force is provided by the large negative heat of formation of the amorphous phase. A fast diffusing component (similar to hydrogen) is essential to satisfy the kinetic constraints for producing and retaining the metastable glass phase. Since the Au-La study, amorphous phase formation from metal diffusion couples has been observed in a large number of other binary metallic systems such as Ni-Ti [78], Ni-Zr [79], Au-Y [80].

Two other related techniques for synthesizing metallic glass phase are irradiation and ball milling. A description of the ball milling method has been given at the beginning of this chapter. Here, only some simple comparisons between mechanical milling and irradiation method will be given since these two techniques are very similar in principle. In contrast to the solid-state diffusion couple and hydriding cases, irradiation and ball milling are processes in which systems are driven to amorphous phases by "external" energy and large amounts of defects created by bombarding with energetic particles or heavy mechanical deformation. Moreover, in both cases, the amorphization does not occur under isothermal conditions. The fact that there is no direct and easy method of *in situ* monitoring of the collision processes makes it difficult to understand the exact mechanism by which vitrification takes place at the microstructural level. Both mechanical milling and irradiation are powerful techniques for amorphizing an intermetallic compound by the introduction of chemical disorder and defects in the ordered compound phase. It was found that the glass forming ranges for mechanical milling/alloying and irradiation are not restricted to eutectic compositions as is the case for rapidly quenched

amorphous alloys. By the structural comparisons of amorphous CuZr and NiTi alloys (CsCl type) prepared by proton irradiation and mechanical alloying, Lee *et al.* [81] and Wagner *et al.* [82] concluded the short range atomic distribution in these amorphous alloys is the same. When Di *et al.* [83] studied the mechanical milling of the well-known superconductor Nb_3Sn system, they found that the time-dependence of the change in the superconducting transition temperature is similar to that observed during irradiation by heavy particles. The change in the lattice parameter is also of the same magnitude as that found in an irradiation experiment. In conventional techniques such as rapid quenching, very high cooling rates of 10^4-10^{12} K/s are required to avoid nucleation and growth of crystalline phases. These cooling rates are a severe restriction in the production of bulk amorphous materials and therefore in the technical application of metallic glasses. The advantage for ball milling is that a large amount of sample powder can be synthesized making it possible to consolidate the powder to bulk amorphous materials. The main drawback is the contamination from the milling medium and atmosphere.

Other different methods such as pressure-induced amorphization [84], ion implantation [85] belong to this category as well (for good review papers, see [6,10,86]).

More recently, a set of ternary and quarternary systems were prepared in amorphous form by water quenching. For example, a $La_{55}Al_{25}Ni_{20}$ alloy was found to be amorphized by quenching the melt in a quartz capillary into water resulting in an amorphous alloy having a cylindrical form with the diameter in the range of several mm [87]. This discovery opens a new field for researchers to synthesize bulk metallic glasses and to understand the

intrinsic reasons why the high glass-forming ability exists in these systems. In practice, it makes the potential applications of bulk amorphous alloy materials more attractive.

1.3.2 Properties and applications

Generally, metallic glass materials possess some desirable or unique electrical, magnetic, mechanical, and corrosion properties that have many applications in science and technology. In contrast to the above discussed nanophase materials in which the grain boundary properties are enhanced, amorphous materials are often structurally homogeneous and isotropic on a macroscopic length scale and have no grain boundaries or crystalline defects such as dislocations or stacking faults. As a result, their physical and chemical properties are also isotropic and homogeneous. One example of making use of the absence of grain boundary in amorphous phase is in magneto-optic storage materials [88]. These materials are generally amorphous alloys of the rare earth and the transition metals, like Fe or Co. Amorphous materials have a distinct advantage for this purpose because they do not suffer from "grain noise," spurious variations in the plane of polarization of reflected light caused by randomness in the orientation of grains in a polycrystalline film. The absence of structural defects directly leads to a dramatic effect on the mechanical behavior, resulting in many uses of amorphous materials in mechanical engineering applications. For example, because amorphous materials are often structurally homogeneous and do not have crystal-like defects, they can have mechanical strengths approaching ideal values. The ductility of certain intermetallic amorphous alloys makes them extremely useful for brazing alloys. Their hardness, high permeability and zero magnetostriction make them useful for recording

heads. Their high permeability and toughness make them useful for magnetic-shielding applications. The high stress-sensitivity of some amorphous alloys makes them useful as stress transducers. Their electrical properties are different from the same alloy in the crystalline state due to a random atomic arrangement. These properties usually include a high value of electric resistivity and a very small temperature dependence which might be of interest in electrical circuitry or measuring instruments requiring resistance components insensitive to temperature. The improved properties in comparison to conventional stable materials have motivated considerable research in this field. The amorphous phase can be regarded as chemically homogeneous with respect to the surface-related characteristics such as corrosion and catalysis[89]. The excellent corrosion resistance of amorphous materials makes them very useful for coatings.

As we can see, the many methods discussed here have been utilized for preparing both nanocrystalline and amorphous materials. In fact, due to the common features of metastable phases, these techniques are not limited to nanocrystalline or amorphous materials. They are useful for synthesizing almost all the other metastable or configurationally frozen phases such as metastable compounds or quasi-crystalline phases as long as suitable synthesis conditions can be found.

References

[1] J. S. Benjamin, *Metall. Trans.* **1**, 2943 (1970).

[2] D. R. Maurice and T. H. Courtney, *Metall. Trans. A* **21A**, 289 (1990).

[3] P. S. Gilman and J. S. Benjamin, *Annu. Rev. Mater. Soi.* **13**, 279 (1983).

[4] A. Y. Yermakov., Y. Y. Yurchikov and V. A. Barinov, *Phys. Met. Metall.* **52**, 50 (1981).

[5] C. C. Koch et al. *Appl. Phys. Lett.* **43**, 1017 (1983)

[6] W. L. Johnson, *Prog. Mater. Sci.* **30**, 81 (1986)

[7] E. Hellstern, H. J. Fecht, Z. Fu and W. L. Johnson, *J. Appl. Phys.* **65**, 305 (1989); H. J. Fecht, E. Hellstern, Z. Fu and W. L. Johnson, *Adv. Powd. Met.* **2**, 111 (1989); H. J. Fecht, G. Han, Z. Fu and W. L. Johnson, *J. Appl. Phys.* **67**, (4) 1744 (1990).

[8] D. R. Maurice and T. H. Countney, *Metall. Trans. A* **21A**, 289 (1990).

[9] D. Turnbull, *Metall. Tran. A* **12A**, 695 (1981)

[10] W. L. Johnson, *Mater. Sci. and Emg.* **97**, 1 (1988).

[11] H. Gleiter and P. Marquardt, *Z. Metall.* **75**, 263 (1984); R. Birringer, H. Gleiter *et al., Phys. Lett.* **A 102**, 365 (1984).

[12] H. Gleiter, *J. Appl. Cryst.* **24** 79-90 (1991).

[13] R. W. Siegel, *Annu. Rev. Mater. Sci.* **21**, 559 (1991).

[14] H. Gleiter, *Progress in Mater. Sci.* **33**, 223 (1989).

[15] R. Birringer and H. Gleiter, Adv. in Mater. Sci., Encyclopedia of Mater. Sci. and Eng., Suppl. 1, ed. by R. W. Cahn, (Pergamon Press Oxford), p. 339 (1988).

[16] R. Birringer, *Mater. Sci. Eng. A.* **117**, 33 (1989).

[17] K.-N. P. Kumar, K. Keizer *et al., Nature* **358,** 48 (1992).

[18] T. Haubold, R. Birringer *et al, Phys. Lett.* **A 135,** 461, (1989).

[19] K. L. Merkle, J. F. Reddy *et al., Phys. Rev. Lett.* **59,** 2887 (1987).

[20] R. W. Siegel, *Ultramicroscopy* **40,** 376 (1992).

[21] H. Gleiter, In Deformation of Polycrystals: Mechanisms and Microstructures, ed. N. Hansen et al., p. 15, Roskilde: Riso Natl. Lab.

[22] R. Birringer, *Ph.D. Thesis,* University of Saarland, Germany (1985).

[23] P. Fayet and L. Woste, *Z. Phys.* **D3,** 177 (1986).

[24] M. L. Mandich *et al., J. Chem. Phys.* **86,** 4245 (1987).

[25] DEGUSSA, Patent Nr. DE 762 723 (1942).

[26] DEGUSSA, Frankfurt, *Tech. Bull. Pigments* **56,** 12 (1982).

[27] M. Carey Lea, *Am. J. Sci.* **37,** 479 (1989).

[28] E. Hort, *Diploma Thesis,* University of Saarland, Germany (1985).

[29] U. Herr, *Diploma Thesis,* University of Saarland, Germany (1985).

[30] R.W. Siegel and H. Hahn, Current Trends in Physics of Materials, ed. M. Yussouff, (World Scientific Publ. Co., Singapore, p. 403 (1987).

[31] J. Karch, R. Birringer and H. Gleiter, *Nature* **330,** 556 (1987).

[32] Y. Wang *et al., J. Chem. phys.* **87,** 7315 (1987).

[33] N. F. Borrelli *et al., J. Appl. Phys.* **61,** 5399 (1987).

[34] E. Hellstern, *et al., J. Appl. Phys.* **65,** 305 (1989).

[35] H. J. Fecht, *et al., J. Adv. Powder Metall.* **1,** 11 (1989).

[36] J. S. C. Jang ,*et al., Scr. Metall. Mater.* **24,** 1599 (1990).

[37] J. Eckert, *et al., J. Mater. Res.* **7** (7) Page? (1992).

[38] K. L. Breitbach and L. S. Chumbley, *Scripta Metall. Mater.* **25,** 2553 (1991).

[39] M. Oehring and R. Bormann, *Mater. Sci. and Engn.* **A134,** 1330 (1991).

[40] C. Suryanarayana *et al., J. Mater. Res.* **5** (9), 1880 (1990).

[41] B. M. Gallois, R. Mathur *et al., Mater. Soc. Symp. Proc.* **132,** 49 (1989).

[42] R. L. Bickerdife, D. Clark *et al., Int. J. Rapid Solidification* vol. **1,** p. 305 (1984-85).

[43] D. S. Lashmore and M. P. Dariel, Encyclopedia of Mater. Sci. and Eng., ed. by R. W. Cahn, (Pergamon Press, Oxford, United Kingdom) suppl. vol. **1,** p. 136 (1988).

[44] H. Bestgen, Microstructure of Amorphous and Microcrystalline Electrodeposited Co-P, Ni-P and Fe-P, *Proc. 5th. Conf. Rap. Quenched Met.* p. 443 (1985).

[45] R. Sonnenberger, E. Pfanner and G. Dietz, *Z. Phys. B.* **63,** 203 (1986).

[46] R. A. Roy and R. Roy, Abstracts, *Mater. Res. Soc. Annu. Meeting,* (Boston, MA,) p. 377 (1982).

[47] D. W. Hoffman *et al., Ceram. Bull.* **62,** 375 (1983).

[48] D. W. Hoffman *et al., J. Mater. Sci. Lett.* **3,** 439 (1985).

[49] Y. Suwa, R. Roy and S. Komarneni, *Mater. Sci. Eng.* **83,** 151 (1986).

[50] K. Lu, W. D. Wei *et al., Scr. Metall. Mater.* **24,** 2319 (1990); K. Lu, J. T. Wang, and W. D. Wei, *J. Appl. Phys.* **69** (1), 1 (1991).

[51] G. McMahon and U. Erb, *Microstructural Science* **17,** 447 (1989).

[52] A. M. El-Sherik *et al,* Structure and Properties of Interfaces in Materials, edited by W. A. T. Clark *et al,* (Mater. Res. Soc. Proc. **238,** Pittsburg, PA, 1992).

[53] S. J. Savage and F. H. Froes, *J. Metals* **36,** 20 (1984).

[54] T. R. Anantharaman, Metallic glasses: production, properties and applications, Trans. Tech., p. 1 (1984).

[55] J. Bigot, Preparation of metallic Glasses and its Influence on the Properties, Summer School on Amorphous Metals, World Scientific, Publ. Co., Singapore, p. 18 (1986).

[56] S. K. Ganapathi *et al.*, Clusters and Cluster-Assembled Materials, edited by R. S. Averbach et al, (Mater. Res. Soc. Proc. **206**, Pittsburg, PA, 1991), p. 593.

[57] J. E. Epperson, R. W. Siegel *et al., Mater. Res. Soc. Symp. Proc.* **132**, 15 (1989); J. E. Epperson, R. W. Siegel *et al., Mater. Res. Soc. Symp. Proc.* **166**, 87 (1990).

[58] H. J. de Wit, *et al., Adv. Mater.* **3** (7/8), 356 (1991).

[59] J. Horvath, R. Birringer and H. Gleiter, *Solid State Comm.* **62**, 319 (1987).

[60] S. Schumacher *et al., Acta Metall.* **37** (9), 2485 (1989).

[61] R. Kirchheim, *et al., Mater. Sci. and Engn.* **99**, 457, (1988).

[62] R. Kirchheim, *et al., Mater. Sci. and Engn.* **99**, 462, (1988).

[63] H. J. Fecht, G. Han, Z. Fu and W. L. Johnson, *J. Appl. Phys.* **67**, (4) 1744 (1990).

[64] H. J. Klam, H. Hahn and H. Gleiter, *Acta Metall.* **35** (8), 2101, (1987).

[65] H. Gleiter, *Phase Transitions* **24-26**, 15 (1990).

[66] R. S. Averback *et al., Mater. Res. Soc.. Symp. Proc.* **153**, 3 (1989).

[67] C. N. J. Wagner, *J. Non-Cryst. Solids* **31**, 1 (1978).

[68] P. Duwez, R. H. Willens, and W. Klement Jr., *J. Appl. Phys.* **31**, 1136 (1960).

[69] S. R. Elliott, Physics of amorphous Materials, 2nd ed. (Longman Scientific & Technical, Copublished in the United States with John Wiley & Sons, Inc., New York) p. 8 (1990)

[70] H. J. Leamy *et al.*, in Current Topics in Materials Science, vol.6, E. Kaldis (ed.) (North-Holland) p. 309 (1980)

[71] X. L. Yeh, K. Samwer and W. L. Johnson, *Appl. Phys. Lett.* **42**, 242 (1983).

[72] K. Aoki, T. Yamamoto *et al., Acta Metall.* **35**, 2465 (1987).

[73] H. J. Fecht, Z. Fu and W. L. Johnson, *Phys. Rev. Lett.* **64**, 1753 (1990).

[74] K. Aoki, X.-G. Li, T. Aihara *et al., Mater. Sci. Eng.* **A133,** 316 (1991).

[75] W. J. Meng, P. R. Okamoto et al., Appl. Phys. Lett. **53** (19), 1820 (1988).

[76] J.-Y. Lee, W.-C. Choi *et al., Acta Metall. Mater.* **39** (7), 1693 (1991).

[77] R. B. Schwarz and W. L. Johnson, *Phys. Rev. Lett.* **51,** 415 (1983).

[78] B. M. Clemens, *Phys. Rev. B.* **33,** 7615 (1986).

[79] B. M. Clements, R. B. Schwarz and W. L. Johnson, *J. Non-Cryst. Solid* **61,** 817 (1984).

[80] R. B. Schwarz, K. L. Wong and W. L. Johnson, *J. Non-Cryst. Solid,* **61/62,** 129 (1984).

[81] D. Lee, J. Cheng et al., *J. Appl. Phys.* **64** (9), 4772 (1988).

[82] C. N. J. Wagner, D. Lee et al., *J. Non-Crystall. Solid* **106,** 81 (1988).

[83] L. M. Di, P. I. Loeff and H. Bakker, *J. Less-Comm. Metals* **168,** 183 (1991).

[84] O. Mishima, L. D. Calvert and E. Whalley, *Nature* **310,** 343 (1984).

[85] G. Linker, *Solid State Commun.* **57,** 773 (1986).

[86] K. Samwer, *Phys. Report* **161** (1), 1 (1988).

[87] Akihisa Inoue *et al., Materials Trans.,* JIM **30** (9) 722 (1989).

[88] Richard J. Gambino, *MRS Bulletin* **15** (4) 20 (1990)

[89] K. Hashimoto, Amorphous Metallic Alloys, ed. by F. E. Luborsky, (Butterworths & Co. Ltd., London) p. 471, (1983).

Chapter. 2

Experimental Methods

In this chapter, I will describe the experimental instruments and techniques that have been utilized for synthesizing metastable materials and characterizing samples during this thesis research. Some analytical methods for data treatment will also be discussed.

2.1 Mechanical alloying/milling

The metastable phases or configurational frozen phases were synthesized by the so called mechanical alloying/milling technique. A description of the ball milling technique was given in Chapter 1. The general physics of the collision events and temperature effects on the ball milling process were studied by Maurice *et al.* [1]. From geometrical considerations and characteristics of the specific mill and the material being processed, impact times, powder strain rates and strains, powder temperature increase, and powder cooling times have been approximated by a simple model which is based on Hertzian contacts between the grinding media. For a detailed discussion and results, please see reference [1]. The kinetics of the solid state displacement reaction during mechanical alloying has been investigated by Schaffer *et al.* [2].

Two kinds of milling equipment have been used for preparing samples in the thesis experiments. One is the Spex 8000 mixer/mill. This is a vibrational mill where the milling is done in a mounted vial. There is only one vibrational frequency available for the Spex mill so that only one milling intensity can be chosen. Fig. 2.1 shows the clamp, pillow block and

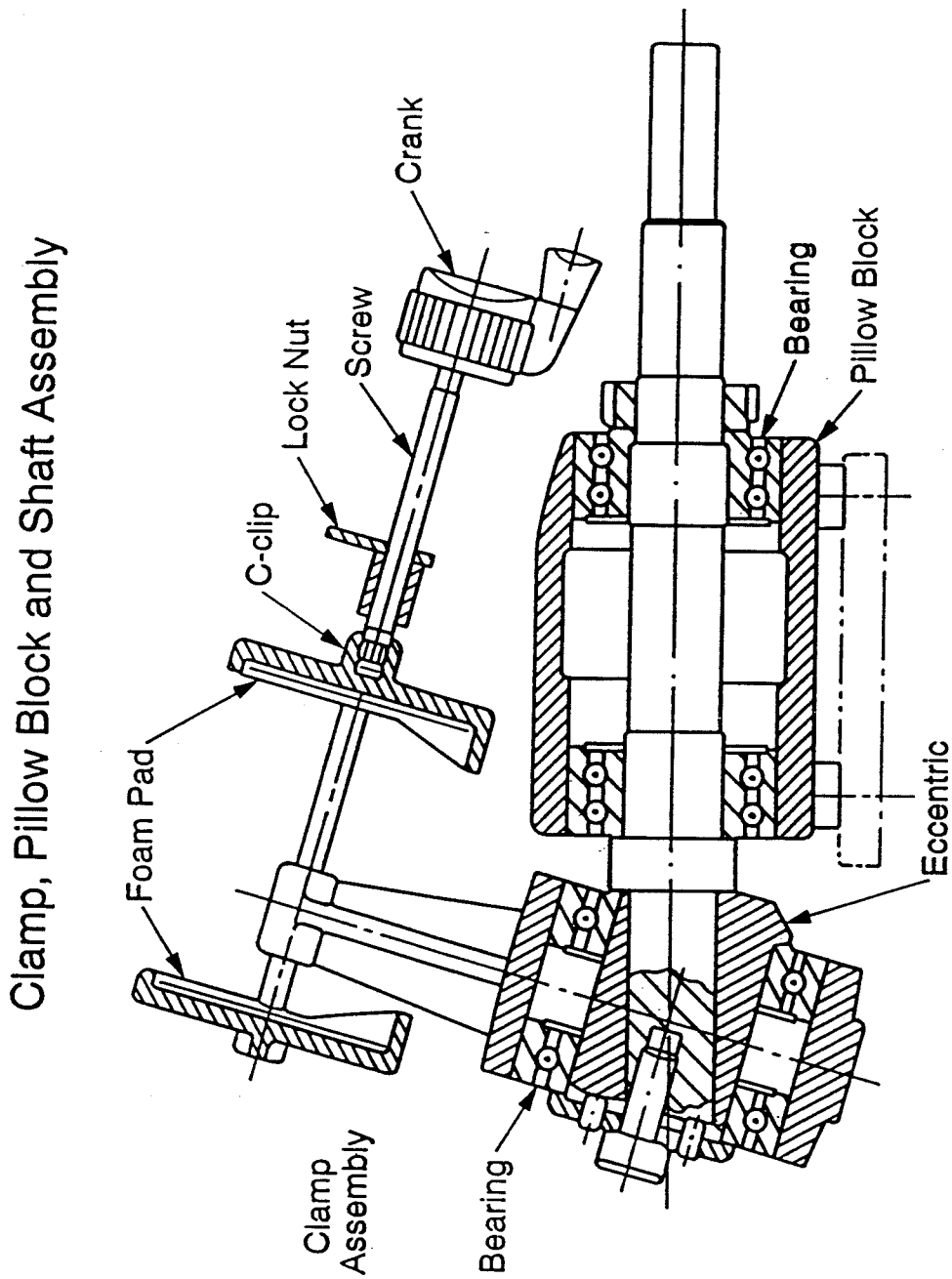

Fig. 2.1 Spex machine's clamp, pillow block and shaft assembly.

shaft assembly of the equipment. The equipment is easy to operate. To place a sample vial in the clamp jars (between the foam pads in Fig. 2.1), tighten the crank firmly and then turn the small locking nut on the threaded rod. Close the door and latch. Using a timer, the milling "on" and "off" sequences can be controlled automatically for each experiment. The mechanical alloying of a mixture of two elemental powders of Zr and Al was carried out in our laboratory SPEX 8000 mixer using a hardened steel vial and balls. To minimize oxidation the loaded vials were sealed under a dry argon atmosphere in a glove bag and the vial temperature during mechanical milling was held near ambient by forced air cooling. The weight of the mixed powder charge for each composition was about 8 g and the ratio of ball weight to powder weight was about 4:1.

A second ball milling machine used in this work is the Super-MISUNI Model NEV-MA8 (Nisshin Giken Co., ltd.). This specialized equipment is particularly designed for mechanical milling under controlled environmental conditions. The Super-MISUNI has a water cooling system for maintaining at room temperature. A vibration speed control can be used for changing the vibration frequency (or milling intensity). The milling can be carried out in vacuum or in a controlled gas atmosphere as required. A vacuum pump and a gas supply valve are built into the ball mill. Heating and cooling units are designed for operating the mill at different temperatures. The equipment consists of vessels, vibration plate, inclined axle, drive motor, power supply, vacuum pump, vacuum and cooling water lines and operation panel. There are two fully equipped vessels on the vibration plate, each with its own inner vessel. The inner vessels have a needle valve for pumping to vacuum or introducing gas.

Fig. 2.2 is a schematic drawing of the normal room temperature milling vessel in the original design. In our experiments, an extra thin steel plate with a small hole in the center was inserted between the inner vessel and the lid which included a needle valve for preventing chemical contamination from the specimen to the lid. Different pieces of thin steel plate can be used while milling different materials. The obvious improvements for the modification are: 1) chemical contamination can not be affected from one material to another via the lid; 2) the needle valve can be protected by filter paper which stays on the top of the small hole of plate for blocking sample powders during pumping and milling. The left hand side vessel can be replaced by either a heating unit or cooling unit depending on the experimental requirement. These units consist of inner vessels for holding sample powders and balls together with outer vessels (fixed by the vibration plate) which can be used as a heating or cooling jackets. To operate under higher temperature conditions, detach the water cooling for standard vessel on the left hand side, and attach the outer vessel accompanied by heater. Fig. 2.3 shows the heater unit for heating vessels. The original design for the heating vessel was sealed by a viton O-ring. Our experimental practice revealed that severe air contamination was due to the failure of the seal at 300°C. Therefore, we have modified the inner vial to seal samples in a glove bag under Ar atmosphere with a Cu gasket seal as shown in Fig. 2.4. The chemical analysis indicated a much lower contamination after the improvement. To measure temperature the K-thermocouple should be placed between the inner vessel and the heater.

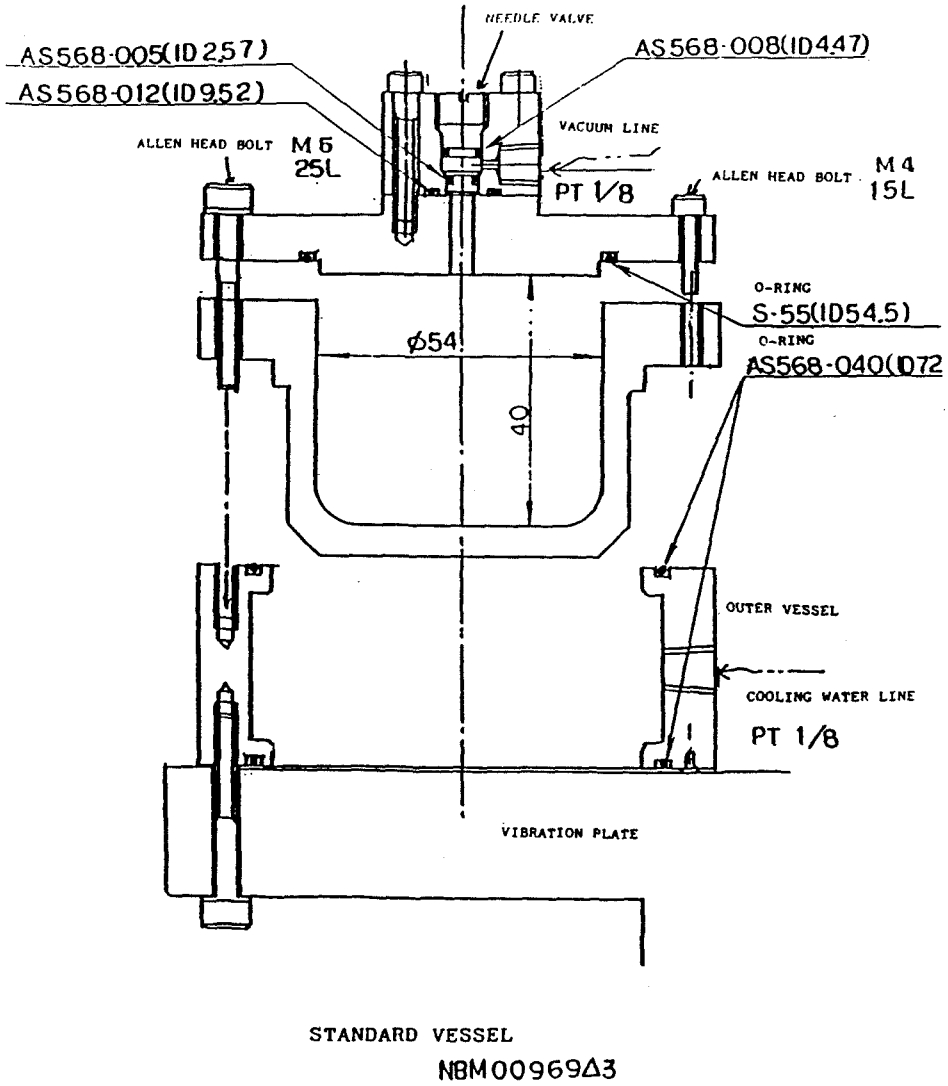

Fig. 2.2 A schematic drawing of the normal temperature milling vessel as the original design for Super-MISUNI machine.

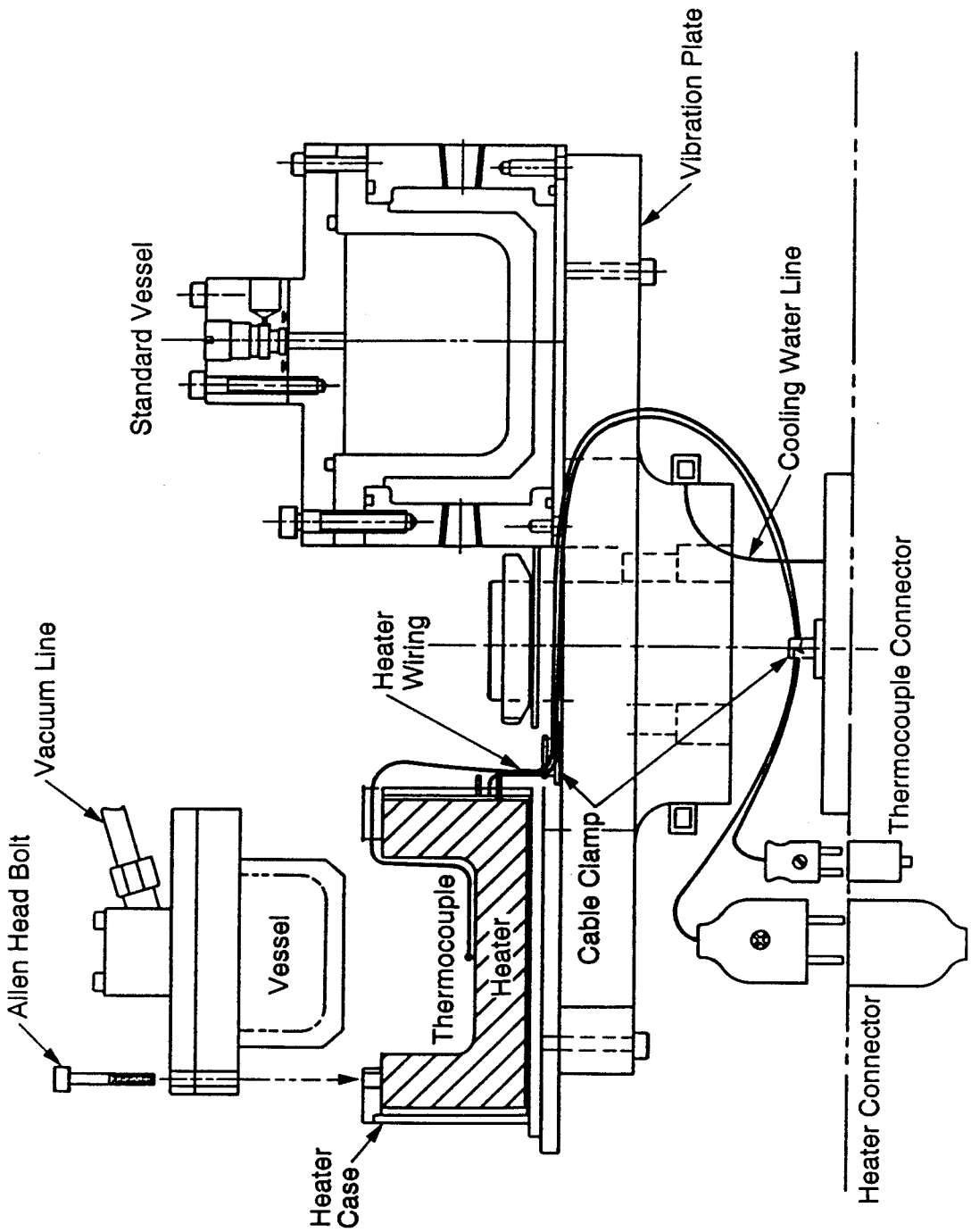

Fig. 2.3 The heater unit for heating vessel.

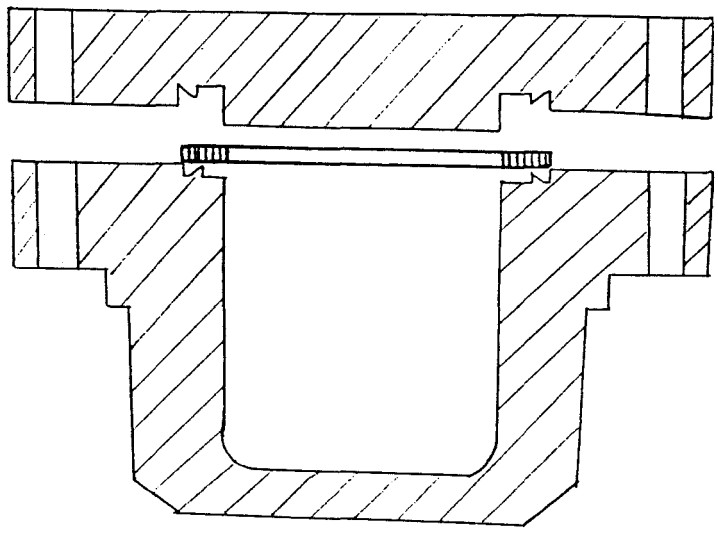

Fig. 2.4 The modified inner vial with Cu gasket seal for ball milling at the ambient temperature higher than 200°C.

After connecting the cable between the main body and the temperature regulator, switch the power on and heat the vessel. A liquid crystal display of the regulator is also used. After setting the heating parameter correctly, an automatic mode can be chosen to keep the vessel at the required temperature. The heating temperature can be well controlled from room temperature to 300°C. To keep the vessel at low temperature during milling, a continuous supply of liquid N_2 is required. It was reported[3] that the temperature can be held in the range of $-180^{o}C < T < -120^{o}C$ with a refill of liquid N_2 every 15 minutes. There are more features for the Super-MISUNI NEV-MA8 milling machine, and all operation switches are mounted on the operation panel. Fig. 2.5 shows the operation panel and Fig. 2.6 shows the water and pumping gas line connections. We have used this equipment for synthesizing metastable materials at both room temperature and "*high*" temperature. It is important to test the seals for each experiment to ensure that the sample environment is controlled. This is done by pumping and filling with inert gas repeatedly. It is found to be preferable to keep the pressure inside the vial greater than atmosphere during the experiments. The disadvantage for the Super-MISUNI NEV-MA8 milling machine is that the milling intensity is lower than in the Spex mill. This leads to about three times longer milling times and perhaps more Fe contamination comparing it with the Spex mill.

2.2 Differential scanning calorimeter

Differential scanning calorimeter (DSC) is an instrument for characterizing the thermal properties of the sample. In general, it can be used for measuring physical properties such as specific heat, C_p and stored enthalpy, ΔH, as well as in studying phase transitions, and chemical

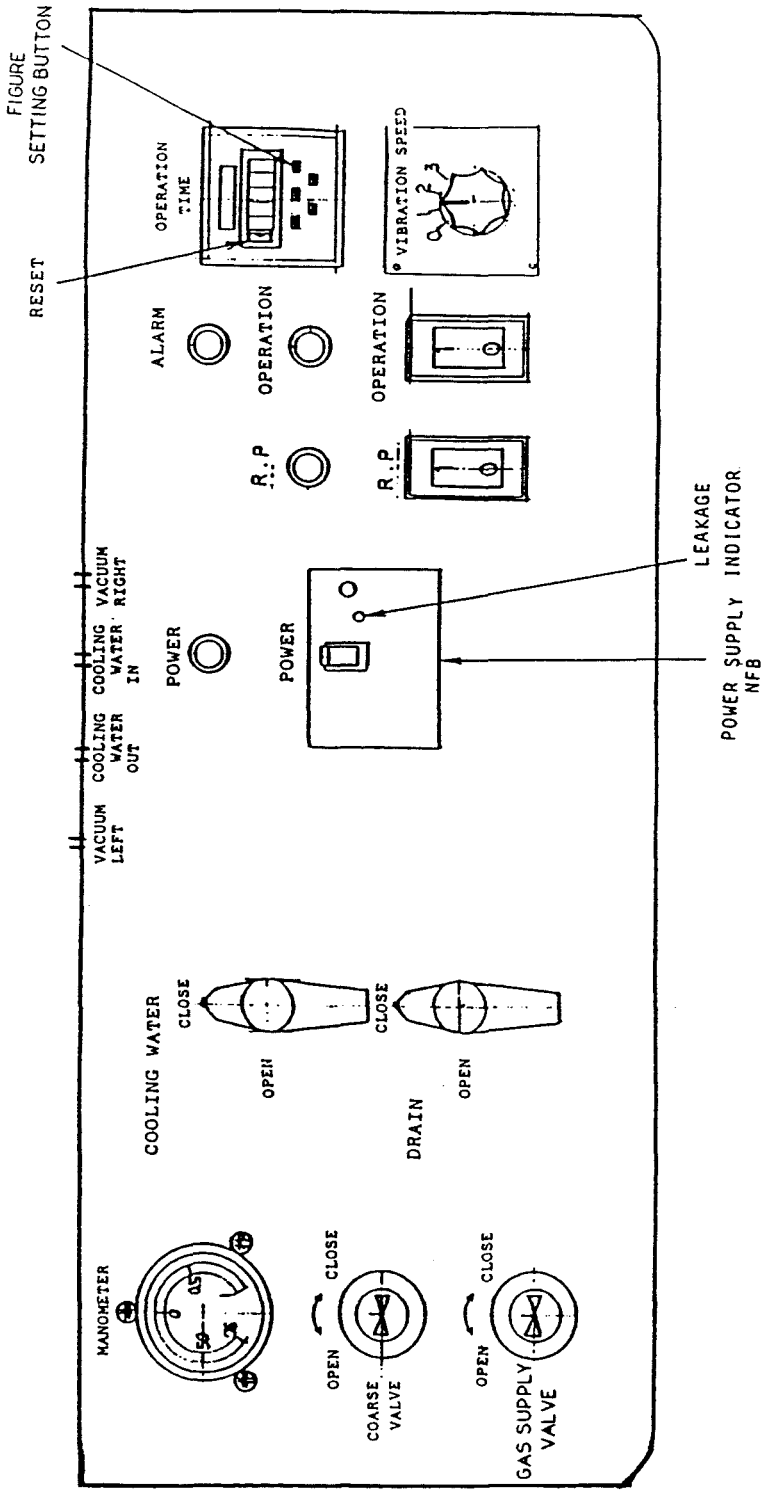

Fig. 2.5 The operation panel for Super-MISUNI machine.

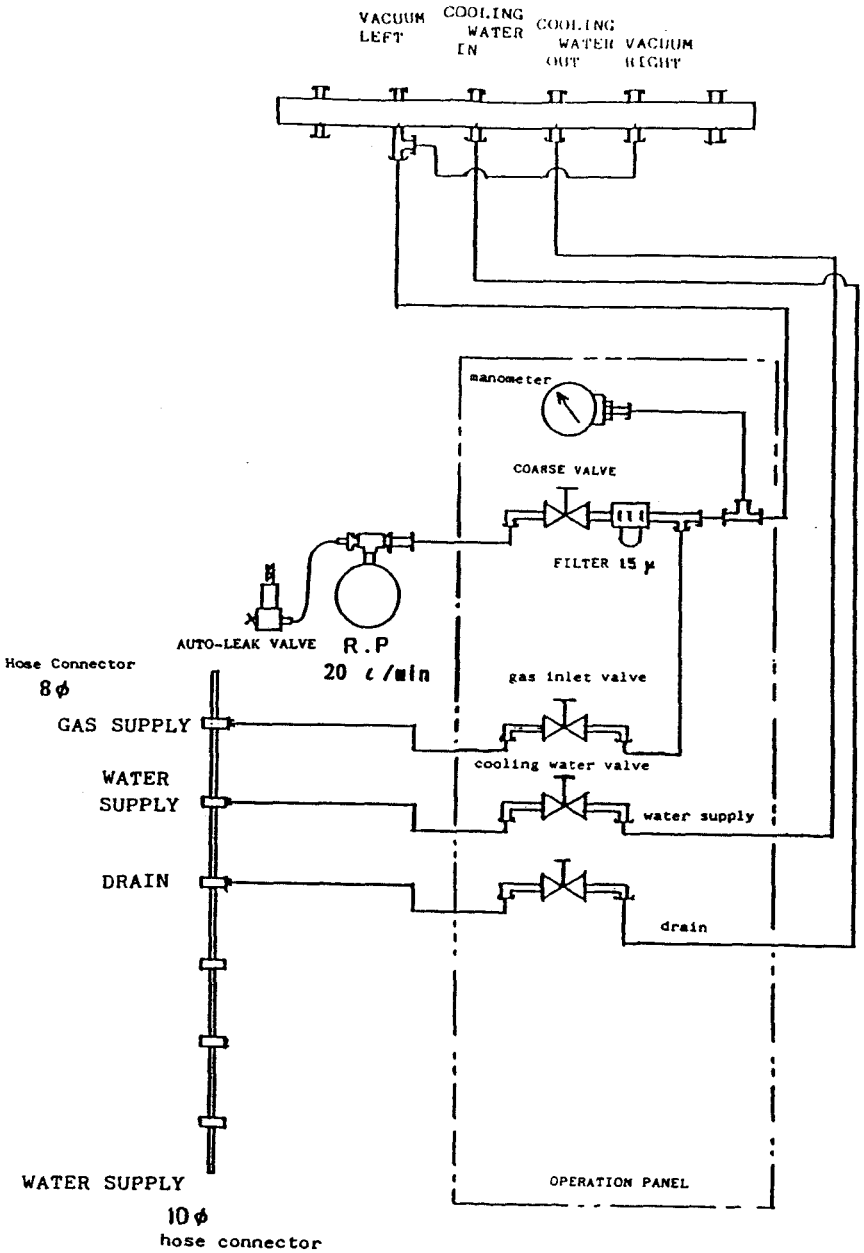

Fig. 2.6 The water, pumping and filling gas line connections.

reactions. The working principle of DSC differs from that of a differential thermal analyzer (DTA). The DTA uses a single furnace and measures the temperature difference developed between the sample and reference material during a thermal event. The DSC, however, using two furnaces, measures the enthalpies of phase transitions or chemical reactions by measuring the differential heat flow required to keep a sample cell and a reference cell at the same temperature. Fig. 2.7 shows the schematic representations for various thermal analysis systems [4]. In Fig. 2.7(c), a sample and reference cells are placed in two separate furnaces each equipped with its own temperature detection sensor and heater. It is convenient to think of the system as divided into two control loops. One is for average temperature control, so the temperature of sample and reference may be increased at a predetermined rate. Another loop ensures that if a temperature difference develops between sample and reference, because of the exothermic or endothermic reaction in the sample, the power input is adjusted to remove this deference. Obviously, a DTA is a thermometric device that measures temperature, while a DSC is a calorimetric device that measures heat flow or energy flow. The difference between DTA and thermal null DSC instrumentation is not only in the number of furnaces used but also in their size. The furnace cells used in DSC are much smaller than that used in DTA. The small furnace size provides for rapid heating and cooling a better control of sample temperature. Hence, DSC provides more accurate data for both temperature and enthalpy than DTA, although calorimetric data can also be derived from DTA measurements. Fig. 2.8 is an idealized thermogram which presents some information given by the DSC experiments.

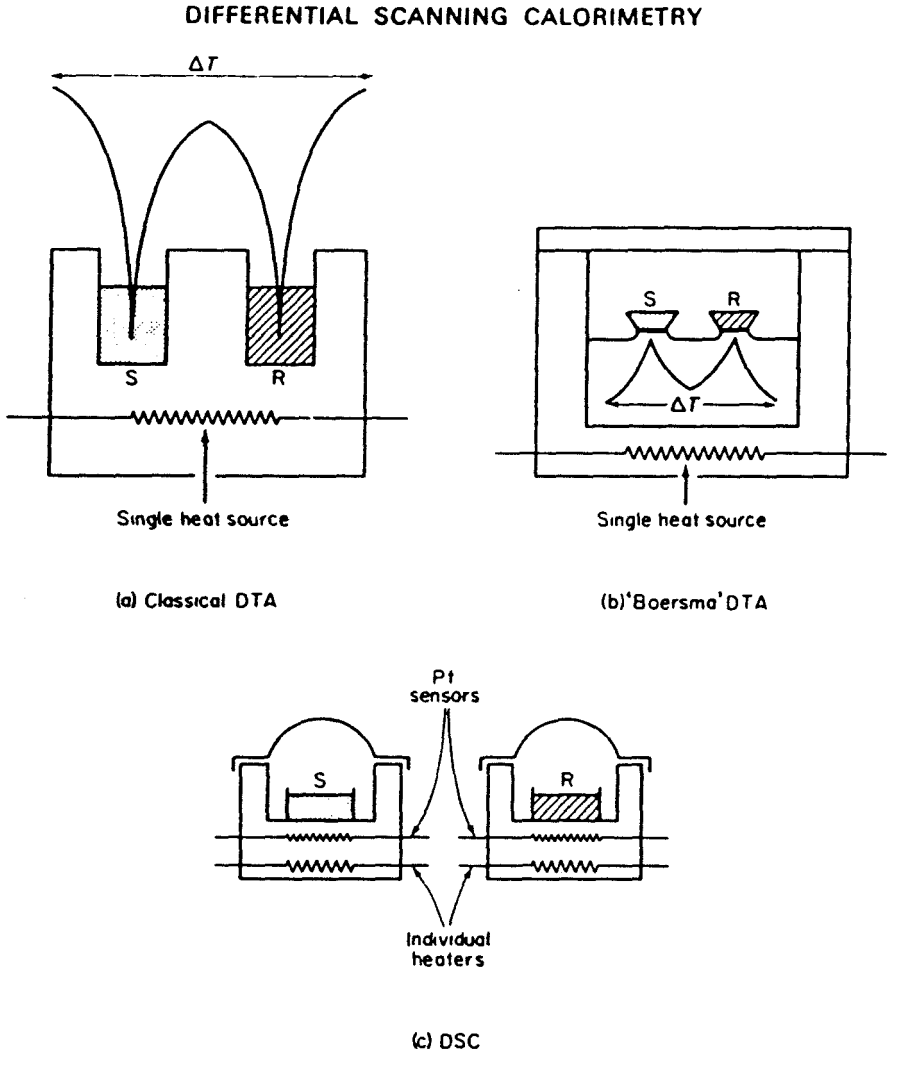

Fig. 2.7 Schematic representation for various thermal analysis systems.

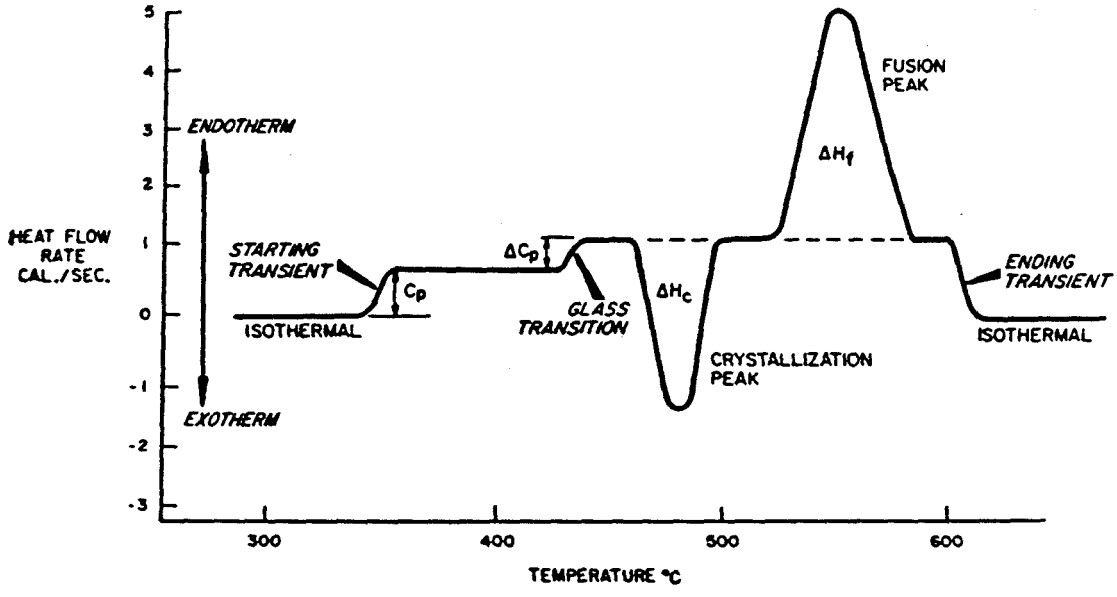

Fig. 2.8 An idealized thermogram for illustrating the information may be given by DSC.

The DSC equipment we used is a Perkin-Elmer DSC-4 interfaced to an IBM-PC computer for data collection and analysis. With ice water as a reservoir, the temperature can be controlled from 25°C to 600°C. With liquid nitrogen as a reservoir, the temperature can be controlled from about 100°K to room temperature. The heating rate can be varied from 0.1°K/min to 200°K/min. After a baseline adjustment and calibration, the error in the measured temperature is less than 0.2°C while the error in power is generally less than 0.2 mcal/sec. In this study, DSC has been utilized to monitor the solid state transformations at a constant heating rate, to measure the heat capacity, to determine stored enthalpy, to study the thermal stability of metastable phases, as well as to obtain the activation energy of the reactions by following the Kissinger method [5]. The transition temperatures and related enthalpy changes can be obtained simply by locating the onset temperature, and then integrating the area of the transition peak in the thermogram. The kinetics of crystallization and grain growth[6] can be examined by Kissinger analysis[5] based on the peak position changes for DSC curves with different scanning rates. By plotting $\ln(S/T^2)$ vs. $(1/T)$, the Kissinger analysis yields an activation energy of the reaction (for details see ref. [5] and [7]), where S is the scanning rate dT/dt and T is the temperature of the peak in the DSC scan. In the following, I will describe in detail how specific heat measurements can be done.

As we have just discussed, the DSC signal gives directly the heat flow dQ/dt into the measured sample. Under our constant pressure experimental condition, dQ/dt is simply equal to C_p where $C_p = dH/dt$, the heat capacity at constant pressure, and H is the thermodynamic enthalpy function. In order to measure the specific heat accurately, some special

procedures must be followed. 1) Carefully calibrating the DSC for temperature and power over the temperature range of interest for heat capacity measurement and ensuring the equipment is in a very good condition. 2) Three scans, for the sample, a standard, and an empty aluminum pan need to be taken under exactly the same experimental conditions. The specific heat data for standard must be known precisely within the measured temperature range and the standard itself must be stable during the experiment. Sapphire (Al_2O_3) is usually taken as a standard. 3) To reduce the relative error of heat capacity measurement in a wide temperature range, it is necessary to divide the temperature range into several intervals of about 100°K. 4) The temperature conditions for a heat capacity measurement are isothermal at the beginning and at the end of the experiment with constant rate of scanning in between. The isothermal intervals allow the unit to equilibrate at the initial temperature and the final temperature. A reasonable scanning rate is required, usually 5 to 20 K/min, since high rates will give greater sensitivity but poorer temperature accuracy.

To calculate the specific heat, first, the base-line correction is required for both sample and standard as shown in Fig. 2.9. Second, we must subtract the empty Al pan signal from both sample and standard signals. As we know, the total heat flow for the given sample is equal to:

$$dH/dt = mC_p \cdot dT_p/dt$$

where H is enthalpy (equivalent to the heat at constant pressure) and t is time. m is sample mass; C_p is the specific heat; dT_p/dt is the programmed scanning rate of temperature. From the above equation, the specific heat

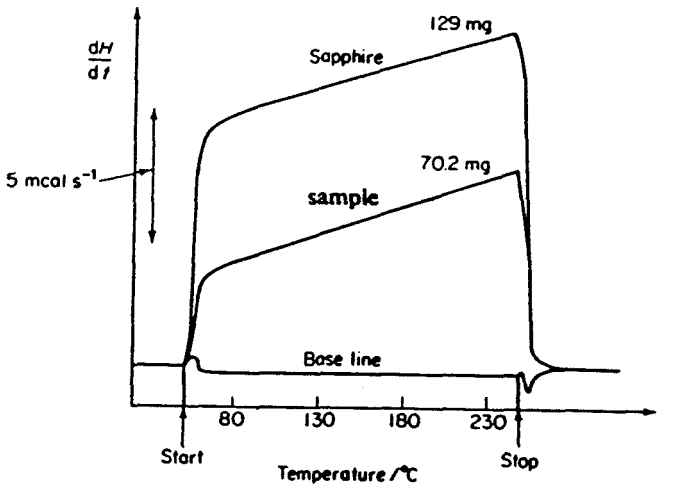

Fig. 2.9 Base-line corrections for both sample and sapphire for specific heat measurement.

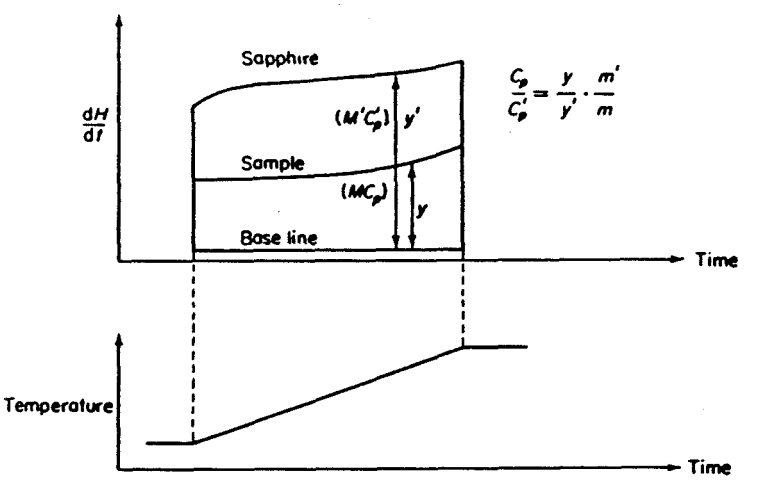

Fig. 2.10 The ratio method for determining the specific heat of samples.

value of the unknown sample can be calculated directly by ratio method as expressed in the following:

$$C_p = \frac{y \cdot m'}{y' \cdot m} C_p',$$

where C_p is the specific heat of sample and C_p' is the specific heat of sapphire. y is the amplitude of sample signal and y' is the amplitude of sapphire signal, m is the mass of sample, and m' is the mass of sapphire. Fig. 2.10 illustrates the method schematically. Following the above described procedures, the heat capacity of Zr-Al ball milled samples have been determined from 150°K to 400°K with a liquid nitrogen cooling system. By measuring the specific heat of pure metals such as Ru, it is found that the experimental value agreed with literature data within 2%.

2.3 X-ray diffraction and data analysis

Our x-ray investigations were performed with a Norelco diffractometer in a step-scanning mode using Ni-filtered CuKα radiation. The crystalline structural properties can be analyzed based on Bragg law:

$$2d\sin(\theta) = n\lambda$$

where d is the lattice spacing of crystal and θ is the diffraction angle. λ is the wavelength of the radiation souse and n is an integer. Diffraction theory predicts that the lines of a powder crystalline specimen should be exceedingly sharp, but in actual experiments, the predicted sharpness of Bragg peaks is never observed because of: 1) Instrumental broadening due to the geometry etc. of the x-ray diffractometer. For instance, finite slit widths, and variations in the plane of the specimen surface contribute to instrumental broadening; 2) overlapping of $K\alpha_1$ and $K\alpha_2$ peaks. In addition to these, in our mechanically deformed samples, there are two other factors

which contribute to the diffraction peak broadening. These are the small crystallite sizes (along with distribution of the sizes) and the distribution of lattice strain.

To analyze the crystalline grain size and lattice strain broadening, one has to obtain the "pure" line profile first. The instrument broadening profile can be derived by running a standard coarse grained Si powder. It was found that Lorentzian curves fit the line shapes of the Si pattern well. We therefore use a simple subtraction of the FWHM's (full width of half maximum of Bragg peak) to remove the instrumental broadening. The $K\alpha_1$ and $K\alpha_2$ doublet were removed by the Rachinger correction [8,9]. Furthermore, one can show that the broadening due to the crystallite size effect is independent of diffraction angle, while the inhomogeneous strain effect is proportional to diffraction angle [8,9]. Thus, we can separate these two effects and obtain the average grain size and inhomogeneous atomic strain. There are two common methods for the grain size and strain analysis, i.e., the peak breadth method which is based on line shape fitting, and the Warren-Averbach method which is based on Fourier analysis. The grain size and atomic strain in this thesis were analyzed by peak breadth method. The two most commonly assumed line shapes are the Gaussian: $G(\theta)=e^{-k^2\theta^2}$ and the Lorentzian: $L(\theta)=\frac{1}{1+k^2\theta^2}$. The FWHM of experimental x-ray diffraction peaks were obtained by fitting with Lorentzian profiles. The grain size and strain calculation show that size broadening results in a Lorentzian peak shape and strain broadening contributes a Gaussian line shape. In other words, the best match to the experimental data (or the least error to calculated values) were obtained by Lorentzian size broadening and Gaussian strain broadening fittings.

The lattice parameter for crystalline materials can be precisely determined by Nelson-Riley extrapolation plot [10] on the basis of the fact that lattice parameter a is a linear function of $(\cos^2\theta)/\sin\theta + (\cos^2\theta)/\theta$ down to very low values of θ. In practice, lines at all angles are employed in making the extrapolation to obtain the lattice parameter a.

2.4 Other experimental techniques

2.4.1 Transmission electron microscopy (TEM)

It is very important to prepare suitable thin TEM samples from the powders. Ultra-thin sections (60-70 nm) were made with a diamond knife on an ultra-microtome. The sections were retrieved from water onto grids coated with a perforated carbon substrate. The samples for TEM were prepared by grinding powders in alcohol and retrieving a very small piece onto a copper grid. The bright field and dark field images and diffraction patterns of each metastable phase, the high-resolution microstructure, and x-ray energy dispersive spectroscopy were obtained using a Philips EM 430 equipped with EDX 900.

2.4.2 Density measurement of amorphous phase

The density of amorphous phases was precisely measured using the Archimedes principle. The experiment set up consists of 1) a stand for holding a 140 ml beaker of toluene which straddles an electronic balance weigh-pan. 2) a 3-legged stand which rests on the weigh-pan with a wire support for the sample. The sample can be lowered into the toluene for wet weighing and raised for sample loading and removal. The density of toluene (C_6H_6) for a given temperature is known from standard data in the literature. All the weight measurements were taken using a Mettler AE100

balance which is a precise analytical digital balance with sensitivity of 10 μg. Each sample was first weighed in air (dry condition). It was then prepared for weighing in toluene by lowering the sample holder into the toluene bath and submersing the sample in toluene for about 10 minutes to remove any air trapped on the surface of the sample or in pores. The sample was then weighed in toluene (wet condition). Finally, the temperature of toluene was measured. With the following equation, the density of sample can be determined easily:

$$\rho_s = \frac{dw}{dw - ww} \cdot \rho_t \quad ,$$

where ρ_s is the density of sample and ρ_t is the density of toluene at the experimental temperature. dw is the dry weight of sample and ww is the wet weight of sample. The powder samples are compressed under pressure into small tablets with some porosity before the weight measurement. After weighing dw and ww carefully, the density of amorphous phase can be calculated by using the above equation.

2.4.3 Chemical analysis

The carbon and nitrogen analysis of our samples were determined by the Model 240 Elemental Analyzer. The Model 240 Elemental Analyzer accurately determines the carbon and nitrogen contents of samples by detecting and measuring their combustion products (CO_2 and N_2). Combustion occurs in pure oxygen under static conditions to guarantee a complete combustion. The combustion products are then analyzed automatically in a self-integrating, steady-state, thermal conductivity analyzer, which eliminates the tedious classical gravimateric-analysis and weighing of absorption traps. The concentration of sample components as

well as the iron contamination (i.e., metallic elements) were analyzed by Rigaku 3370 machine with the common fluorescence x-ray (EDX) method. The calibration standard data were saved in the memory of the analyzer, so quantitative analysis could be done easily. Oxygen analysis was carried out using the infra-red absorption method. The sample is put into a carbon crucible which is located at the center of an RF coil, then the sample is heated, melted, and reacted with carbon crucible. Therefore, the final product from oxygen becomes CO_2 which is detected by quantitative infrared spectrum analysis. The fluorescence x-ray analysis and the infrared absorption spectrum analysis were done at the advanced materials & technology research laboratory of Nippon Steel Corporation, Japan.

References

[1] D. R. Maurice and T. H. Courtney, *Metall. Trans.* **21A**, 289 (1990).

[2] G. B. Schaffer and P. G. McCormick, *Metall. Trans.* **23A**, 1285 (1992).

[3] C. H. Lee, *et al.*, Japanese *J. of Appli. Phys.* **29** (3), 540 (1990).

[4] *Thermal Analysis Newsletter* No.9 (Norwalk, Conn.: Perkin-Elmer Corporation) (1970).

[5] H. E. Kissinger, *Anal. Chem.* **29**, 1702 (1957).

[6] L. C. Chen and F. Spaepen, *J. Appl. Phys.* **69** (2), 679 (1991).

[7] H. E. Kissinger, *J. of Res. of the National Bureau of Standards* **57** (4), 217, (1956).

[8] B. E. Warren, X-ray Diffraction, Addison Wesley (1969).

[9] H. P. Klug and L. E. Allexander, X-ray Diffraction Procedures, 2nd ed., John Wiley and Sons, New York, (1974).

[10] J. B. Nelson and D. P. Riley, *Proc. Phys. Soc.* (London) **57**, 160 (1945).

Chapter 3

Synthesis and Properties of Metastable Phases

Commercially available pure Zr powder (99.8%, -60, +325mesh) and pure Al powder (99.95%, -40mesh) have been used as the initial materials for mechanical alloying studies. Two types of milling systems have been utilized to synthesize the metastable materials as described in the previous chapter. In some experiments, the ball milling process was periodically interrupted to remove small sample portions and the agglomeration of powder on the vial and balls was reduced or eliminated by mechanical scraping. The selected overall powder compositions for this study were varied from 0 to 60 atomic per cent of aluminum.

The structural evolution and thermodynamic properties of ball-milled powders were analyzed by x-ray diffraction (XRD), transmission electron microscopy (TEM) and differential scanning calorimetry (DSC). X-ray scans were carried out on a Norelco Philips powder diffractometer with Cu-Kα radiation (λ = 1.540598 Å). A Philips EM430 equipped with EDX detector and STEM unit was used for TEM experiments. A Perkin Elmer DSC-4 interfaced to an IBM PC computer for data collection was employed for thermal analysis. Specimens were either sealed under dry argon gas or unsealed in aluminum pans depending on the DSC experimental requirements. The chemical constitution of selected samples after ball milling were analyzed by the fluorescence x-ray (EDX) method, infra-red

absorption spectroscopy, and the thermal conductivity method after complete combustion. The results from elemental analyses indicate that the iron contamination is less than 0.5 at.%. The average composition of the samples was found to be close to the initial mixed nominal composition (within 3 at.%), though some powder becomes welded to the balls and vial during the milling process. The contamination of oxygen, nitrogen and carbon was found to be less than 1 at.%, 0.5 at. % and 0.5 at. % respectively.

3.1 Metastable phase formation

From the earlier experiments done with the SPEX 8000 mixer, the following three metastable phases were found [1] depending on the overall composition of the powder mixture, as shown in Fig. 3.1.

(1) A nanocrystalline supersaturated hcp α-Zr solid solution for Al concentration less than 15 at.% (atomic per cent) was observed.

(2) A completed amorphous phase for Al concentrations between 15 at.% and 40 at.% was obtained.

(3) A metastable nanocrystalline phase with an fcc structure and lattice parameter a=4.6093 Å was found for Al concentration equal to 50 at.%.

The third "*metastable fcc*" phase was initially identified to be a new metastable ZrAl metallic alloy phase. Later by the study of a ball milled Er-Fe system [2], we realized that the steel vials sometimes do not remain hermetically sealed during the milling process. If the air sealing failed, a nitride phase was found to form under the certain conditions. The presence of a good nitride-former (such as Er, Zr, etc.) and a catalyst (such as Fe, Ni, etc.) for the dissociation reaction of nitrogen molecules in the studied material can lead to nitride formation during the high energy ball milling. A detectable amount of nitride phase may be obtained if there is a

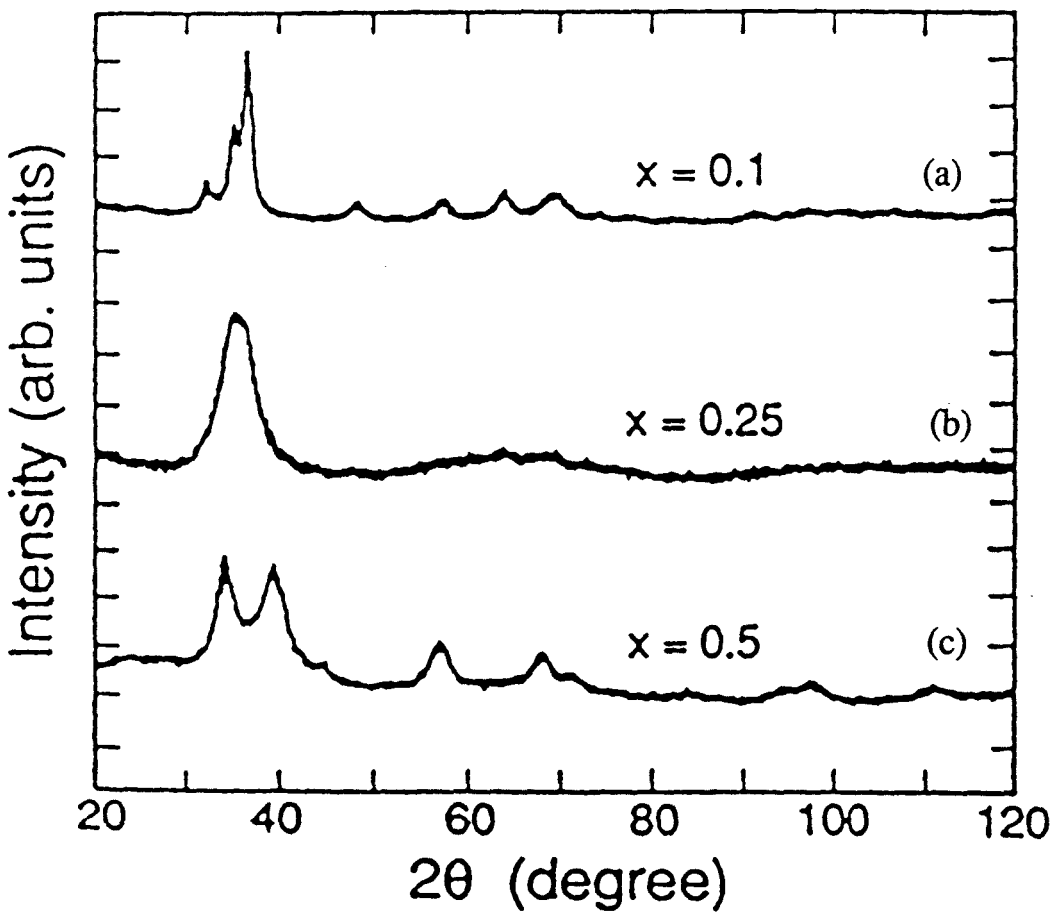

Fig. 3.1 X-ray diffraction patterns show the different structure obtained after 15 hrs. ball milling with Spex 8000 mixer for the following three compositions: (a) supersaturated solid solution α-Zr for x_{Al} = 0.1; (b) an amorphous phase for x_{Al} = 0.25; (c) a metastable fcc phase for x_{Al} = 0.5.

continuous supply of nitrogen caused by a leak in the seal. For example, an fcc nanocrystalline ErN phase was found by mechanical alloying of the Er-Fe system. After this discovery, I realized that it is necessary to re-examine the "*metastable fcc*" phase found in Al-Zr since Zr is an easier nitride-former and the "ZrN" phase has an fcc structure. In addition, the lattice parameter of $Zr_{(1-x)}N_x$ in the literature is a=4.585 Å for x=0.37 while the lattice parameter of the "*metastable fcc*" phase we obtained by MA is a=4.609 Å. The difference in lattice parameters between the literature value for ZrN and the experimental value observed could be due to differing amounts of nitrogen dissolved in the ball milled sample since the ZrN intermetallic compound is not a stoichiometric phase. Moreover, the same set of experiments (as shown in Fig. 3.1) was done with the Super-MISUNI milling machine where the milling cell pressure can be measured and controlled in this system. To prevent the air contamination, the pressure in the sample vessel was kept greater than one atmosphere during the milling time. The sequence of phases obtained as a function of Al concentration for the experiments done with Super-MISUNI machine is shown in Fig. 3.2. Instead of observing three metastable phases, there are only two metastable phases obtained in the absence of air contamination for samples with compositions $x_{Al} \leq 55 at.\%$. Therefore, the fcc phase appearing in Fig. 3.1 is not a ZrAl metastable phase but rather a $Zr_{(1-x)}N_x$ stable phase formed by reaction of Zr powder with nitrogen gas.

From the Al-Zr equilibrium phase diagram shown in Fig. 3.3, it is known that the equilibrium solubility of Al in α-Zr solution is less than 2 at.% at temperatures below 500°C. Futher, there are several intermetallic compounds appearing with different alloy compositions. The analyses of

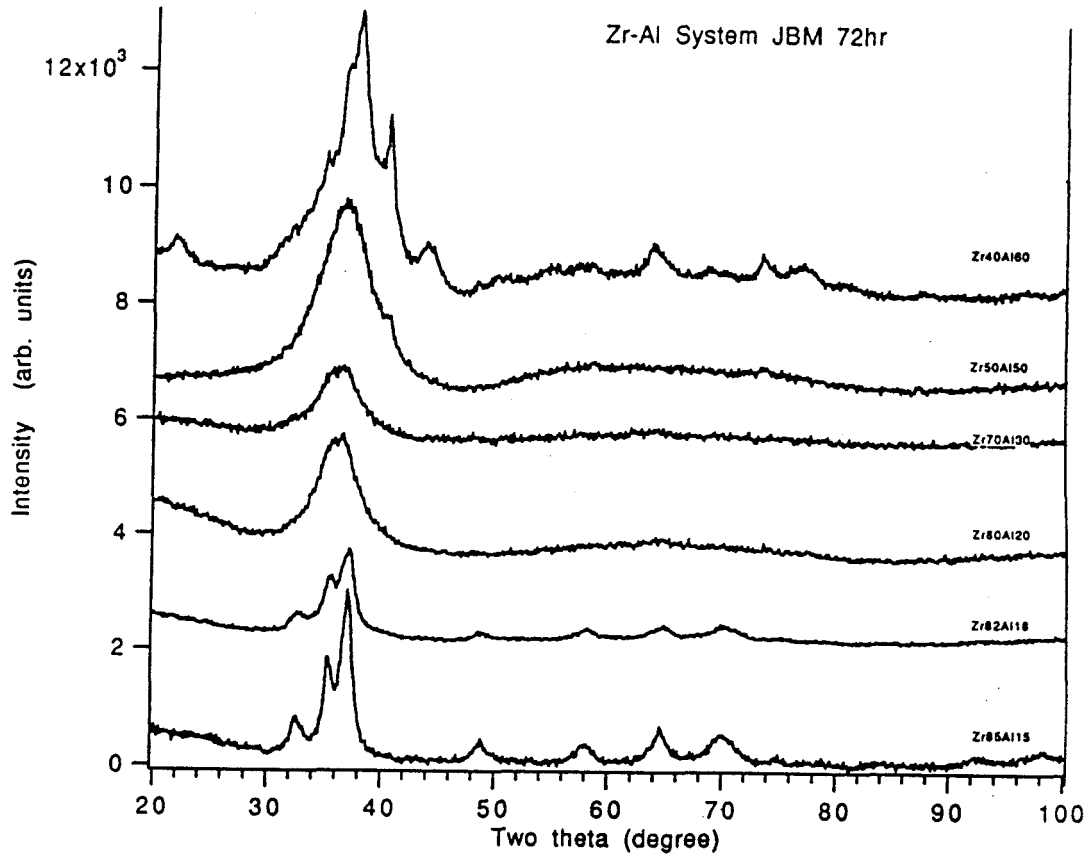

Fig. 3.2 X-ray diffraction patterns show the structure changes as a function of composition for samples after 72 hrs. ball milling with Super-MISUNI machine.

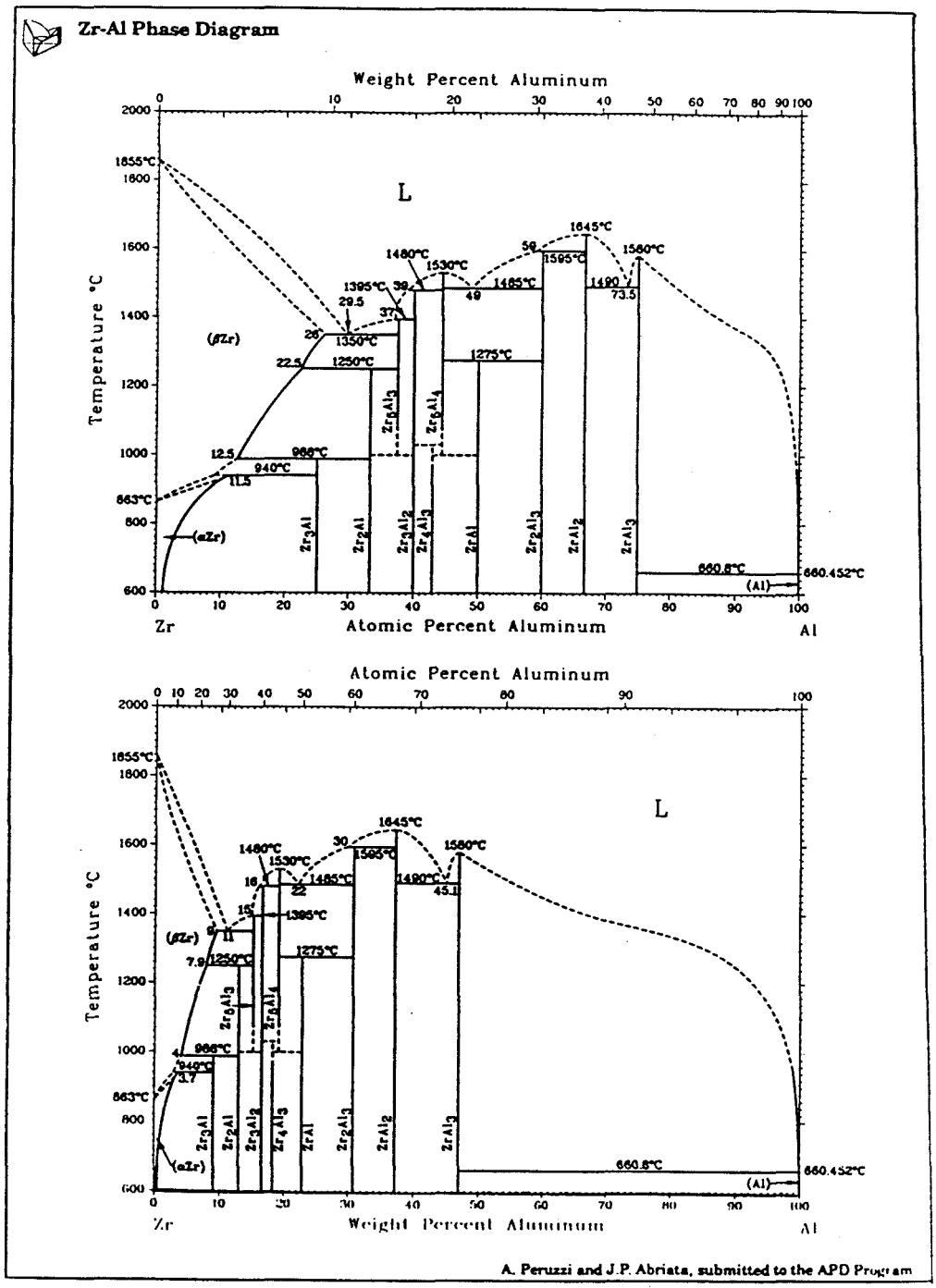

Fig. 3.3 Thermodynamic equilibrium phase diagram of Zr-Al binary system.

ball milled samples with x-ray diffractometry indicated that none of the thermodynamically stable intermetallic compounds found in the equilibrium phase diagram are formed during mechanical alloying of the mixtures of Al and Zr elemental powders. Though the equilibrium solubility of Al in α-Zr is very small at temperatures below 500°C, the solubility of aluminum can be enhanced by ball milling to at least 15 at.% without the formation of the stable Zr_3Al compound phase. In contrast to the intermetallic compound phases found in equilibrium phase diagram, a metallic glass structure is obtained for aluminum concentrations of $20at.\% \leq x_{Al} \leq 55at.\%$.

In addition to the investigation of metastable phase formation as a function of composition, the structural evolution with ball milling time for a given composition has been studied as well. The x-ray diffractograms of the sample $Zr_{90}Al_{10}$ at different milling times is shown in Fig. 3.4. As we can see from the x-ray curves, the Bragg peaks of α-Zr solid solution phase become broader and move toward the high angle with the increase of ball milling time. These structural changes are associated with the reduction of grain size, the development of atomic strain, and the shrinkage of lattice parameter with Al dissolution. These results can be understood by the following considerations. Because the solute aluminum has a smaller atomic size than Zr, and the fact that Al atoms substitute for Zr atoms upon forming a solid solution, the lattice parameter of α-Zr phase should decrease with increasing Al solubility. The severe deformation during mechanical alloying reduces crystallite size and increases the densities of structural defects [3,4,5]. A quantitative analyses of the lattice parameter, the atomic strain, and the average grain size, after mechanical deformation for solid

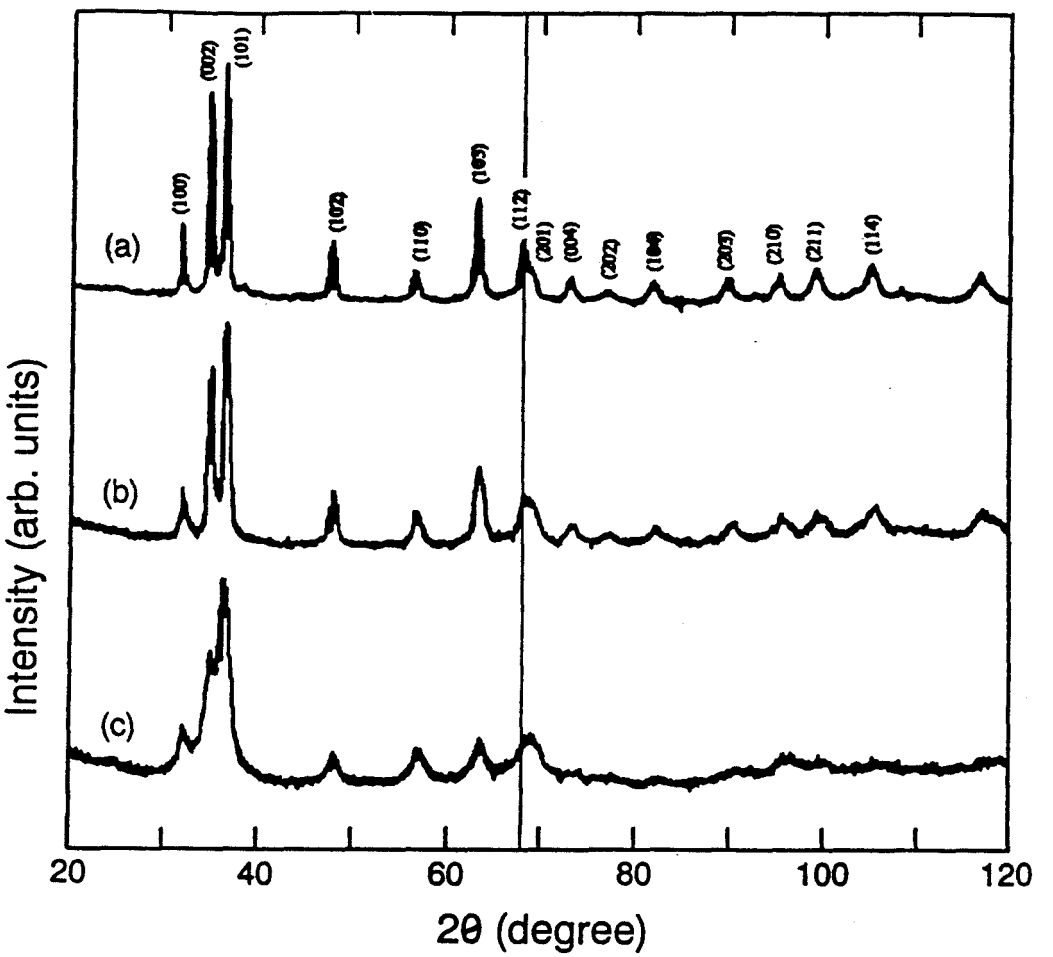

Fig. 3.4 X-ray diffraction patterns of ball milled powder with initial average composition $Zr_{90}Al_{10}$ after ball milling time: (a) 2 hr., (b) 8 hr. and (c) 20 hr.

solutions with different compositions will be given in Section 3.3. Figure 3.5 shows the structural evolution of a $Zr_{75}Al_{25}$ sample as a function of ball milling time. After 2 hour's ball milling (shown in Fig. 3.5(a)), the (111) Bragg peak associated with fcc aluminum is still detectable. By continued milling to 8 hours (shown in Fig. 3.5(b)), the process leads to the disappearance of (111) Al peak and a shift of α-Zr peaks towards higher angle (when compared with the pure Zr). This indicates that Al is dissolved in a Zr-rich solid solution, causing the lattice parameter of α-Zr phase to shrink. Following ball milling to 20 hours, the sample transforms completely to an amorphous phase (shown in Fig. 3.5(c)). TEM observations show the same metastable phases as obtained by x-ray diffraction. The TEM images of nanophase and amorphous phase are shown in Fig. 3.6 and Fig. 3.7.

3.2 Thermodynamic properties

As mentioned in Chapter 1, structural changes in a material can result in a change of its properties. Therefore, we may expect thermodynamic property changes in the nanocrystalline supersaturated α-Zr solid solutions since the crystal refinement to nanometer-sized grains leads to an increase in the fraction of grain boundaries, and therefore an enhanced contribution of grain boundary properties. In fact, changes in thermodynamic properties (such as specific heat) of nanocrystalline materials in comparison to polycrystalline for pure metals has been reported [4][6]. For nanocrystalline Pd (6 nm) made by gas condensation method, the excess specific heat varies from 29% (at 150°K) to 53% (at 300°K). In the case of 8nm Cu, the increase of specific heat is 9% (at 150°K) and 11% (at 300°K). This enhancement of specific heat has been associated with an increase in the configurational and

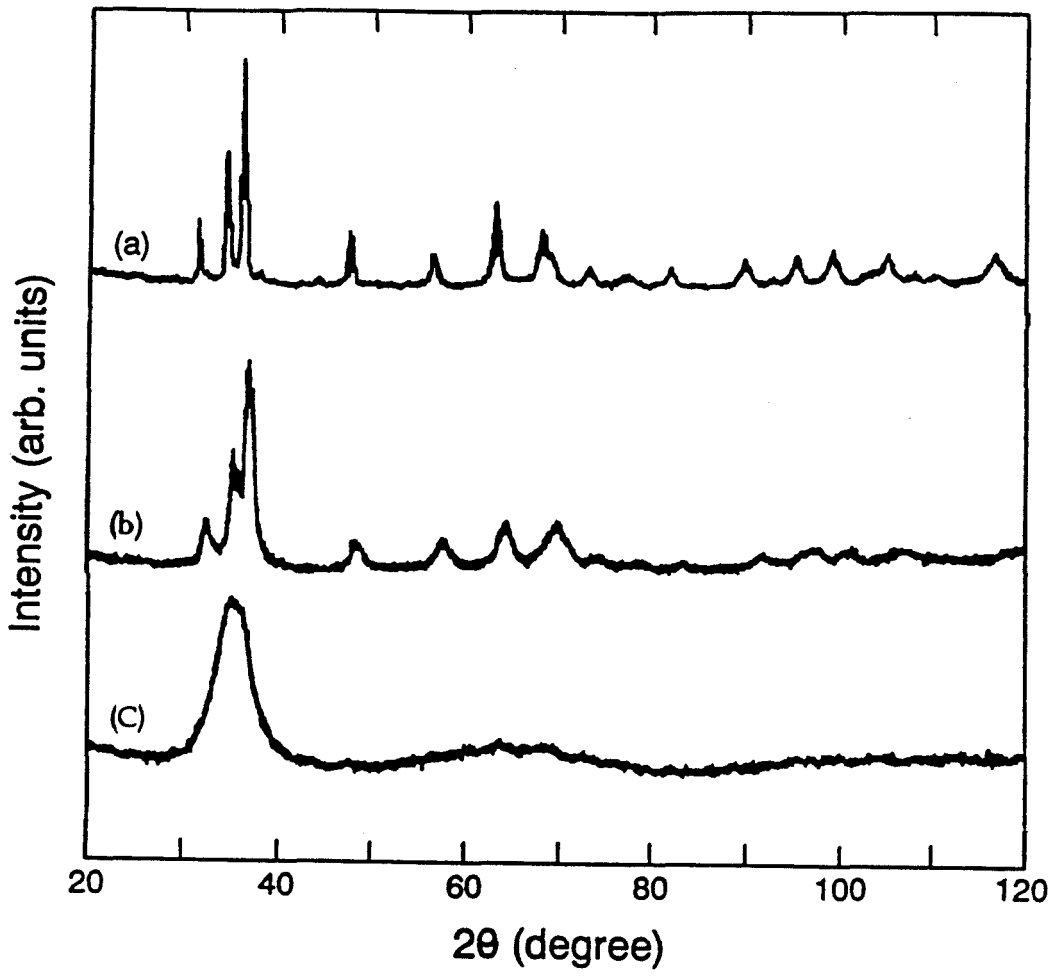

Fig. 3.5 X-ray diffraction patterns of ball milled powder with initial average composition $Zr_{75}Al_{25}$ after different milling time: (a) 2 hr., (b) 8 hr. and (c) 20 hr.

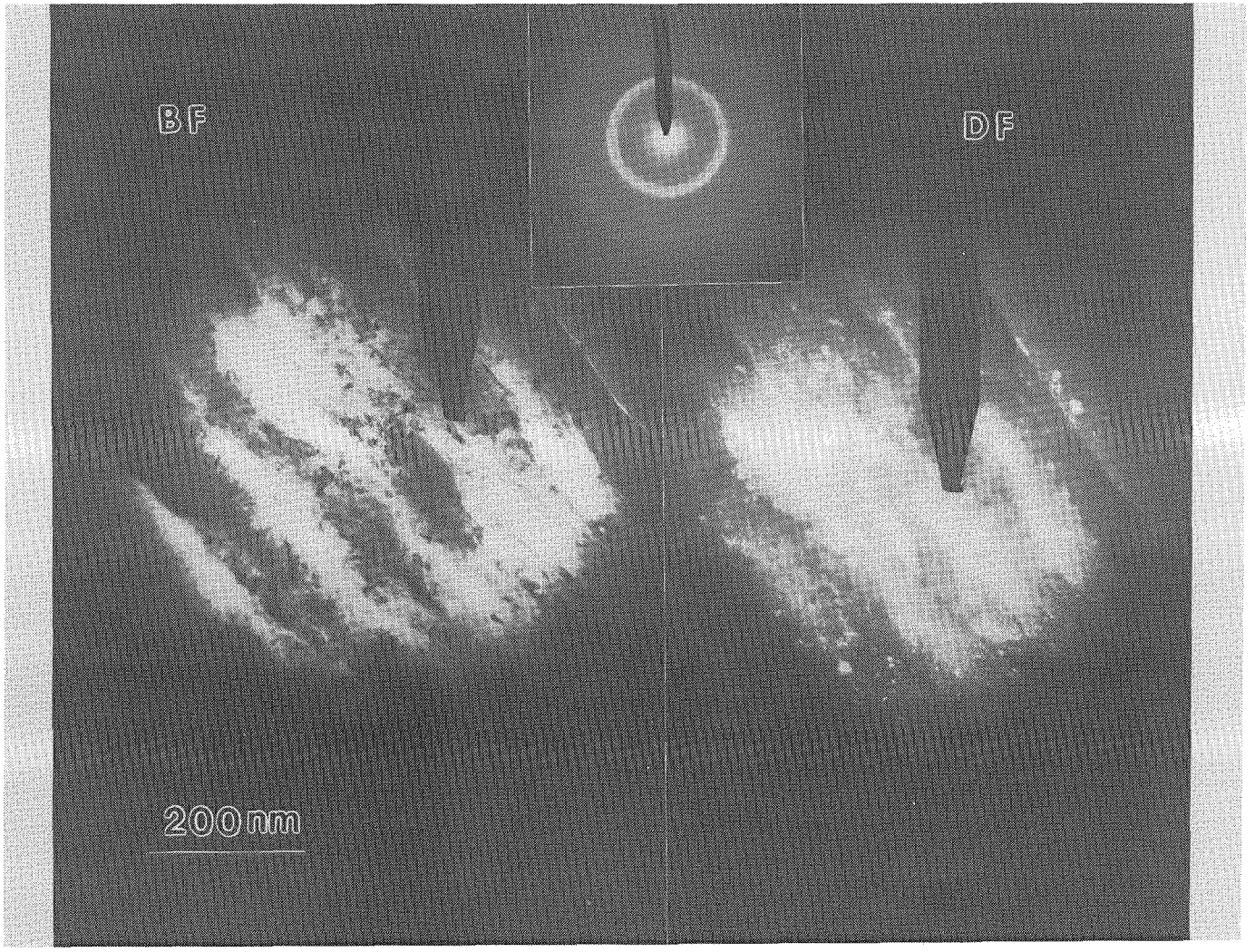

Fig. 3.6 TEM results of nanocrystalline supersaturated solid solution (bright field image, dark field image and diffraction pattern).

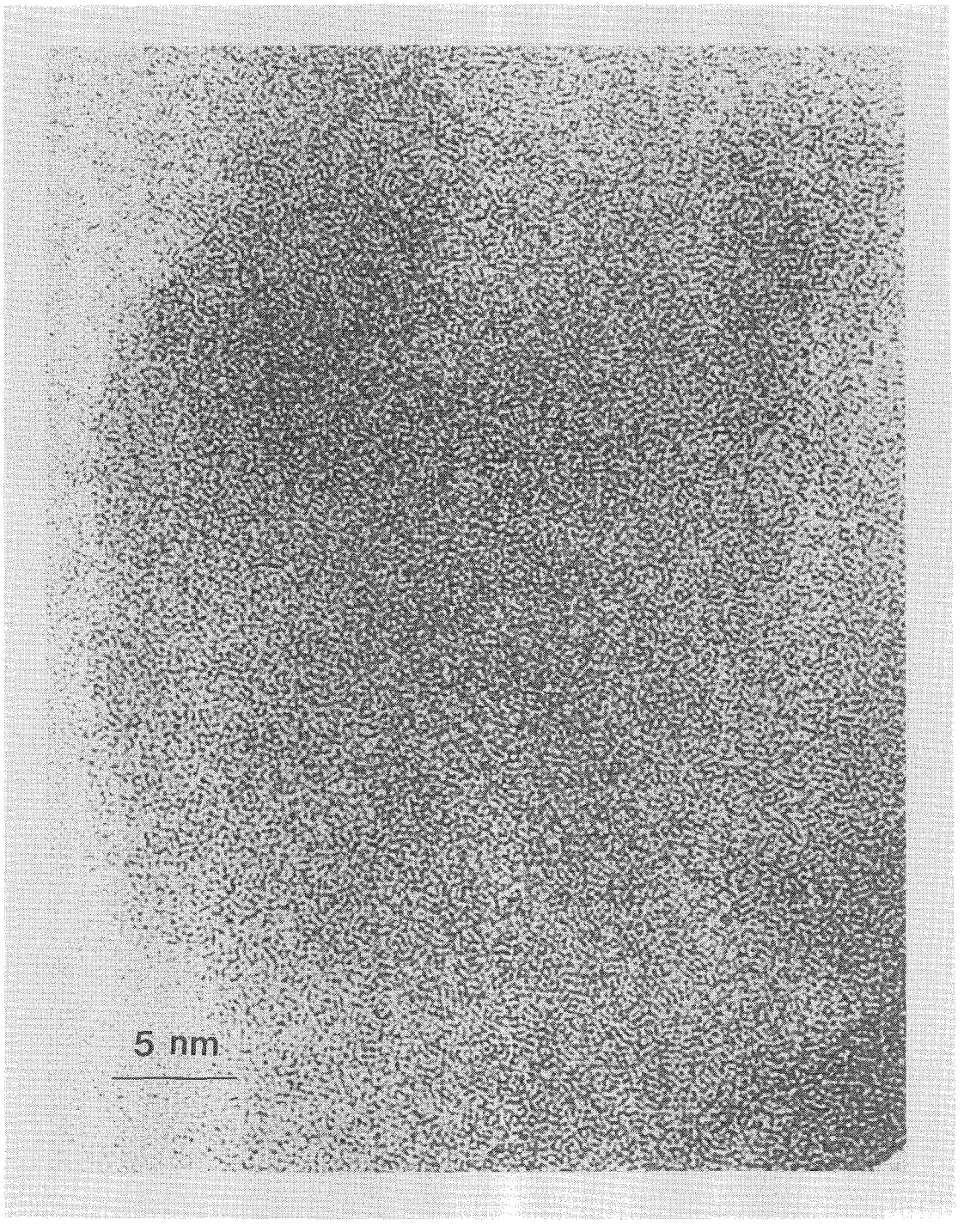

Fig. 3.7 High-resolution TEM image of an amorphous phase.

vibrational entropy due to grain boundary disorder and with lattice defects. For nanocrystalline Ru (15 nm) made by mechanical milling, the increase of specific heat was found to be 15%-20% in the temperature range of 150°K to 300°K. This was explained in terms of large anharmonic atomic vibrations within the grain boundary component and lattice defects formed during milling. Lu *et al.* [7] have also reported thermal expansion and specific heat data for a nanocrystalline Ni-P alloy. They give experimental comparisons of thermodynamic data for crystalline, amorphous, and nanophase alloys with the same composition. The thermal expansion coefficient of the nanocrystalline phase was enhanced by 56.3%, while that of the amorphous phase is only 3.6 % greater than that of a coarse grained crystal. The specific heat, C_p, of the nanocrystalline material was found to increase linearly with the temperature from 310°K to 400°K, and the value was 12.3 % larger than that for coarse grained crystals. The C_p enhancement of the amorphous phase in comparison with the coarse grained crystalline state is only 7.7 %. In their study, the nanocrystalline Ni-P alloy with 9 nm grain size was prepared by using the method of crystallization from an amorphous phase.

With our Perkin-Elmer DSC-4 equipment, the specific heat C_p of nanocrystalline supersaturated solid solution and amorphous materials for Al-Zr system have been measured in the temperature range from 150°K to 400°K. The detailed experimental procedures for heat capacity measurement were described in Chapter 2. Our specific heat results as a function of Al concentrations have similar behavior within the measured temperature range. The data at 300°K were discussed here. Fig. 3.8a shows the direct measurement C_p data from the experiments and the linear plot is calculated from the idea mixtures of Al-Zr alloys. The excess heat capacity ΔC_p in

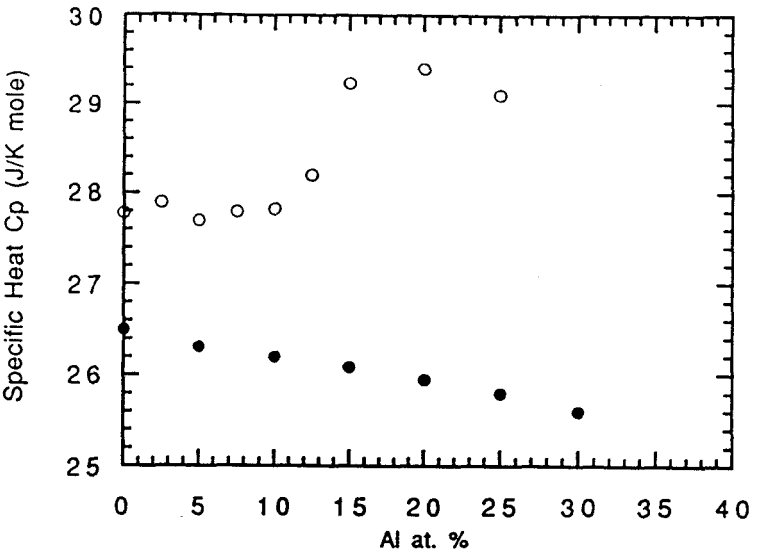

Fig. 3.8a Open circles are the experimental specific heat data of ball milled metastable specimens. Solid dots are the calculated data by assuming an ideal Al-Zr solid solution.

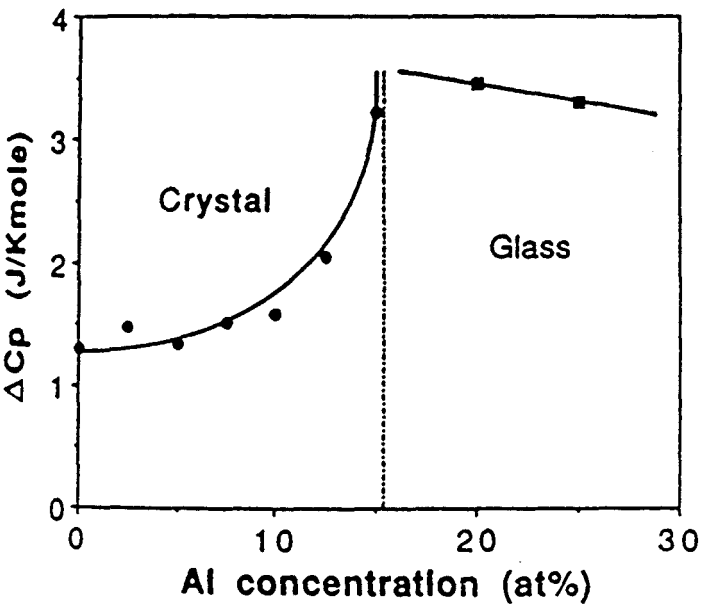

Fig. 3.8b Excess heat capacity ΔC_p as a function of Al concentration up to 25 at. %. Data were measured at 300 K from DSC. The solid line is a fitting for experimental points.

comparison to a physical mixture of Al and Zr as a function of Al concentration up to 25 at.% is shown in Fig. 3.8b. The excess heat capacity is due to the chemical and topological disorder associated with grain boundaries and defects in the crystal lattice. Due to the significant reduction of the grain size and the related incorporation of high-angle grain boundaries and defects, an increase in C_p of 5 % is found for pure Zr. Alloying with Al leads to the formation of a metastable disordered solid solution accompanied by an additional increase in anharmonicity of the Zr crystal lattice as compared with the stable ordered compounds. This results in a further increase of C_p, reaching a value of 12 % for x_{Al}= 15 *at.%* compared to a physical mixture of Al and Zr. The more dramatic increase of C_p near the composition where an amorphous phase is found, suggests the possibility that amorphization may be associated with some kind of instability as Fecht and Johnson proposed [8].

In addition to the specific heat, the normal DSC temperature scans from 50°C to 600°C with a constant heating rate of 20 K/min have also been used to study the relaxation, recovery, grain growth, and phase transformation behavior of the supersaturated solid solutions and amorphous samples. It is known that mechanical alloying or mechanical milling creates a significant population of various types of defects within the crystallites. The experiments show that the relaxation or recovery of these defects usually starts at about 100°C and covers a wide temperature range for almost all of our ball milled samples. The signal arising from this exothermic recovery is relatively weak and poorly defined compared with signals arising from first order phase transformations. Therefore, if a phase tranformation (such as crystallization) signal follows or overlaps with a

relaxation peak, it may become difficult to define the phase transformation peak precisely because of the presence of the broad underlying relaxation peak. The DSC temperature scan for the ball milled solid solution of $Zr_{85}Al_{15}$ (a) and the scan for amorphous $Zr_{70}Al_{30}$ specimens (b) are shown in Fig. 3.9. The two samples have very similar behaviors upon the heating in the DSC. By using x-ray diffraction to analyze the structural changes occurring in both samples following DSC scans, the final reaction products for the solid solution samples were found to be equilibrium α-Zr solid solution and the intermetallic compound Zr_2Al and Zr_3Al_2 phases. The ordered fcc Cu_3Au type Zr_3Al phase which appears in the equilibrium phase diagram was not observed. This is probably due to kinetic constraints for forming this ordered phase from a severely deformed and disordered sample under DSC experimental conditions. Although the crystallization peak of amorphous phase in Fig. 3.9(b) is relatively sharper than the peak in Fig. 3.9(a), the peak positions are around the same temperature. This makes it very difficult to tell from the DSC curves if there is any amorphous phase in the solid solution samples. Perhaps, it is possible that the peak in Fig. 3.9(a) is actually the overlap of two reaction signals which arise from the formation of the equilibrium compound (from the solid solution) and the crystallization of partially amorphized sample. By integrating the exothermic peak in the DSC scans for samples with different compositions, the total enthalpy released from each sample can be plotted as seen in Fig. 3.10(a).

There are at least two possibilities to explain the enthalpy data obtained from DSC experiments. One has been reported and discussed by En Ma *et al.* [9]. They found an abrupt change in the slope of two sets of enthalpy data

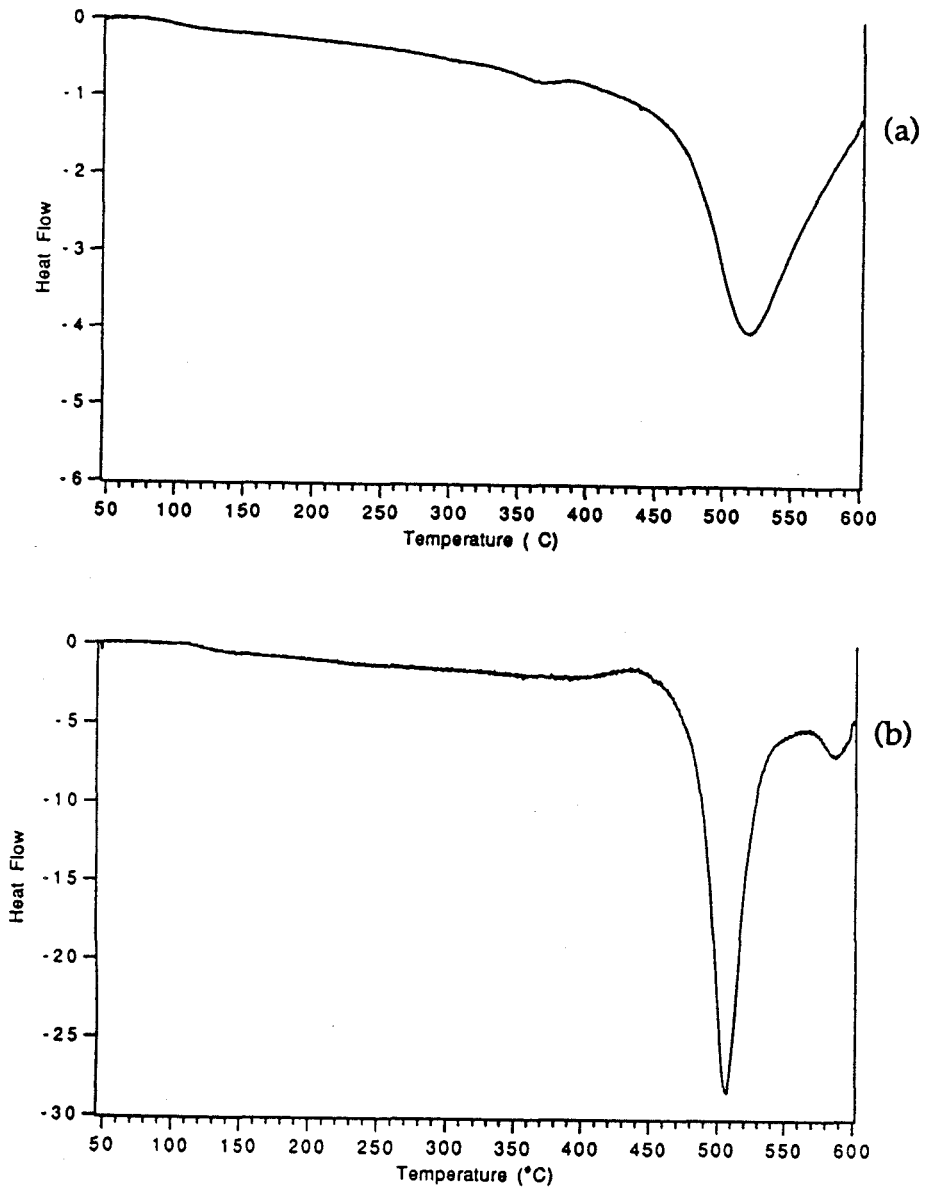

Fig. 3.9 Typical DSC temperature scans for both nanocrystalline supersaturated solid solution (a) and amorphous phase (b).

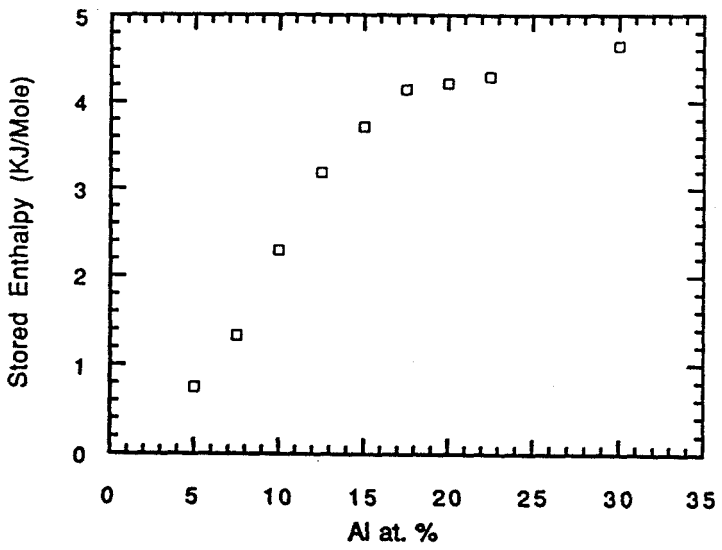

Fig. 3.10a The enthalpy of the exothermic peak measured by DSC for ball milled samples as a function of Al concentration.

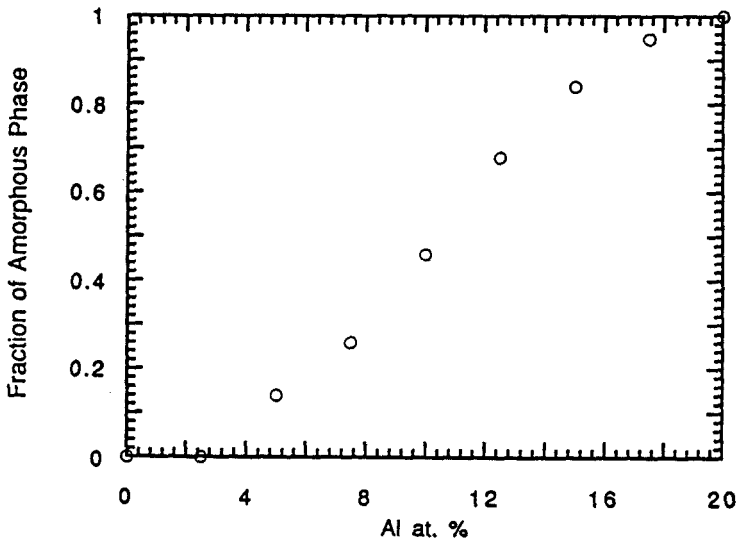

Fig. 3.10b Percentage of amorphous phase as a function of Al concentration by assuming the enthalpy is released from the crystalliztion reaction of amorphous phase.

points (solid solution and amorphous) and believe that the cusp corresponds to the composition where the enthalpy of solid solution is equal to the enthalpy of amorphous phases. Furthermore, based on this interpretation, they conclude the amorphization by MA in Al-Zr occurs under a polymorphous constraint rather than by nucleation and growth under metastable two-phase equilibrium. First of all, as shown in Fig. 6.2, the x-ray trace of the amorphous sample presented in their paper does not appear to be that of a single phase. A real polymorphous transformation should lead from a single crystalline solid solution phase to single amorphous phase. Secondly, there are large error bars in the released enthalpy as determined from DSC experiments because of the presence of the broad relaxation peak (as discussed above). Another possibility is to concern the existence of an amorphous phase in the solid solution samples. Assuming the total enthalpy is mainly due to the crystallization of an amorphous phase in the sample, the fraction of amorphous phase formed by ball milling can be derived as shown in Fig. 3.10(b). This plot may over estimate the amount of amorphous phase, but the qualitative behavior should be right if the amorphous phase fraction is determined by a metastable two-phase equilibrium. A detailed discussion of the possibility of polymorphous amorphization by MA will be given in Chapter 6. The point here is that the enthalpy data from DSC experiments cannot alone yield an unambiguous conclusion regarding the mechanism of the phase transformation during MA. Obviously, other experimental methods such as transmission electron microscopy, small angle x-ray scattering or Debye temperature measurements, are necessary to determine the mechanism by which transformation to an amorphous phase occurs during MA of Al-Zr.

3.3 Structural properties

The structure characterization of both nanocrystalline supersaturated solid solutions and amorphous samples has been done with x-ray diffraction and TEM. The qualitative analysis of metastable phase formation by x-ray diffraction was given in Section 3.1. The quantitative analysis of lattice parameters, lattice strains and grain sizes of the solid solution phase will be discussed in the following section based on the analytical methods described in Chapter 2.

3.3.1 Lattice parameter and atomic volume

Before showing the experimental data, let us first review the basic concepts of solid solutions and ideal solid solutions. If one component is dissolved in another component (or other components) without changing the structure of the host component, the resulting alloy is called a solid solution. The solute solubility depends on the interactions among all component atoms. It is affected by such factors as chemical affinity or atomic size difference. If the mixing process of solid solutions does not involve a change in enthalpy, volume, etc., the solution is called ideal solution. For ideal solutions,

$$V = x_A V_A^o + x_B V_B^o \ ,$$

where V is the total volume; x_A is the concentration of element A and V_A^o is the mole volume of pure A; x_B is the concentration of element B and V_B^o is the mole volume of pure B. The lattice parameter of ideal solution follows Vegard's law which for a binary system is:

$$a = x_A a_A^o + x_B a_B^o \ ,$$

where a is the lattice parameter of solid solution, a_A^o is the lattice parameter of pure A, and a_B^o is the lattice parameter of pure B. Hence, the properties

for an ideal solution are very easy to obtain from the properties of each component.

The experimental data for the lattice parameter as a function of Al concentration is shown in Fig. 3.11. The lattice parameter decreases with increasing of the nominal Al concentration since the atomic radius of Al is smaller than that of Zr and the Al atoms substitutionally occupy the Zr sites. There is no question about the solubility enhancement of Al in α-Zr by the non-equilibrium ball milling process, but it is not clear if all the aluminum atoms substitutionally and homogeneously occupy the lattice sites. It is hard to determine the exact solubility in α-Zr from lattice parameter data when the experimental error becomes large due to the peak broadening which arises from severe deformation and small grain size. It is probable that, either Al grain boundary segregation or amorphous phase formation exist in the samples with concentrations $x_{Al} > 10 at.\%$. In Fig. 3.12, atomic volume data are plotted as a function of composition for the different phases. The experimental data for the solid solutions were obtained from the lattice parameters in Fig. 3.11. The linear extrapolation curve is from the calculated atomic volume by assuming an ideal solution model. The data for the amorphous phase were obtained by weighing samples in toluene and air, on the basis of the Archimedes principle (see Chapter 2 for detailed descriptions). The atomic volumes of equilibrium compound phases are taken from literature [10] data. The remaining two points (marked by square) are for an idea phase of amorphous Zr and experimental data on Zr_3Al amorphous prepared by ion irradiation[11]. The experimental data for the α-Zr solid solution shows a deviation from ideal solution behavior when $x_{Al} > 10$ *at.%* . This could be a sign of the existence of a

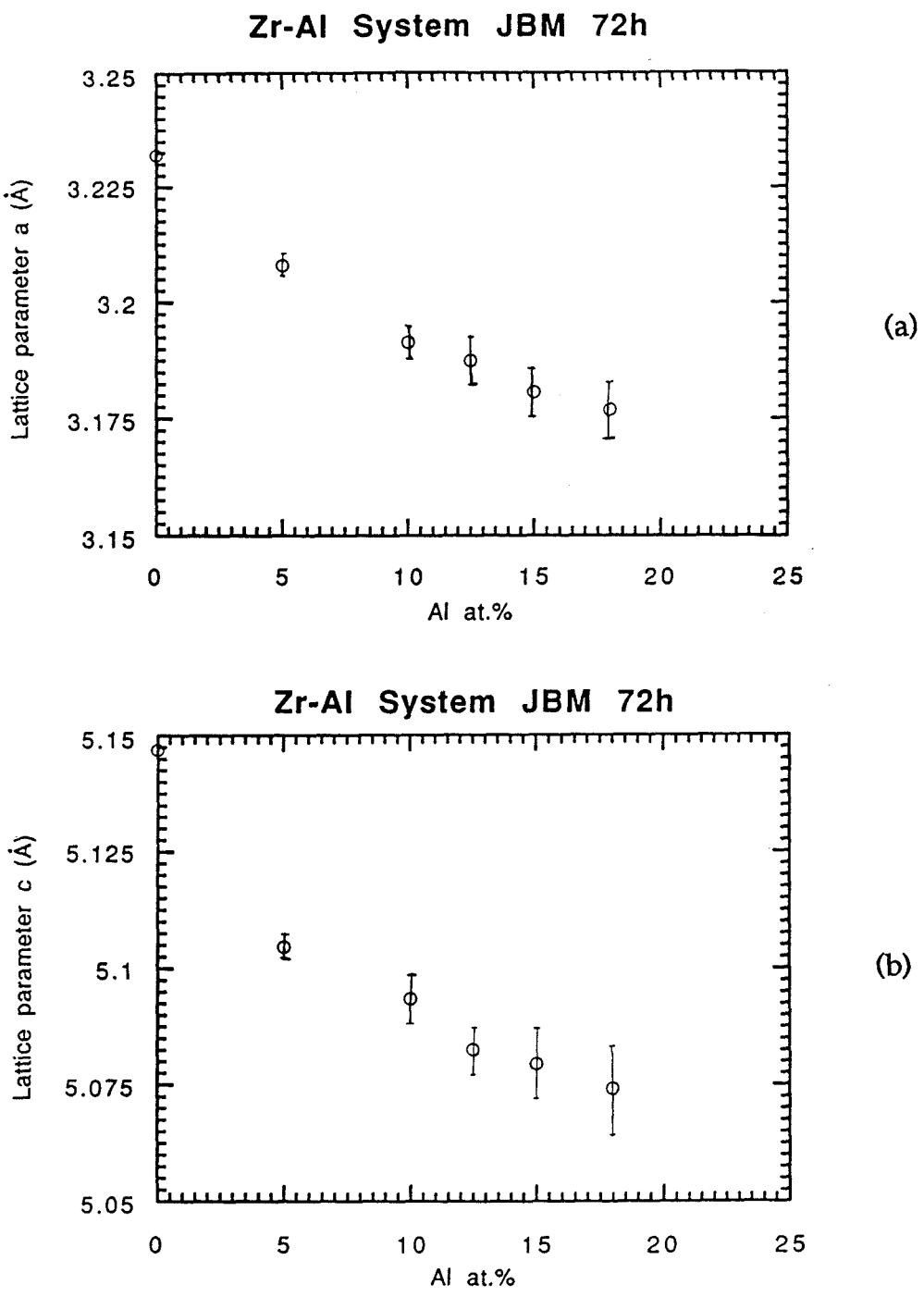

Fig. 3.11 Experimental lattice parameters for nanocrystalline supersaturated solid solution: (a) lattice parameter *a* and (b) lattice parameter *c*.

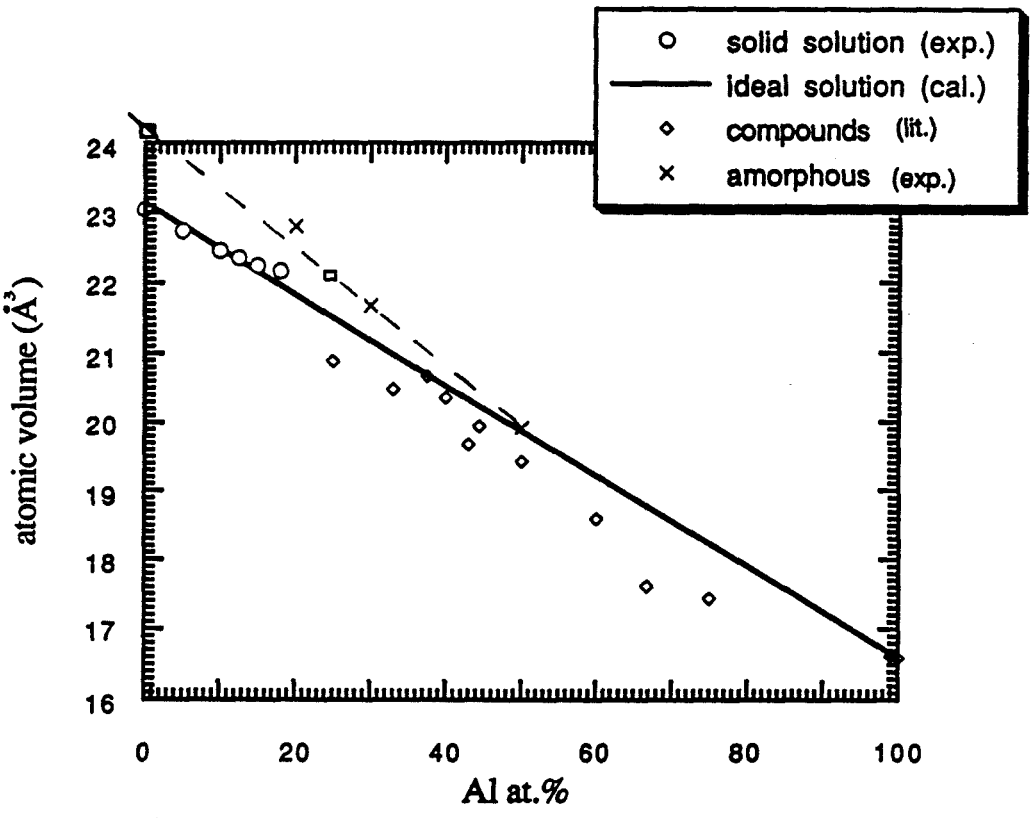

Fig. 3.12 The atomic volumes for different phases were plotted as functions of Al concentrations.

small amount of amorphous phase. In fitting the amorphous data with a dashed line, we see a decrease of the atomic volume difference between the crystal and amorphous phase with the increasing of Al concentration. This result seems consistent with the glass forming ability of the alloys. The highest crystallization temperature obtained for an $Zr_{50}Al_{50}$ amorphous alloy (as shown in Chapter 4) may be associated with its smallest density difference from the crystalline phase.

3.3.2 Grain size changes with composition

The experiments have shown that the final grain size of powders processed by ball milling saturate at a steady value with no further refinement occurring after a certain milling time. In studying ball milling of pure metals and some "CsCl-type" intermetallic compounds, Hellstern *et al.* [4] have considered the mechanisms for crystal refinement. Plastic deformation occurs by the glide of dislocations when a critical stress is applied. Based on the Hall-Petch relationship, a very high stress is expected to maintain plastic deformation via dislocation movement for nanometer-sized crystalline materials. As such, a small crystal grain size itself provides a limit for the glide of dislocations and therefore for further crystal size refinement since the force required can not ultimately be provided by ball milling. From a different point of view, Eckert *et al.* [12,13] suggested that the minimum grain size achievable by mechanical milling is determined by the minimum distance that can be sustained between dislocations in a dislocation pile-up. This idea has also been extended to understand the minimum grain size for binary solid solution systems such as Fe-Cu. The model is nevertheless not general. For example, the model does not apply to the Al-Zr system even at the qualitative level. It turns out from

experiments that the mechanisms of crystal size refinement for binary alloys become more complex because of the chemical interactions between two components. Experiments show that the ultimate grain size depends on not only the structural defects but also the chemical compositions of the alloys. Fig. 3.13 shows the grain size as a function of nominal composition for ball milled supersaturated α-Zr solid solutions. For pure Zr, the average microcrystallite size has been reduced to 14 nm after ball milling. The grain size decreases linearly with increasing average Al concentration in the samples. For $Zr_{82.5}Al_{17.5}$ sample, the measured average crystalline grain size is reduced to about 5 nm. Similarly to the other property analysis, the broader the Bragg peak is, the larger the experimental error becomes. Therefore, it is not clear whether the average grain size can continuously decrease to ultimately reach that of an amorphous phase (1 to 2 nm). The two cross marks in Figure 3.13 indicate that the grain size can be changed reversibly by varying the composition of ball milled samples. The experimental details for these two points are as follows: 1) ball milling the $Zr_{90}Al_{10}$ sample from a mixture of Zr and Al elemental powders to get a steady-state grain size indicated by the open circle at $x_{Al} = 10at.\%$. 2) Adding pure Zr to the as-milled powder to make the average composition equal to $Zr_{95}Al_5$, then continue ball milling for another 20hrs. to get a grain size indicated by the cross sign at $x_{Al} = 5at.\%$. 3) Adding pure Al powder to the milled $Zr_{95}Al_5$ sample to change the average composition to $Zr_{90}Al_{10}$, then continue milling for 20hrs. to obtain the final grain size as plotted by the second cross sign at $x_{Al} = 10at.\%$. This set of experiments reveals that the average grain size depends in a reversible manner on the Al concentration. Consistent with these results on Al-Zr, similar reversible behavior of grain

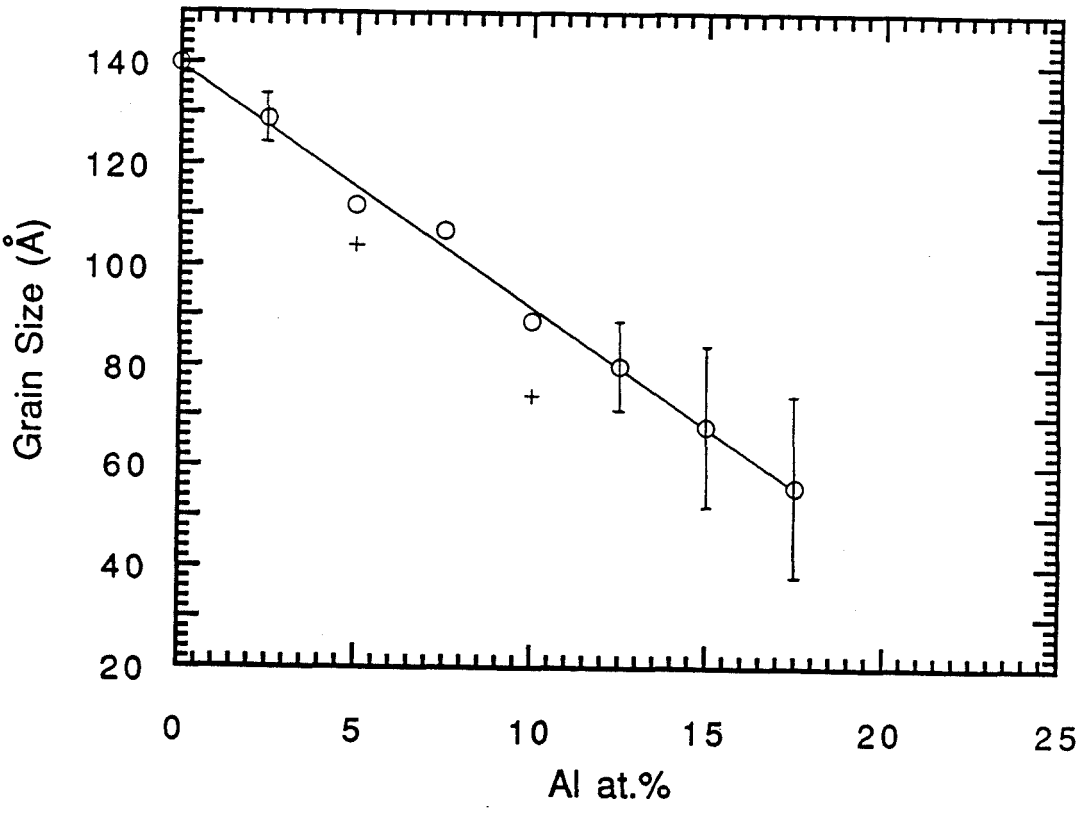

Fig. 3.13 Grain size as a function of Al concentration (The two cross marks were obtained by reversible changing of Al compositions.).

size has been obtained during mechanical alloying of CuNb [14] and FeCu [13,15] systems. By changing the composition reversibly, the final average steady-state grain size changes reversibly as well. The deviation of cross mark from the fitted straight line is perhaps due to the additional Fe contamination which arises from the increased ball milling time. For the Al-Zr system, the ball milling of an initial Zr_2Al compound and Zr mixtures has also been studied to compare with the MA of pure elemental powders. The same results of the average grain size and atomic strain were found in experiments on samples with the same overall composition. Moreover, the DSC scans showed the same thermal stability. The experiments indicated that the ultimate grain size by MA is determined mainly by two factors: 1) the competition between the severe plastic deformation (structural defects) induced by mechanical milling and the recovery behavior of the material; 2) the chemistry of the material which is composition dependent. For a given milling system, the applied stress is fixed by the geometry of the vial, the vibration frequency, etc. The stain rates obtained in powder grains depends on both the applied stress and on the materials properties. An increase in strain rate generally increases the flow stress of a material. However, our experiments show generally that for a given system and fixed experimental conditions, a steady-state condition with an ultimate steady state grain size is obtained by MA.

3.3.3 Atomic strain behavior

It is known that the defects (dislocations) created within the crystals by mechanical deformation as well as atomic strains associated with atomic size mismatch in solid solutions both lead to an increasing level of atomic strain within the nanocrystallites. The analyzed rms strain from x-ray

diffraction experiments is plotted in Fig. 3.14 as a function of the composition for supersaturated solid solutions. A normal parabolic behavior expected for solid solutions is obtained. The maximum value for the strain reaches about 0.8 % which is of the same order for ball milled pure Ru metal and much smaller than that of ball milled AlRu compound[4]. To compare with the atomic strain levels in an ordinary solid solution, the atomic strain has been calculated with a generalized model using the Lindemann criterion for a disordered binary alloy system [16] and plotted as a solid line in Fig. 3.14. In the model, the total mean square displacement is obtained from the sum of two parts. One is the thermal vibration part which is temperature dependent,

$$\langle (\Delta r)^2_v \rangle = 9\hbar^2 T / M k_B \Theta^2 \quad ,$$

where T is the temperature and M is the mass. Θ is the Debye temperature of the alloy.

Another is the static part which is atomic size and composition dependent,

$$\langle (\Delta r)^2_s \rangle = C_1 C_2 (r_1 - r_2)^2 \quad ,$$

where C_1 and C_2 are the atomic concentrations for each component. r_1 and r_2 are the radii of each kind of atom, respectively.

Essentially, the experimental results are reasonably consistent with the calculated curve. The difference between experiment and the calculation for pure Zr and very low Al concentration samples could be produced by Fe contamination since Fe atoms may play a role as a solute. Although only a small amount of iron contaminates in the sample, its effect for pure Zr or very low Al concentration samples could be significant. The deviations of lattice strain compared with the calculated data for $x_{Al} > 10$ samples can be

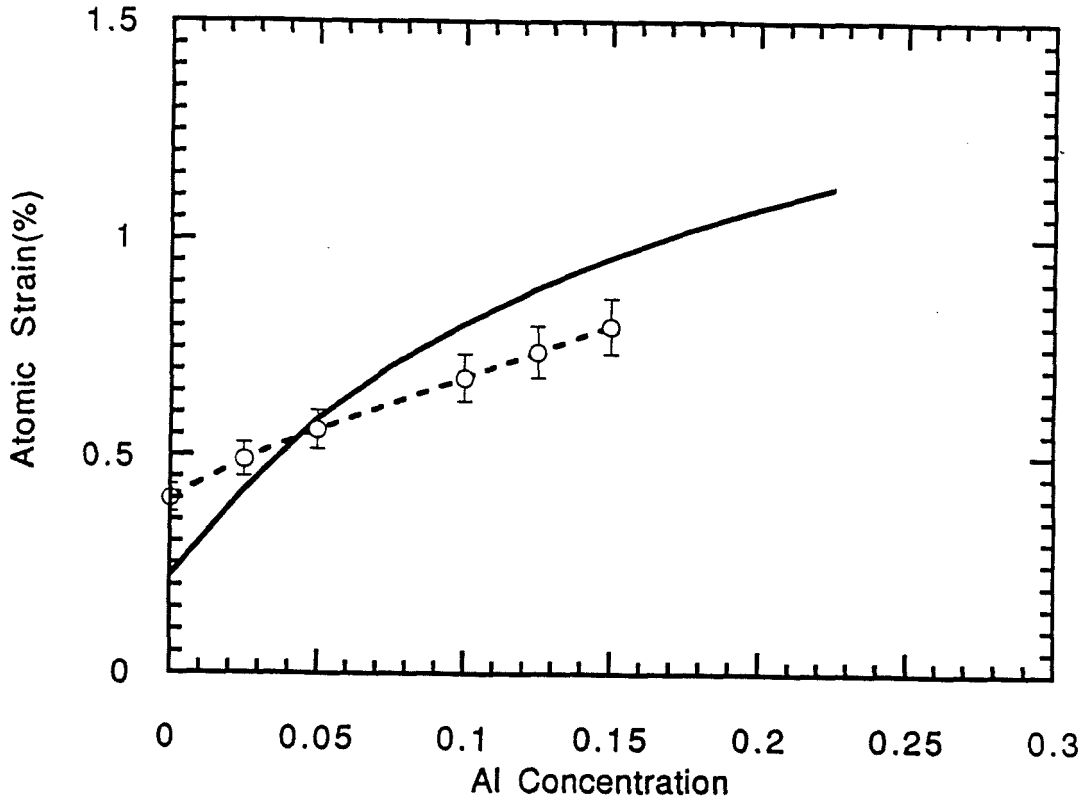

Fig. 3.14 Atomic strains of both the experimental data and the calculated data were plotted as functions of Al concentrations.

understood by the fact that there is a large fraction of grain boundaries in the ball milled nanometer-sized materials. Many defects like dislocations may be trapped at grain boundaries or form new grain boundaries so the atomic strains inside the crystalline grains are altered. Another possibility for having smaller strain in the samples within this composition range may be due to the existence of trace amount of amorphous phase so that the real solubility of Al is lower than the average composition.

3.4 Mechanical properties

In the last decade, there has been considerable interest in developing nanocrystalline materials. In such materials, the volume fraction of the grain boundaries becomes comparable to the volume fraction of the crystal grains. Small grain size or a larger fraction of grain boundaries has a stronger influence on the mechanical properties than in the case of traditional materials as observed in the Hall-Petch effect[17,18], Coble creep[19], and superplasticity [20]. The Hall-Petch relationship predicts a linear dependence of yield strength for conventional polycrystalline materials on the square root of reciprocal grain size, i.e., the strength or hardness should increase with decreasing grain size. In recent years, some investigations have been done on the mechanical properties of nanocrystalline metals and alloys [21-26] including the microhardness behavior of nanocrystalline materials as a function of grain size for comparing with the Hall-Petch relationship. In the study of the microhardness behavior of nanocrystalline Cu and Pd prepared by gas-condensation method, Chokshi *et al* [25] observed a negative Hall-Petch relationship for these materials, i.e., the hardness decreases as the nanocrystalline grain size decreases. It was suggested that, analogous to

Rosenhain's equicohesive temperature concept[27] which separates the low temperature regime where grain boundaries increase strength from the high temperature regime where grain boundary creep decreases strength (at a fixed grain size), the concept of "equicohesive" grain size may be introduced at a fixed temperature. That is, below the equicohesive grain size, grain boundaries were presumed to be strong, whereas above it, grain boundaries were presumed to be weak. Similar to this discovery, in studying the microhardness and the fracture properties of the nanocrystalline Ni-P alloy, Lu *et al.* [26] also claimed that the hardness of the nanophase material decreases with the reduction of grain size. They further found the hardness of the nanocrystalline alloy to be greater than that of the amorphous phase. In contract to Chokshi and Lu's results, Nieman *et al.* [28] have found that the microhardness of the nanocrystalline sample exceeds that of coarse-grained samples by a fact of 2 to 5 and the usual Hall-Petch behavior of increasing hardness with decreasing grain size holds, albeit with a smaller slope than for coarse grained samples. Restrictions on dislocation generation and mobility imposed by ultra-fine grain size were believed to be a dominant factor on increasing strength. They suspected that microhardness is strongly influenced by microstructural processing flaws that control the upper limit of measured hardness of the samples. This upper limit is determined by the point at which grain size becomes comparable to flaw size. More recently, consistent with the result of Nieman *et al.*, Jang *et al* [29] reported a Hall-Petch relationship in nanocrystalline iron produced by ball milling and found the hardness increases as the grain size decreases. Another interesting result is recently published by Y.-H. Kim *et al.* [30]. They claimed that Al-based amorphous

alloys containing 7 volume percent of 3 to 4 nm finely dispersed fcc-Al particles exhibit higher tensile strengths and hardness than those of amorphous single phase alloys with the same compositions. The purpose of the current measurements is to determine the hardness-grain size relationship in a nanometer-sized supersaturated solid solution and to understand the microhardness-microstructure relationship by comparing the hardness of solid solution, mixed two phase material, and single amorphous phase.

Hardness is a measure of a materials resistance to surface penetration by an indenter with a force applied to it. It is obvious that hardness is related to the flow strength of the material. As we know, the flow strength of crystalline solid is increased by restricting the ease of dislocation motion. Various types of "obstacles" either alone or in combination can be introduced into a crystalline material to produce such an effect. The most common obstacles are dislocations, internal boundaries (such as grain boundary, phase boundary), solute atoms, impurities, etc. The solution hardening effect is a simple example caused by solute atoms. I expected the nanocrystalline supersaturated α-Zr solid solution could have higher hardness than the equilibrium solid solution due to the higher dislocation and grain boundary densities and the extended solubility of Al solute. Vicker's microhardness measurements were performed by Miniload hardness tester on "as-compacted" and polished samples using a 100 g load on individual powder grains. About 8 measurements of each sample were collected to calculate the average values. The hardness data as the functions of Al concentration and grain size were exhibited in Fig. 3.15 and Fig. 3.16 respectively. In Fig. 3.15, the open circles represent the data for samples

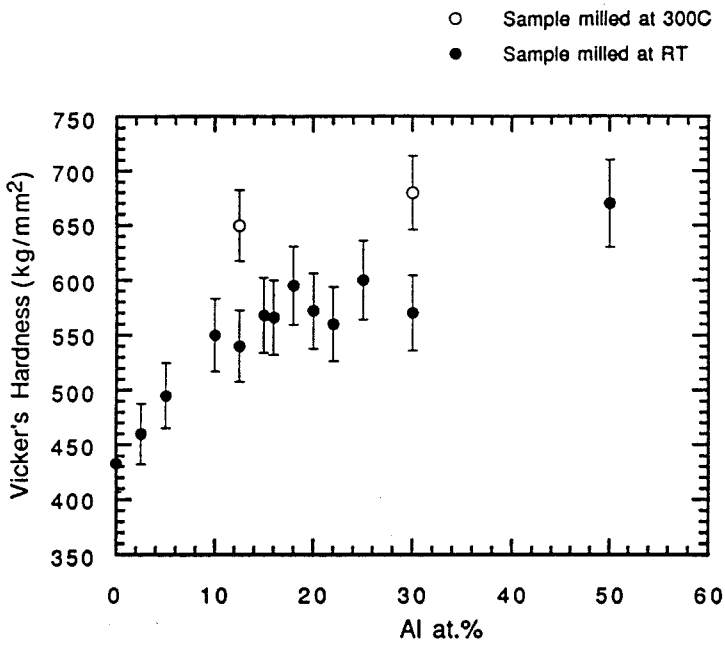

Fig. 3.15 Vicker's hardness as a function of Al concentration.

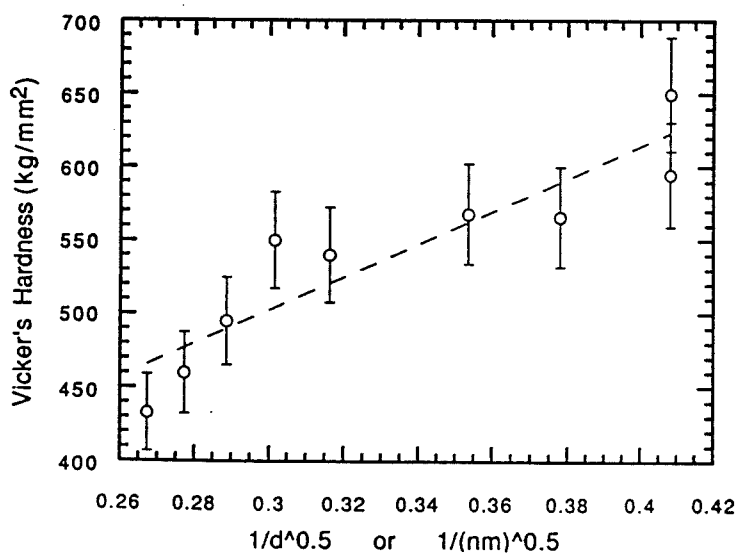

Fig. 3.16 Vicker's hardness was plotted as a function of grain size by following the Hall-Petch relationship.

milled at 300°C. The microhardness is higher for these samples than for those milled at room temperature for the same chemical compositions. From the high-resolution TEM analysis to be discussed in Chapter 5, the different hardness for samples milled at different ambient temperatures can be understood by their different microstructures. It was noticed that it is hard to determine the dependence of microhardness on nanocrystalline grain size quantitatively, partially because the changes in indentation diagonal length due to grain size-influenced hardness differences are of the same order of magnitude as uncertainties in the measurements. In addition, the absolute values of hardness could be underestimated as a result of the limited sizes of selected powder particles and the microstructural processing flaws. The qualitative analysis and discussion are summarized in the following:

1). The hardness was observed to increase with decreasing grain size. In general, the data can be explained following Hall-Petch relationship, but the slope of the fitting line has a much smaller value than that observed for more conventional coarser-grained polycrystalline sample [31]. This result is consistent with Nieman *et al.* [28] and Jang *et al.* [29]'s reports for nanophase materials.

2). For the same chemical compositions, the samples made by ball milling at 300°C have higher hardness due to their different microstrctures. For instance, we see crystalline grains dispersed in the amorphous matrix from HRTEM photo of $Zr_{70}Al_{30}$ by ball milling at 300°C. Our experimental data indicated that the "two-phase" samples have higher microhardness than the single phase specimens. This agrees with the result of Y.-H. Kim *et al.* [30]. The hardness of the amorphous phase in the Al-Zr system is greater

than that of nanophase materials. This is different from Lu's result for the Ni-P system. It is interesting to notice that the hardness of the $Al_{50}Zr_{50}$ amorphous phase has significantly higher value than that of amorphous $Zr_{70}Al_{30}$ at the same milling temperature. This does not seem to be simply due to the composition effect. The crystallization temperature of $Al_{50}Zr_{50}$ is also different from that of the amorphous materials with lower Al concentration (see Chapter 4). The data for amorphous $Al_{50}Zr_{50}$ suggested it is possible that there might be two different kinds of amorphous phases. More experiments are required to understand exactly the causes of the differences among these metastable materials.

References

[1] H. Fecht, G. Han, Z. Fu and W. L. Johnson, *J. Appl. Phys.* **67** (4) 1744 (1990).

[2] Z. Fu, H. Fecht and W. L. Johnson, *Proc. MRS spring meeting,* San Francisco, April, 1990.

[3] H. Fecht, E. Hellstern, Z. Fu and W. L. Johnson, *Metall. Trans. A* **21**(9), 2333 (1990).

[4] E. Hellstern, H.J. Fecht, Z. Fu and W.L. Johnson, *J. Appl. Phys.* **65** (1) 305 (1989).

[5] M. Oehring and R. Bormann, *Mater. Sci. and Engn.* **A134,** 1330 (1991).

[6] E. Hellstern, H. J. Fecht *et al., Mater. Res. Soc. Symp. Proc.* **132,** 137 (1989).

[7] K. Lu, J. T. Wang and W. D. Wei, *Scripta Metall. Mater.* **25,** 619, (1991).

[8] H.J. Fecht and W. L. Johnson, *Nature* 334, 50 (1988).

[9] En Ma and M. Atzmon *Phys. Rev. Lett.* **67** (9) 1126 (1991).

[10] P. Villars and L. D. Calvert, Pearson's Handbook of Crystallographic Data for Intermetallic Phases, 2nd ed. (ASTM International, Newbury, OH), (1991).

[11] L. E. Rehn, P. R. Okamoto *et al., Phys. Rev. Lett.,* **59,** 2987 (1987).

[12] J. Eckert, Y. R. Abe, Z. Fu, and W. L. Johnson, Chemical Processes in Inorganic Materials: Metal and Semiconductor Clusters and Colloids, ed. by J. S. Bradley, et al., Mater. Res. Soc. Symp. Proc. **272,** (1992) in press.

[13] J. Eckert, J. C. Holzer, C. E. Krill and W. L. Johnson, *J. Mater. Res.* **7,** 1980 (1992).

[14] Y. R. Abe, J. C. Holzer and W. L. Johnson, in Structure and Properties of Interfaces in Materials, ed. by W. A. T. Clark, C. L. Briant and U. Dahmen (Pittsburgh, PA) *Mater. Res. Soc. Proc.* **238,** (1992).

[15] J. Eckert, J. C. Holzer, C. E. Krill III, and W. L. Johnson, *J. Appl. Phys.* (Submitted.)

[16] S. Rabinovich, A. Voronel and L. Peretzman, *J. Phys. C: Solid State Phys.* **21**, 5943 (1988).

[17] E. O. Hall, *Proc. Phys. Soc.* (London) **B64**, 747 (1951).

[18] N. J. Petch, *J. Iron Steel Inst.* **174**, 25 (1953).

[19] R. L. Coble, *J. Appl. Phys.* **34**, 1679 (1963).

[20] O. D. Sherby, *et al.*, in Deformation Processing and Structure, ed. by G. Krauss, p. 355 (1982).

[21] R. Bohn *et al.*, *Scrpta Metallurgica* **25**, 811 (1991)

[22] Y. Fahmy, J. C. Russ and C. C. Koch, *J. Mater. Res.* **6**(9) 1856 (1991).

[23] M. J. Mayo, R. W. Siegel, *et al* , *J. Mater. Res.* **5**(5) 1073 (1990).

[24] G. W. Nieman, J. R. Weertman and R. W. Siegel, *J. Mater. Res.* **6**(5) 1012 (1991).

[25] A. H. Chokski, A. Rosen, J. Karch and H. Gleiter, *Scripta Metall.* **23**, 1679 (1989).

[26] K. Lu, W. D. Wei, and J. T. Wang, *Scripta Metall.* **24**, 2319 (1990).

[27] W. Rosenhain and D. Owen, *J. Inst. Metals* **10**, 119 (1913).

[28] G. W. Nieman, J. R. Weertman and R. W. Siegel, *Scripta Metallurgica* **23**, 2013 (1989).

[29] J. S. C. Jang and C. C. Koch, *Scripta Metallurgica* **24**, 1599 (1990).

[30] Y.-H. Kim, A. Inoue and T. Masumoto, *Mater. Trans.*, JIM **31** (8), 747 (1990).

[31] K. Farrell and B. T. M. Loh, JISI, 915 (1971).

Chapter 4

Thermal Stability Discussion

As we know from the previous chapter, there are two "*metastable phases*", i.e., nanocrystalline supersaturated solid solution and amorphous, formed by mechanical alloying of Al-Zr system. One of the crucial aspects of these materials is the stability against grain growth and crystallization. In the first part of this chapter, I would like to discuss the metastability of nanocrystalline materials based on the thermodynamics and grain boundary segregation arguments proposed by Johnson[1] as well as the related experimental concerns. Then, the experimental results by x-ray diffraction, DSC, and isothermal annealing will be given.

4.1 Can a nanocrystalline phase be a truly metastable phase?

The definitions of truly metastable and false metastable (or called configurationally frozen) phases have been given in the introduction chapter. To be a thermodynamic metastable state, the Gibbs free energy of a phase must be at a minimum and the state must be stable against fluctuations. In other words, there must be an energy barrier for the metastable phase to transform to any other phase. From common sense, the Gibbs free energy of a polycrystalline phase is usually higher than that of an interface-free single crystal of the same phase due to the existence of grain boundaries. Hence, poly- or nano-crystalline solids should be unstable against grain growth when the atoms become mobile. Unlike the crystallization of an amorphous phase, which usually has a nucleation

barrier, normal grain growth has no energy barrier, so it is easy to understand nanometer-sized materials as simply a configurationally frozen state. Indeed, systems such as nanocrystalline pure metals perhaps can not be truly thermodynamic metastable phases since the grain boundary energies in these systems will always be positive quantities (excess interfacial energies). Obviously, the stability of nanophase materials is directly related to the features of grain boundaries. The question is whether it is possible that nanostructured materials become thermodynamically metastable due to chemical influences which lead to varying grain boundary energy for binary or multi-component systems. Essentially, the grain boundary energy can be described by the following two terms according to the physical meanings[2]:

$$\sigma = \sigma^{o} + \sigma^{s} \quad ,$$

where σ is the total interface energy, σ^{o} and σ^{s} are the energy related to chemical binding and interfacial stress respectively. Grain boundary segregation occurs by a segregant atom diffusing through the lattice until it encounters a grain boundary, where it becomes trapped. As more and more of the segregating atoms accumulate at a grain boundary, the composition of the boundary significantly changes from that of the bulk. Equilibrium solute segregation at grain boundaries is often described by the Gibbs adsorption equation. Gibbs adsorption reduces the grain boundary energy σ by changing either the chemical binding (σ^{o}) or the surface stress (σ^{s}) or by reducing both. For instance, one may expect that a misfitted solute atom will concentrate in regions of the solid where strains can be relaxed such as at grain boundary, thereby lowering the total energy of the system. There are many publications concerning solute segregation at grain boundaries

and the reduction of grain boundary energy[3-6]. Most of the research, however, is limited to the studies of the thermodynamic equilibrium phases. Cahn and Hilliard's [7] assumption that σ is always positive has been widely accepted by intuitive considerations. While many scientists are interested in studying the synthesis, structure and properties of nanophase materials, few investigations concern the nature of the stability of nanocrystalline phase. On the basis of the fundamental equations of thermodynamic equilibrium and solute grain boundary segregation phenomena, Johnson proposed a novel idea to predict the stability of nanocrystalline alloys and argued the possibility of having zero or negative grain boundary energy. In the model, the grain boundary has been treated as another phase which competes with the crystalline solid solution phase under thermodynamic equilibrium conditions. As we know, there is a large fraction of atoms occuping the grain boundaries in nanophase materials due to the very small grain size. Gleiter and Birringer [8,9] have interpreted most of the special properties of nanocrystalline materials in terms of the special structure, i.e., there are two components in the microstructure of nanophases which are nearly perfect long-range ordered atomic arrangement in the grains and a more random grain boundary component. Therefore, it is reasonable to consider the grain boundary component as the second phase and to work out the total Gibbs free energy formalism as a function of thermodynamic variables of two phases including the grain boundary fraction which can be related to grain size by assuming a fixed boundary thickness for simplicity. Then, the amount of grain boundary in the system can be described by thermodynamic two-phase equilibrium. To satisfy the phase equilibrium condition, the system may have to adjust the

fraction of grain boundary in the system by following the level rule like the normal two-phase equilibrium case. Varying the fraction (or area) of grain boundaries in the system is equivalent to varying the grain size if the grain boundary thickness is fixed. Then, the total Gibbs free energy can be expressed as a function of grain size and if a minimum existed in the total Gibbs free energy curve for a particular grain size, a nanocrystalline phase with this specified grain size could become a truly metastable phase. With the same idea, Weissmüller [10] has recently calculated the Gibbs free energy of nanocrystalline alloy systems with large enthalpy of grain boundary segregation as a function of grain size and has found a minimum energy for a specified grain size (Fig. 4.1). He has also worked out the grain boundary energy at a fixed solute concentration as a function of grain size and found the grain boundary energy becomes zero and even negative for grain sizes larger than a certain value (Fig. 4.2). If the grain boundary energy σ assumes a negative value, there will be a negative driving force for grain growth and the crystalline grain size could shrink spontaneously. Therefore, this simple model predicts the existence of a truly metastable nanocrystalline material. Namely, there is a condition for binary alloys with the large enthalpies of segregation at which the nanocrystalline phases become thermodynamically stable against grain growth. Obviously, the idea itself is novel and very interesting. It will be even more important for both application and fundamental understanding of nanophase materials if the idea can be proven experimentally. To prove the existence of a truly metastable nanocrystalline phase, sufficient evidence would be to observe that the grain size changes reversibly with the corresponding experimental conditions. Another alternative type of evidence would be the direct

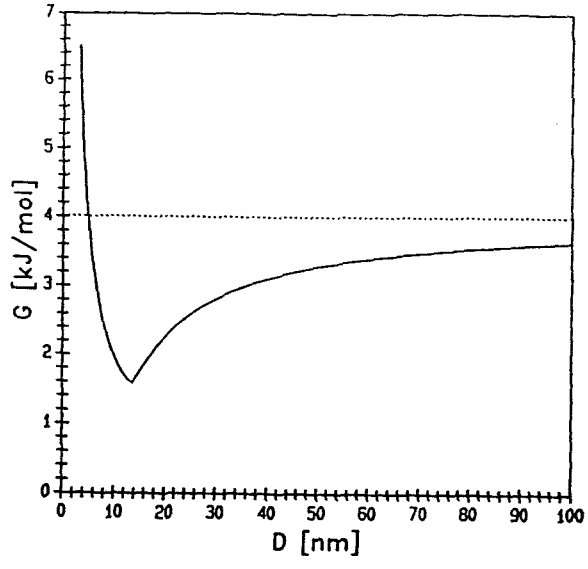

Fig. 4.1 The molar Gibbs free energy G of a binary alloy polycrystal as a function of grain size D at fixed pressure P, temperature T and solute molar fraction x_B=0.05. The dotted line denotes the Gibbs free energy of the solid solution single crystal with the same x_B.

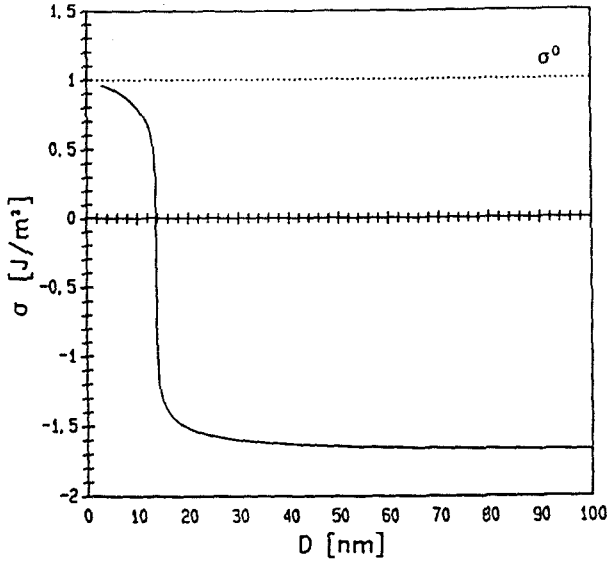

Fig. 4.2 The specific grain boundary energy σ as a function of grain size D at fixed P, T and x_B=0.05. The dotted line denotes the specific grain boundary energy σ^0.

measurement of the grain boundary energy. If the severe segregation reduces the boundary energy dramatically to approach zero or a negative value, the above idea will be proved. It is difficult from the experiment to obtain the excess energy contributed by metastable grain boundaries with the conventional techniques.

The model may be expected to describe some metallic binary or multi-component systems with a large tendency for solute grain boundary segregation such as Co-Zr, Al-Zr, Ni-Zr, Ni-B, etc. Essentially, the system should have a negative heat of mixing for the grain boundary phase. Meanwhile, the system should also have a positive heat of formation for the crystalline solid solution phase due to, for example, the mismatch of atomic sizes between the solute and the solvent (or the chemical disordering energy) so that the equilibrium solubility of the solute in the crystalline solid solution is low. The energy of a solute atom at a grain boundary could be much less than in the solid solution lattice. Hence, the total Gibbs free energy of the system could be minimized by creating more grain boundary phase in order to be in the thermodynamic equilibrium for a fixed solute concentration. Many experiments [11,12] so far have been tried to investigate the possible metastability of nanocrystalline phases. These include the Al-Zr mechanical alloying system. The efforts are focused on studying the grain size behavior at elevated temperature and evaluating if the grain size changes reversibly by varying temperature reversibly. No direct evidence for the presence of a metastable grain size has yet been observed. The main problem which I had in studies of the Al-Zr, Fe-B and Ni-B systems is how to prevent the formation of the stable intermetallic compound phases. Apparently, it is very difficult to observe the movement

of grain boundaries and to simultaneously suppress the formation of thermodynamic equilibrium phases. The model above considers only the competition between the solid solution and the grain boundary phase so the grain size becomes metastable only with respect to the equilibrium distribution of solute between the boundary and the solid solution phases. In the real systems such as Al-Zr, Fe-B and Ni-B, there are several intermetallic compound phases existing at different compositions. When severe segregation occurs, the solute precipitates as a pure phase or some equilibrium compound phase often forms along the grain boundaries. The metastable behavior of a nanocrystalline phase is then obscured. There is usually a large driving force for the formation of stable phases. To observe the metastable nanophase materials, it is necessary for the experimental temperature to be high enough so the system can be in chemical equilibrium between the boundary and solid solution. Furthermore, temperature must be high enough for grain boundaries to migrate and achieve an equilibrium configuration. In other words, a relatively high temperature is required for the atomic movement in the nanophase materials to be sufficient to observe a metastable grain size. If the annealing temperature is low, it will take months or years to be able to obtain the metastable equilibrium grain sizes. According to this estimate, the experiments are likely impossible in practice. On the other hand, the temperature has to be low enough to suppress the formation of stable equilibrium phases. Therefore, there is perhaps only a narrow temperature window where the nanophase could become metastable. Within such a narrow temperature window, the change of average grain size may be expected to be about one order of magnitude smaller than the nanophase

grain size. In fact, Birringer [9] has estimated the change of grain size with this model by assuming a fixed grain boundary thickness and found that changes of only 1 to 2 nm in the average grain size are expected if the temperature change $\Delta T=200^{o}C$. 1 to 2 nm is usually in the same order as the error of the x-ray measured average grain size. Moreover, if the temperature window is smaller than $200^{o}C$, the effect could be even smaller. Therefore, more sensitive or accurate experimental techniques are required for this study. Developing a more accurate experimental method may improve the experiments. Another alternative way is to study a more sensitive parameter. For instance, instead of measuring the average grain size, a grain size distribution curve may be determined to see if there is any reversible behavior in the shape of the grain size distribution function under varying the experimental conditions.

There are other reasons for the difficulty of observing metastable nanophase materials. 1) As we know, these binary systems are often considered as good candidates for solid-state amorphization. If there is no constraint on the thickness of a grain boundary, i.e., the changing of the grain boundary fraction in the system can simply lead to the grain boundaries growing thicker and thicker. The system may become a complete amorphous phase. 2) The model itself contains certain assumptions. For example, the grain boundary is treated as a normal phase, so the grain boundary energy should depend only on the normal thermodynamic variables such as temperature, pressure and so on. In the real system, however, it is often found that the boundary energy is misorientation, structure, and curvature dependent. A system with the same chemical composition and the same grain size may have different

total energy due to the different structures in the boundaries. There are some reports [13] suggesting that it is difficult to estimate a strict thermodynamic parameter for the grain boundary segregation enthalpy because of the various kinds of the segregation sites. Because it is difficult to estimate the exact volume or the exact thickness of a segregated layer, or complexity of atomic structure on grain boundaries, the evaluation of an exact concentration of the segregant at grain boundaries is also difficult. In the study of thermodynamic and structural properties of the [001] twist boundary of Au, the grain boundary energy was found to be misorientation dependent [14]. Other studies indicated grain boundary energy varies with the different boundary configurations [13,15] which are not uniquely determined by grain size. Therefore, only the systems which can be described under the model's assumptions may offer a chance for experiments to detect reversible grain size changes.

There is experimental evidence for seeing a shrinkage of average grain size when the temperature is increased. By studying the grain size dependence of coercivity and permeability in nanocrystalline ferromagnets, Herzer [16] found there is a grain size decrease by increasing annealing temperature. It is not clear, however, that grain size changes reversibly when the annealing temperature is changed back to the lower temperature. A nanocrystalline ribbon sample of $Fe_{74.5-x}Cu_xNb_3Si_{13.5}B_9$ was prepared by rapidly quenching from the melt. There is the plot of coercivity as a function of annealing temperature and the coercivity as a function of grain size shown in the paper. From the experimental grain size and annealing temperature, one can find that the average grain size of $Fe_{74.5-x}Cu_xNb_3Si_{13.5}B_9$ materials is 25 nm by thermal annealing at 530°C. The

average grain size of 40 nm was obtained by annealing at 550°C, but when the material was heated to 600°C and annealed at 600°C for 1hr., the grain size is reduced to 25 nm. It would be very interesting to do experiments on this system to see if the grain size can change reversibly by the cycling change of temperatures.

Generally speaking, the systems with strong tendency for grain boundary segregation can be chosen for the experimental studies. Namely, the system must have a big difference in heat of mixing between the bulk and the boundary and a big difference in excess partial entropies of mixing between the bulk and the boundary. These two factors change the total free energy by influencing the interatomic bonding and the distribution of atoms so it may be possible to obtain a material with a truly metastable grain size. However, it is really a challenge to pick up a "*right*" system and figure out the "*right*" experimental conditions so the metastable nanophase can be observed experimentally.

4.2 Stability of nanocrystalline supersaturated solid solution

Besides the nature of thermal stability of nano-structured materials discussed in the previous section, the normal grain growth temperature for nanocrystalline materials is important for the practical applications. For instance, the thermal stability of mechanically alloyed powders with nanometer-sized grains is of critical importance since powder consolidation methods invariably require high temperatures. DSC combing with the x-ray diffraction and the thermal annealing experiments have been used to study the thermal stability of nanocrystalline supersaturated α-Zr solid solution. The experiments found that the samples after mechanical alloying must subject to a recovery or relaxation behavior upon thermal annealing due to

a big amount of defects created in the materials by heavy deformation. It was noticed from the DSC temperature scanning curves that the recovery or relaxation process usually started about 100°C for samples after ball milling which indicated that the temperature does not exceed 100°C during mechanical milling. During recovery, the density of crystal defects and their distributions change. When the temperature is high enough, the grain boundary moves and the grain growth occurs. Fig. 4.3a and Fig. 4.3b show the average grain size and the atomic strain of nanocrystalline $Zr_{87.5}Al_{12.5}$ solid solution as a function of annealing temperature respectively. In the experiments, the as-milled powders were annealed isothermally at each temperature for 24 hr. and then the x-ray diffraction patterns were taken for analyzing the average grain size. The analysis method for average grain size was described in Chapter 2. The experiments show that there is no change in the x-ray diffraction peaks at temperatures below 300°C. This includes annealing for 10 days at 300°C. The average grain size by annealing at 400°C is 1 to 2 nm larger than that of as-milled powders, but no significant grain growth observed. This small change could be possibly caused by some types of recovery and relaxation. When the annealing temperature is higher than 420°C, the crystal grains of α-Zr solid solution phase grow rapidly. This behavior of average grain size upon heat treatment appears to be rather typical for nanophase oxides [17,18], nanophase metals [19], and alloys [20]. For example, a similar result was obtained by Lu *et al.*[20] for nanocrystalline Ni-P alloys prepared by crystallization from amorphous phase. The temperature they found for significant grain growth is about 50°C lower than the Al-Zr system. Fig. 4.4 shows the x-ray diffraction results of $Zr_{87.5}Al_{12.5}$ samples obtained under different experimental conditions. The

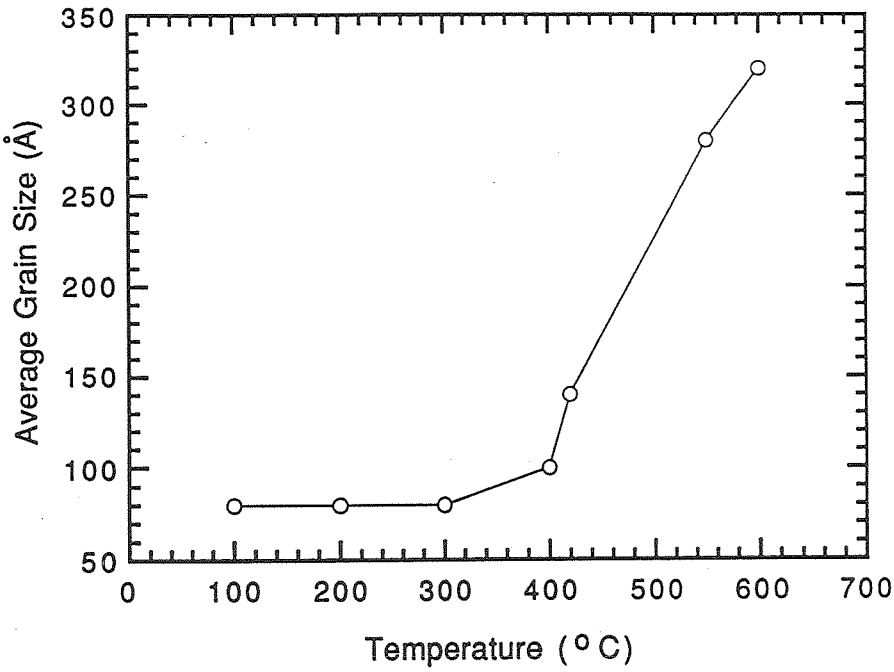

Fig. 4.3a The grain size changes at different annealing temperature for nanocrystalline $Zr_{87.5}Al_{12.5}$ sample.

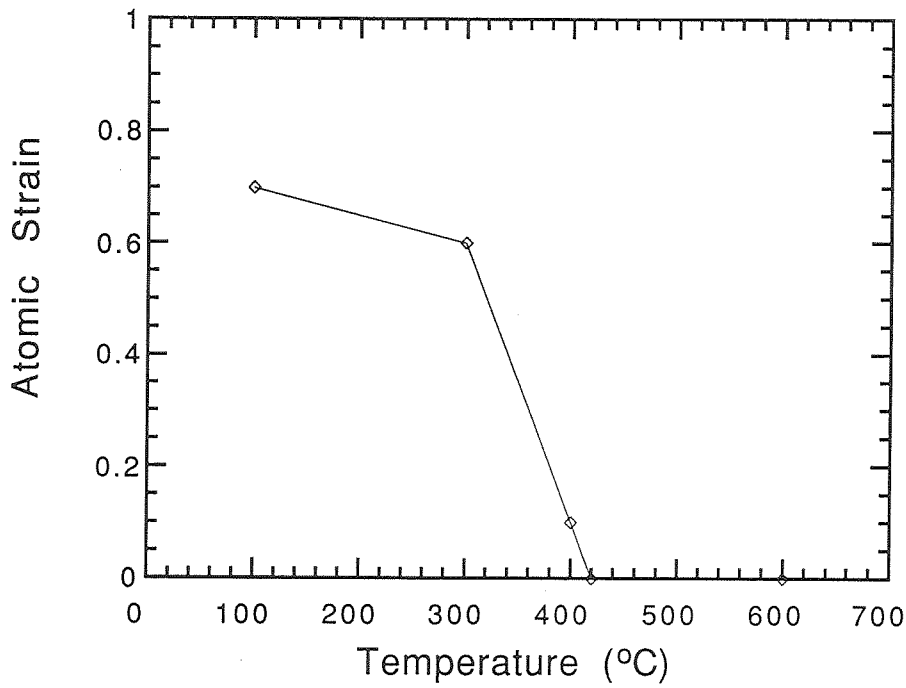

Fig. 4.3b The atomic strain changes at different annealing temperature for nanocrystalline $Zr_{87.5}Al_{12.5}$ sample.

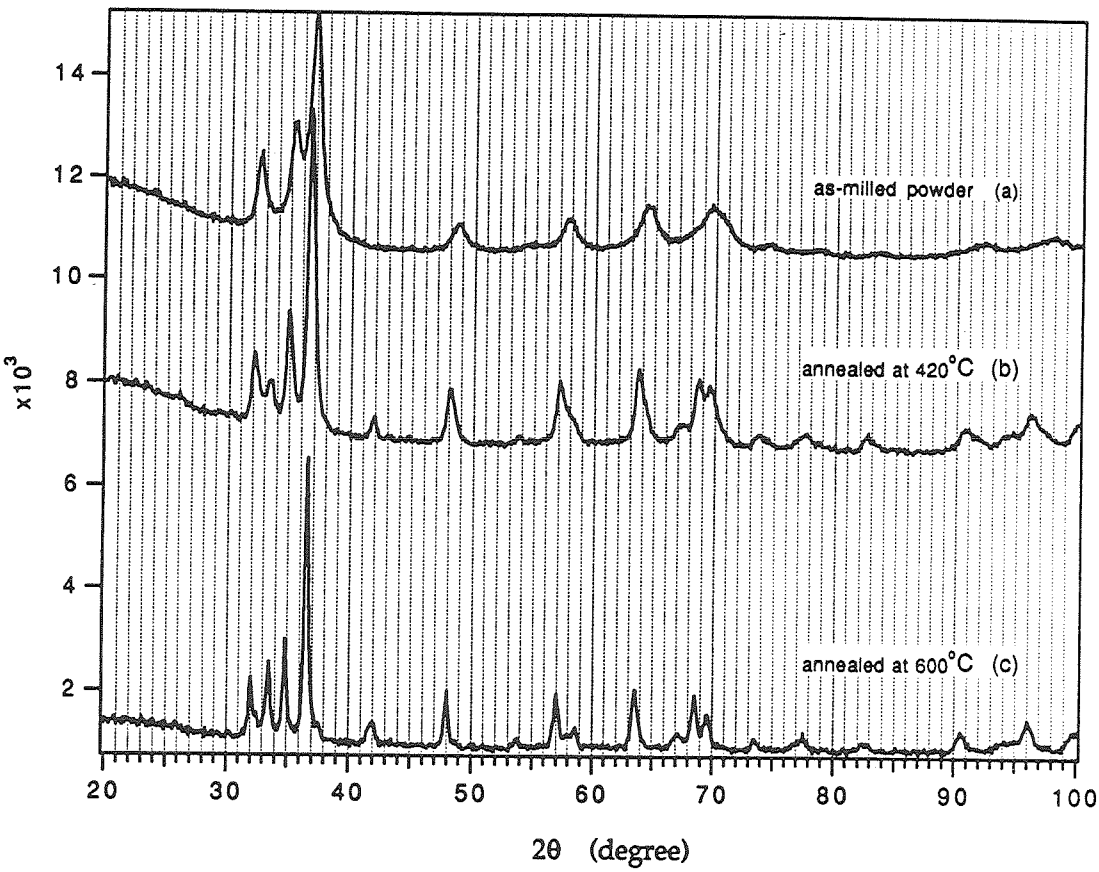

Fig. 4.4 The x-ray diffraction curves for nanocrystalline $Zr_{87.5}Al_{12.5}$ sample after different heat treatments as indicated below: a) as-milled sample; b) annealed at 420°C; c) annealed at 600°C.

structure of the as-milled powder is shown in Fig. 4.4(a). Only a single hcp α-Zr phase is observed. The extra Bragg peaks in Fig. 4.4 (b) indicate the formation of the equilibrium compound Zr_3Al_2 phase after annealing at 420°C. The peak shift towards lower angles for the α-Zr phase is directly related to the decrease of Al solubility in the solid solution. There is an even further shift of Bragg peaks for α-Zr phase detected after annealing at 600°C. From x-ray analysis, an equilibrium solubility of Al in the α-Zr solid solution is obtained for the sample as shown in Fig. 4.4 (c). By combing the data in Fig. 4.3 and Fig. 4.4, it can be concluded that the grain size of nanocrystalline supersaturated solid solution is stable under heat treatment until reaching a temperature where the crystallization of an equilibrium compound phase occurs. On the basis of the above discussions, an interesting experiment could be tried to improve the thermal stability of nanophase materials by preventing the formation of the equilibrium compound phase. The grain size of nanocrystalline phase appears to be stable until this crystallization occurs. For instance, the mechanical alloying of a $Zr_{87.5}Al_{7.5}B_5$ sample has been tried to improve the stability of the nanophase material (compared with $Zr_{87.5}Al_{12.5}$ sample) since the formation of compound phase requires a certain Al concentration. Boron is usually a good segregant and should have little solubility in the Zr_2Al or Zr_3Al_2 compound phases. Thus an improved thermal stability could be expected. The same final x-ray diffractograms were obtained after MA of powders with $Zr_{87.5}Al_{7.5}B_5$ and $Zr_{87.5}Al_{12.5}$ compositions. In the DSC experiments, it turned out that there is only a ten degree improvement in the formation temperature of equilibrium compound by the addition of boron atoms. Since boron can not be easily detected in x-ray spectra, it is

hard to study in detail where the boron goes during the MA and in the final product. For the future research, it is interesting to study the improvement of the thermal stability of nanophase materials by attempting to suppress the formation of equilibrium phases in the system.

As we know, the rapid grain growth for the solid solution phase is observed only after the formation of the equilibrium compound. A pre-annealed sample in which the crystallization of the equilibrium compound has been detected is shown in Fig. 4.4 (b). This sample was used to run both isochronal and isothermal scans by DSC. The pure grain growth behavior can be obtained with this sample since the highest temperature for the DSC experiment is 600°C and no other reaction occurs (except grain growth) by annealing at temperatures T ≤ 600°C as shown in Fig. 4.4 (c). There is a broad exothermic peak found in the temperature scan curve that has a typical shape for grain growth. From the peak position of the normal DSC scan curve, the isothermal temperature can be determined. A typical exponential curve for grain growth was found in an isothermal DSC experiment. The data analysis for the isothermal scan was studied by following Chen and Spaepen [21]:

In an isothermal experiment, the DSC signal heat flow dH/dt can be expressed as:

$$-\frac{dH}{dt} = \frac{H_o r_o}{n} = \frac{K(T)}{[r_o^n + K(T)t]^{n+1/n}} \quad ,$$

where H_o and r_o are, respectively, the initial enthalpy and grain radius. $K(T)$ is the temperature dependence of the rate constant and can be written as: $K(T) = k_o \exp(-Q/k_B T)$. k_o is a pre-exponential constant and Q is the activation energy of the process which can be determined by the Kissinger analysis from the DSC experiments. T is temperature and k_B is the Boztman

constant. t is the experimental time and n is an exponent. H_o is a function of temperature only and can be obtained by integrating the total enthalpy from isothermal DSC curve at given temperature. r_o can be determined by the average grain size analysis using the x-ray results. In an isothermal experiment the evolution of the grain size is: $r^n(t) = r^n(0) + K(T)t$. The evolution of interfacial enthalpy can be written as:

$$H(t) = {H_o r_o}/{r(t)} = \frac{H_o r_o}{[r^n(0) + K(T)t]^{1/n}} \quad ,$$

then,
$$(\frac{H(t)}{H_o})^n = \frac{{r_o^n}/{K(T)}}{{r_o^n}/{K(T)} + t} = \frac{\tau}{t+\tau} \quad ,$$

where $\tau = {r_o^n}/{K(T)}$ and $H(t) = H_o + \int_0^t \frac{dH}{dt} dt$.

By plotting $\ln(t+\tau)$ vs. $\ln H(t)/H_o$ to get a best fit to a straight line (through choosing the variable τ), the exponent n can be determined by the slope of the straight line and n=1.8 is obtained. This result agrees well with the theoretical grain growth model n=2 [22,23,24]. The fitting curve and the experimental curve from DSC isothermal scan are plotted in Fig. 4.5.

By integrating the total enthalpy of the isothermal curve, the enthalpy contribution from the grain boundary energy can be estimated since the initial and final average grain sizes of α-Zr are known from the x-ray data analyses. The total enthalpy of integration is about 1.5 KJ/mole. The density can be estimated from the literature data for pure Zr and Al. It can be proven that the ratio of grain boundary area to the bulk crystal grain is proportional to α/d. Where α is the geometry factor which is determined by

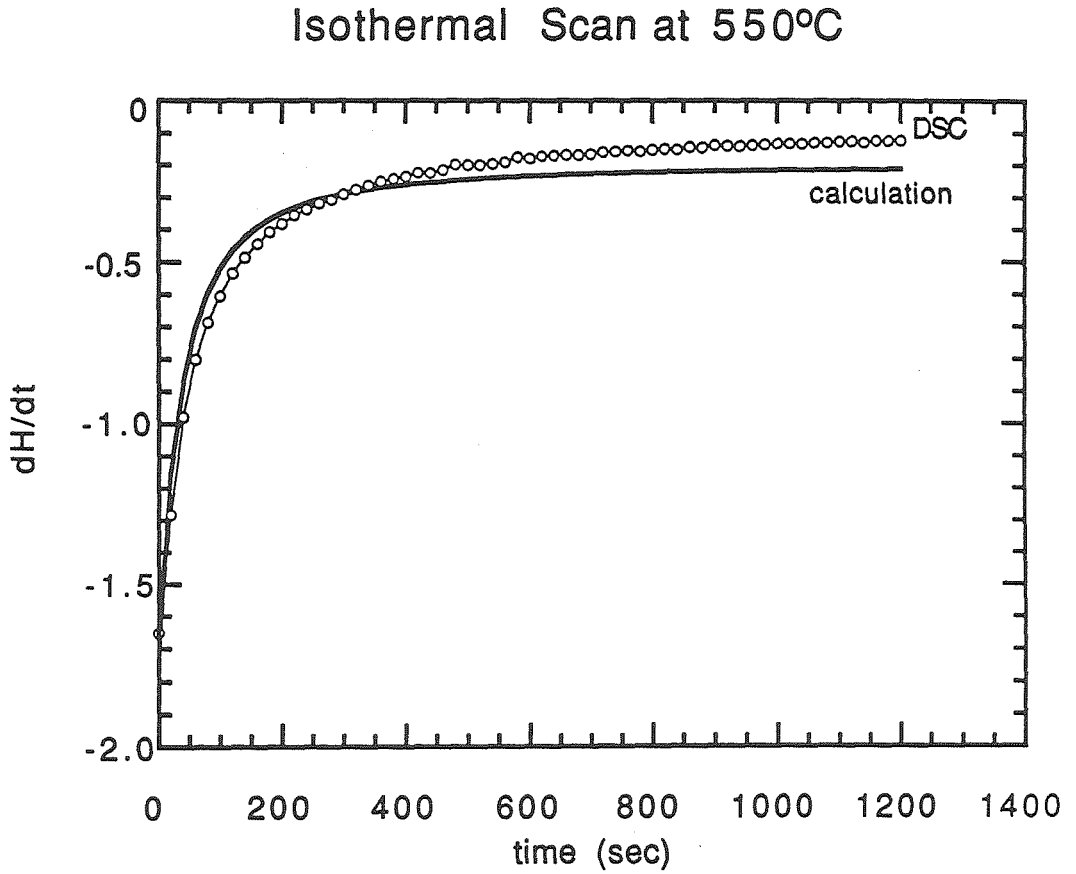

Fig. 4.5 The fitting curve and the experimental curve obtained by isothermal at 550°C in the DSC for the grain growth study.

the shape and size distribution of crystalline grains and d is the average grain size. Taking the average value of α=2.5 and assuming a nanophase α-Zr grain growth only, the specific grain boundary energy can be estimated to be about 675 erg/cm^2. This value corresponds to the grain boundary energy of the equilibrium solid solution after crystallization of the compound phase. The positive grain boundary energy provides a driving force for grain growth. For comparison, the grain boundary energy for nanocrystalline pure Zr [25] has been estimated by the same method. The value of the grain boundary energy for pure Zr turns out to be at least 1000 erg/cm^2·. Therefore, there is a significant decrease on the grain boundary energy for even the equilibrium solid solution It is expected the grain boundary energy will continue decreasing with increasing solute solubility, but it is impossible to measure the grain boundary energy for a highly supersaturated solid solution with this method. Hence, it is not clear if it is possible for the grain boundary energy to approach zero under the highly supersaturation condition.

Since the grain growth and crystallization of compound phases can be studied separately, it is possible to obtain the activation energy for both reactions with Kissinger analysis [26] and to compare with each other. Fig. 4.6 shows the plots of $\ln(S/T^2)$ vs. $(1/T)$ as obtained from DSC for both crystallization of equilibrium phase and the grain growth reactions. From the plots, we can see the two events almost occur together under the useful temperature range for the experiments. It is easy to understand why it is difficult to study only the grain growth without the formation of equilibrium phase. For proving the presence of a metastable nanocrystalline phase experimentally, an ideal system should have either a

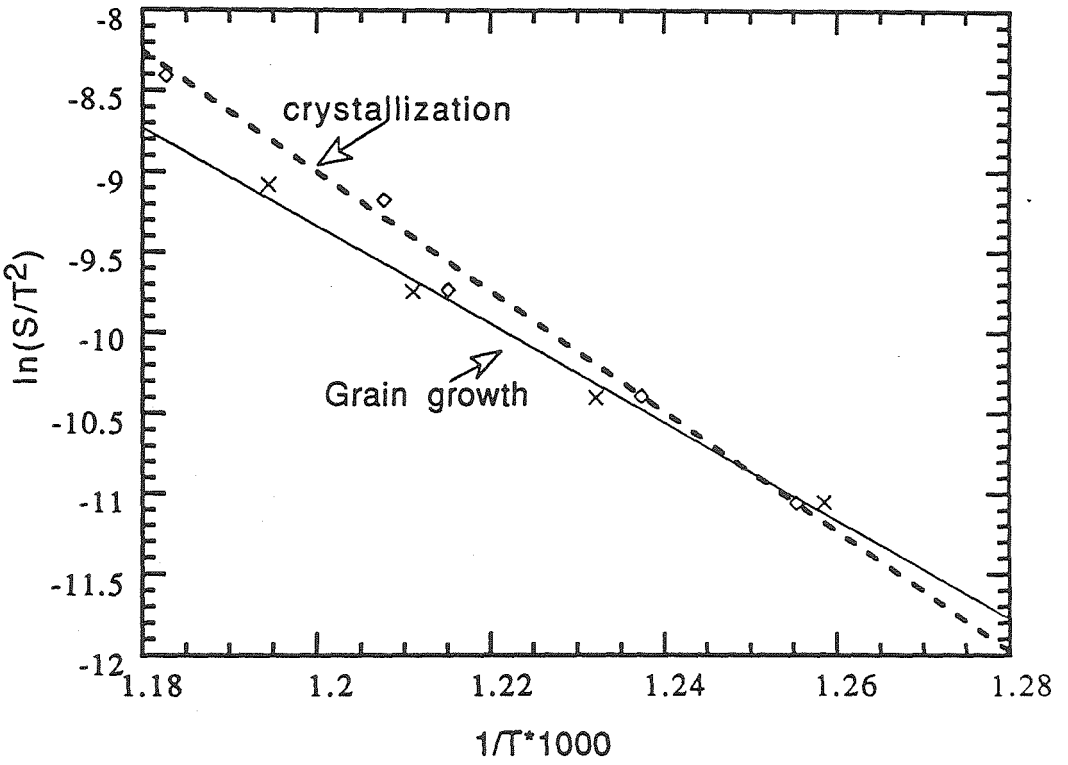

Fig. 4.6 The Arrenious plots for both the crystallization of equilibrium phase and the grain growth processes.

big slope difference of the two lines shown in Fig. 4.6 or the crossover temperature should be high enough so that solute atoms could reach chemical equilibrium or the two curves could be parallel but far from each other. Then grain growth would occur first at all the temperatures of experimental concern.

4.3 Stability of the amorphous materials

Fig. 4.7 [27] is a temperature time transition (TTT) diagram in which dashed line (a) represents a fast cooling illustration, (b) isothermal heat treatment of the glass giving crystallization at time t_x, and (c) slow heating of the glass producing crystallization at temperature T_x. T_m is the melting point, T_g is the glass transition temperature and T_x is the crystallization temperature. From the diagram, one can understand that the glass phase will transform to a crystalline phase after sufficient time by either heating up or isothermal annealing. Hence, the stability is related to time and temperature and is critically important for the glass applications. An essential and standard method to study the thermal stability of metallic glass is to measure the crystallization temperature by DSC. It is worth noting that the crystallization temperature T_x is not a unique temperature and depends on both the heating rate and the thermal history of the materials. Although the crystallization temperature T_x may not be taken as a "safe" operating temperature for applications of amorphous materials, the crystallization temperature obtained from DSC can provide a useful and quick means to qualitatively understand the thermal stability of an amorphous phase. This is especially true, for comparing the relative thermal stabilities of different materials. As an example, Fig. 4.8 shows the DSC temperature scan at heating rate of 20 K/min for $Zr_{50}Al_{50}$ ball-milled amorphous material. The

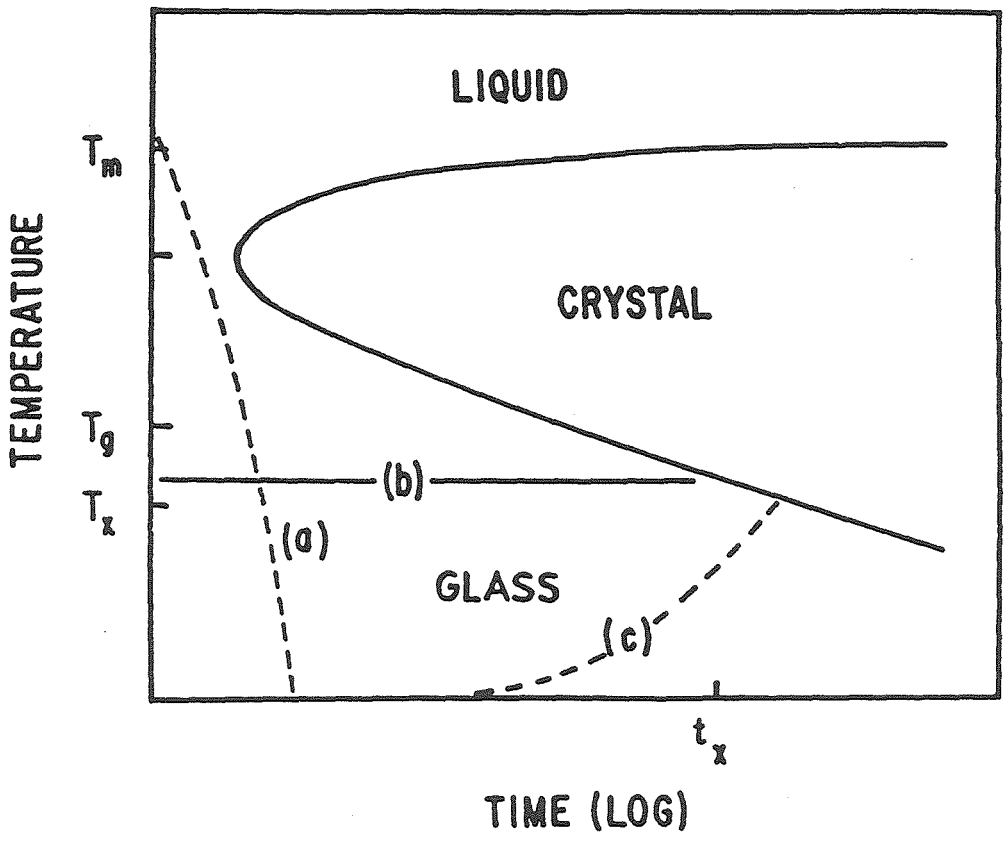

Fig. 4.7 TTT diagram representing a glass to crystal phase transformations by either heating treatment or isothermal annealing.

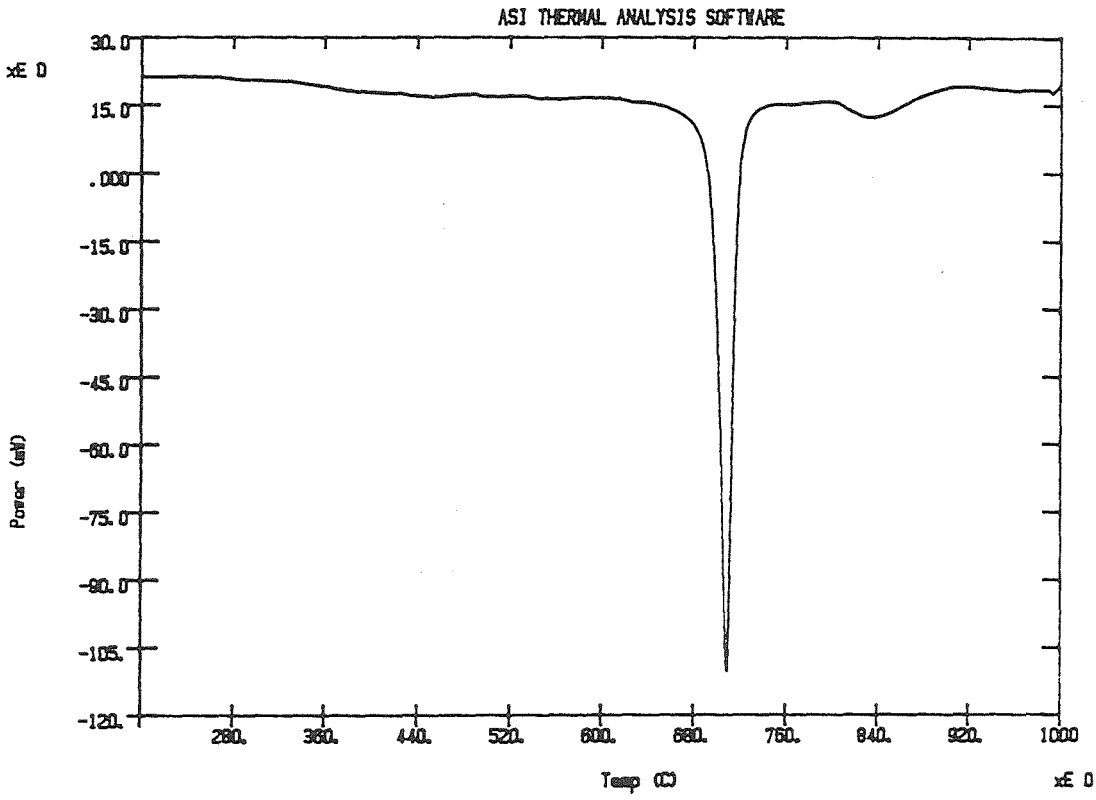

Fig. 4.8 The DSC curve for ZrAl amorphous sample at the heating rate of 20 K/min to show the typical behavior of crystallization.

experiment was carried out with the Sataram DSC 2000 equipment since the crystallization temperature of $Zr_{50}Al_{50}$ amorphous is higher than 600°C. The sharp exothermic peak in Fig. 4.8 is associated with the crystallization reaction of amorphous material. The crystallization temperature is found to be 710°C which is quite high compared with the amorphous materials of other compositions for the Al-Zr system. The crystallization temperature as a function of Al concentration is shown in Fig. 4.9. It should be noticed that the T_x for samples with $x_{Al} < 18at.\%$ could reflect the crystallization of compound from solid solution as well. The kinetics of this crystallization reaction can be examined by a Kissinger analysis [26]. The Arrhnenius plot for $Zr_{80}Al_{20}$ is shown in Fig. 4.10 as an example to show how the activation energy is determined. The activation energy obtained as a function of Al concentration was given in Fig. 4.11. The activation energies of crystallization for samples with different composition are almost a constant except for $Zr_{50}Al_{50}$ amorphous. The activation energy of the amorphous sample is as high as 3.84 ev. The activation energy of grain growth is lower than that of the crystallization reaction. It seems that the crystallization temperature T_x scales with the activation energy E_a. Apparently, the experiments reveal the different properties between amorphous $Zr_{50}Al_{50}$ and the amorphous materials with other composition. As shown in Chapter 3, the microhardness of $Zr_{50}Al_{50}$ amorphous is also away from the nearly constant value of other amorphous materials. The difference could be related to the fact that crystallization leads to different intermetallic phases. It is also possible that there are some intrinsic differences between two types of amorphous phases. To understand better the reasons for

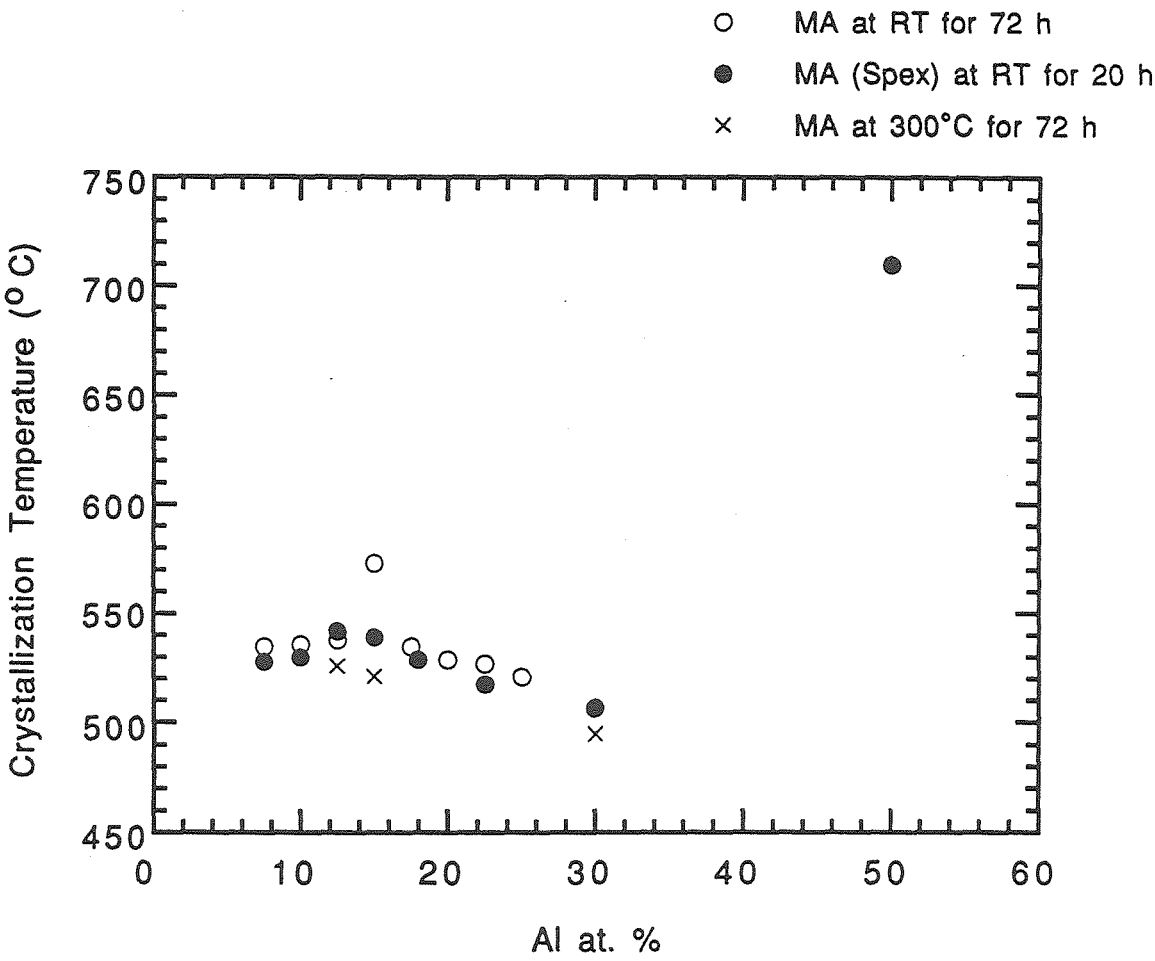

Fig. 4.9 The crystallization temperature as a function of Al concentration under different experimental conditions.

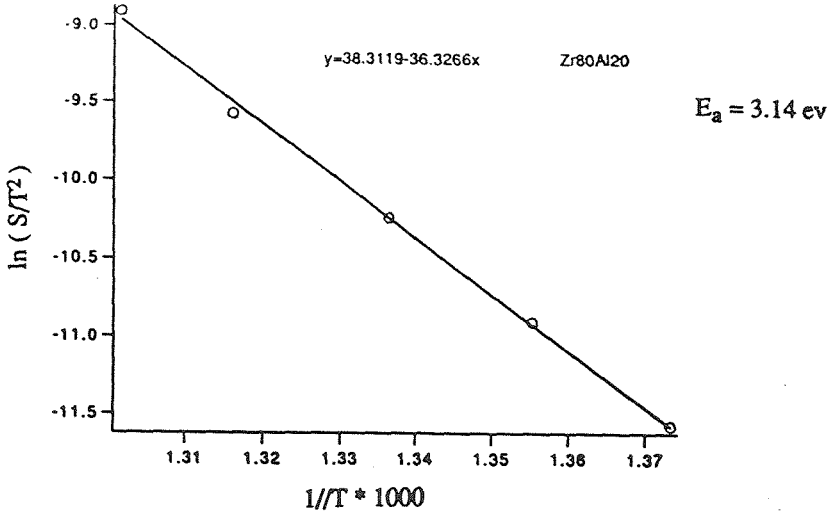

Fig. 4.10 A typical plot of ln (S/T^2) vs. $(1/T)$ as obtained from DSC for determining the activation energy.

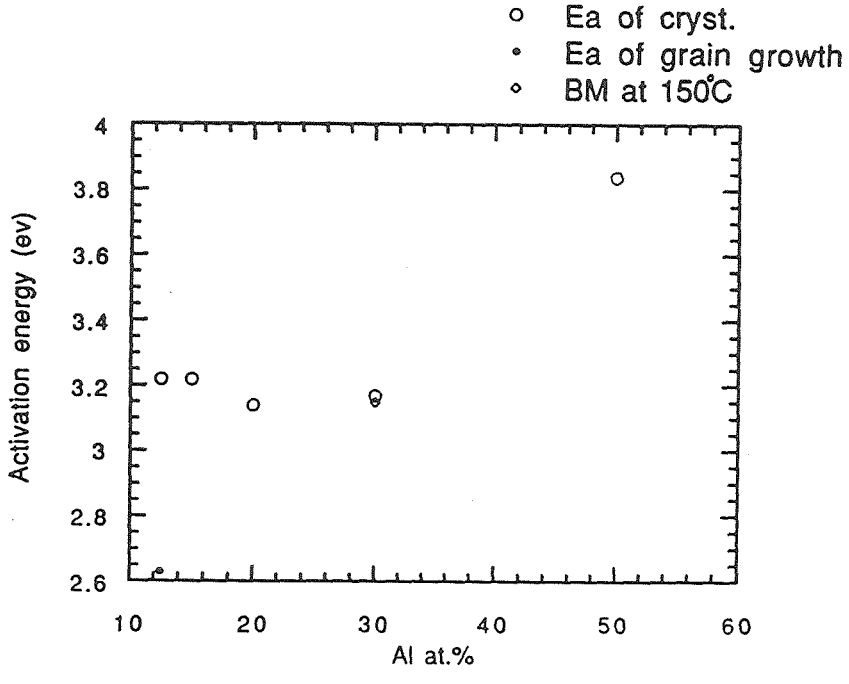

Fig. 4.11 Activation energies for both grain growth and crystallization reactions as a function of Al concentration.

having differences between $Zr_{50}Al_{50}$ amorphous and amorphous materials with lower Al concentrations, more investigations are necessary.

References

[1] W. L. Johnson, Group Meeting talk (March, 1991).

[2] J. W. Cahn and F. Larché, *Acta Metall.* **30**, 51 (1982).

[3] D. McLean, "Grain Boundaries in Metals," Oxford Univ. Press, Oxford, (1957).

[4] D. Gupta, *Metall. Trans. A*, **8A**, 1431 (1977).

[5] E. M. Fine, H. L. Marcus and J. P. Stark, *Scripta Metallurgica* **21**, 1571 (1987).

[6] K. L. Luthra and C. L. Briant, *Metall. Trans. A*, **19A**, 2091 (1988).

[7] J. W. Cahn and J. E. Hilliard, *Acta Metall.* **7**, 219 (1959).

[8] H. Gleiter, *J. Appl. Cryst.* **24**, 79 (1991).

[9] R. Birringer, *Mater. Sci. and Engn.* **A117**, 33 (1989).

[10] J. Weissmüller, Phys. Rev. B, Submitted.

[11] Y. R. Abe, J. C. Holzer and W. L. Johnson, in Structure and Properties of Interfaces in Materials, ed. by W. A. T. Clark, C. L. Briant and U. Dahmen (Pittsburgh, PA) *Mater. Res. Soc. Proc.* **238**, (1992).

[12] J. Eckert, J. C. Holzer, C. E. Krill III, and W. L. Johnson, *J. Appl. Phys.* (Submitted.)

J. Eckert, J. C. Holzer, C. E. Krill and W. L. Johnson, *J. Mater. Res.* **7**, 1980 (1992).

[13] S. Suzuki, *ISIJ International* **30** (11), 1000 (1990).

[14] R. Najafabadi and D. J. Srolovitz, *J. Mater. Res.* **6** (5), 999 (1991).

[15] C. L. Briant, *Acta Metall.* **31** (2), 257 (1983).

[16] G. Herzer, *IEEE Trans. on Magnetics* **26** (5), 1397 (1990).

[17] J. A. Eastman, Y. X. Liao, A. Narayanasamy and R. W. Siegel, *Mater. Res. Soc. Symp. Proc.* **155**, 255 (1989).

[18] R. W. Siegel, *Annu. Rev. Mater. Sci.* **21**, 559 (1991).

[19] E. Hort, Diploma Thesis, Univ. Saarlandes, Saarbrücken, Germany.

[20] K. Lu, W. D. Wei and J. T. Wang, *Scripta Metallurgica* **24**, 2319 (1990).

[21] L. C. Chen and F. Spaepen, *J. Appl. Phys.* **69** (2), 15 (1991).

[22] J. E. Burke and D. Turnbull, *Progr. Metal Phys.* **3**, 220 (1952).

[23] M. Hillert, *Acta Metall.* **13**, 227 (1965).

[24] C. Wagner, *Z. Elektrochem.* **65**, 581 (1961).

[25] H. J. Fecht, *et al., J. Adv. Powder Metall.* **1**, 11 (1989).

[26] H. E. Kissinger, *Anal. Chem.* **29**, 1702 (1957).

[27] M. G. Scott, Amorphous Metallic Alloys, ed. by F. E. Luborsky, (Butterworth & Co Ltd., London), p 144, (1983).

Chapter 5

Temperature Effects on Ball Milling

With the Super-MISUNI NEV-MA8 ball milling machine, mechanical alloying/milling (MA/MM) can be carried out at various ambient temperatures from room temperature to 300°C. The structure changes for samples after milling at different ambient temperatures are characterized by x-ray diffraction and transmission electron microscopy (including high-resolution TEM). The thermal stability behaviors of the samples milled at different temperatures upon heating have been studied by differential scanning calorimetry (DSC). In this chapter, I will first present the results obtained at different milling temperatures and then discuss the temperature effects for the milling process. There are several reasons of doing high temperature ball milling experiments here. 1) The most commonly accepted mechanism of amorphization by mechanical alloying is that the process results in the ultrafine layer structure in which a solid-state amorphizing reaction takes place [1-5]. Naturally, the temperature should be considered as one of the most important parameters in the solid-state reaction process. 2) The metastable stability of nanophase materials argued in the previous chapter is based on thermodynamics so that chemical equilibrium is a necessary condition in the related experimental studies. Obviously, ball milling at higher temperature could provide a better opportunity for the metastability investigations due to the enhancement of atomic diffusion at high temperatures. 3) The structural deformation induced by mechanical alloying is very important for driving a system out

of equilibrium state and certainly the recovery or relaxation behaviors of these structural defects are temperature dependent. 4) If the polymorphous transition mechanism of amorphization by MA at room temperature concluded by En Ma *et al.* [6] is correct and the same mechanism persists to the high temperature milling, the T_o line where the Gibbs free energies of liquid and crystalline phases are equal can be determined experimentally by finding the amorphization compositions at different temperatures.

As discussed in Chapter 3, depending on the composition of mixed powders by mechanical alloying at room temperature, two metastable structures are found in the Al-Zr system, namely nanocrystalline supersaturated α-Zr solid solution and amorphous phase. In the following three sections, taking pure Zr, $Zr_{87.5}Al_{12.5}$ and $Zr_{70}Al_{30}$ specimens as the examples of an equilibrium phase, supersaturated solid solution phase, and amorphous phase respectively, temperature effects on the microstructures and thermal stabilities have been studied for the samples with various compositions. The term high temperature that I use in this chapter is just related to room temperature not the conventional definition of "*high temperature*" for metals and alloys. Although the same milling times of 72 hours were used for all the experiments discussed in this chapter, the experiments revealed that a shorter time is sufficient for reaching a steady state when milling at higher temperatures. This is consistent with the solid state reaction process.

5.1 Stable equilibrium phase

The x-ray diffraction results of pure Zr ball-milled at room temperature and 300°C have been shown in Fig. 5.1. By analyzing the broadening of the

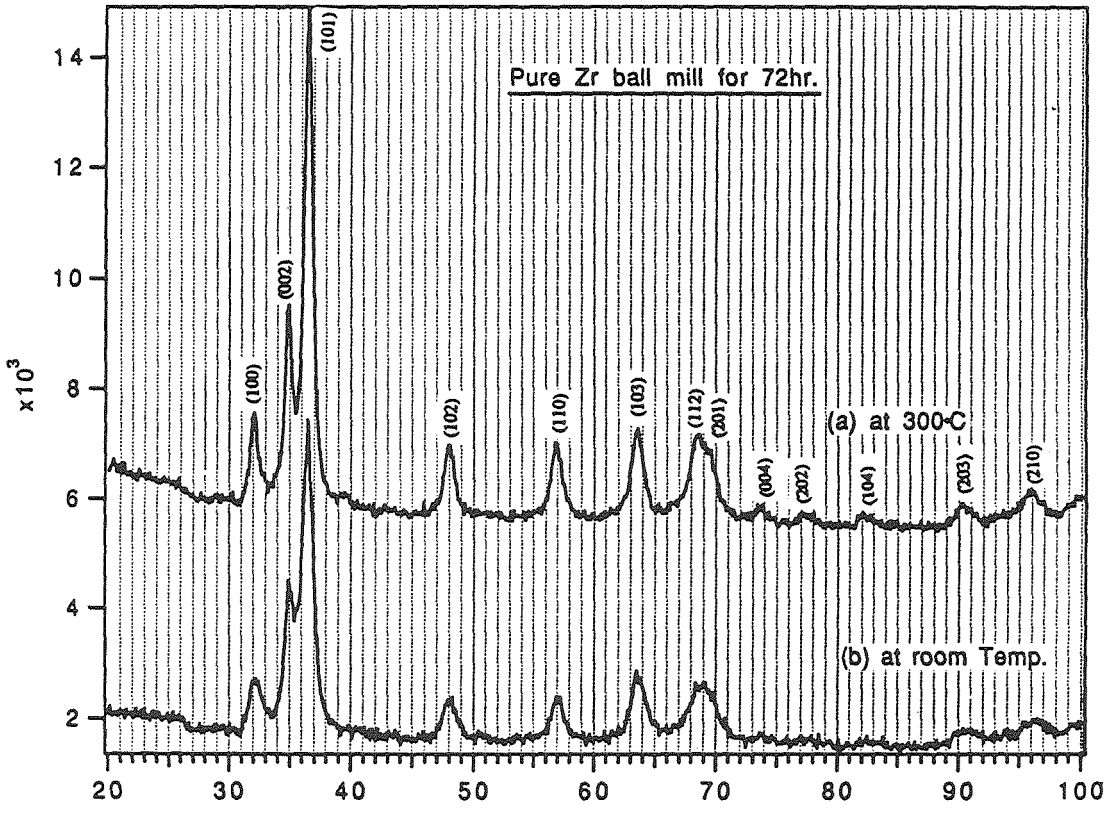

Fig. 5.1 X-ray diffraction results for pure Zr powders after ball milling at room temperature and 300°C.

Bragg peaks with the method described in Chapter 2, the grain size and atomic strain can be obtained (see TABLE I). The experimental results indicated an average grain size of 16 nm and the atomic strain of 0.3 % for Zr milled at 300°C, while the average grain size of 14 nm and the atomic strain of 0.4 % for Zr milled at room temperature. For pure elemental powders, the microstructure of the sample after ball milling process is determined by the plastic deformation and accompanying defects introduced during mechanical attrition. These include point defects, dislocations and grain boundaries, and the recovery behavior of the studied material, i.e., the densities of structural defects produced by ball milling. Because of the enhanced recovery and relaxation at higher temperature, the densities of structural defects, especially the saturation of dislocation density, will decrease with increasing milling temperature. Therefore, a larger grain size and smaller lattice strain were observed for pure Zr powder ball milled at 300°C compared with those ball milled at room temperature. Similar temperature effects on mechanical alloying of α-Zr solid solution with the solubility of aluminum $x_{Al} \leq 2$ *at.%* are expected since this is a thermodynamic equilibrium phase like pure Zr.

5.2 Supersaturated nanocrystalline solid solution

According to the phase diagram, the equilibrium solubility of aluminum in α-Zr is only about 2 at.% at temperature below 500°C. The mechanical alloying process results in a significant increase of the solubility of aluminum in the α-Zr solid solution. The amount of supersaturation can be estimated by comparing the experimentally determined lattice parameters with those predicted by Vegard's law. Fig. 5.2 shows the x-ray scans of supersaturated solid solution with composition $Zr_{87.5}Al_{12.5}$ after

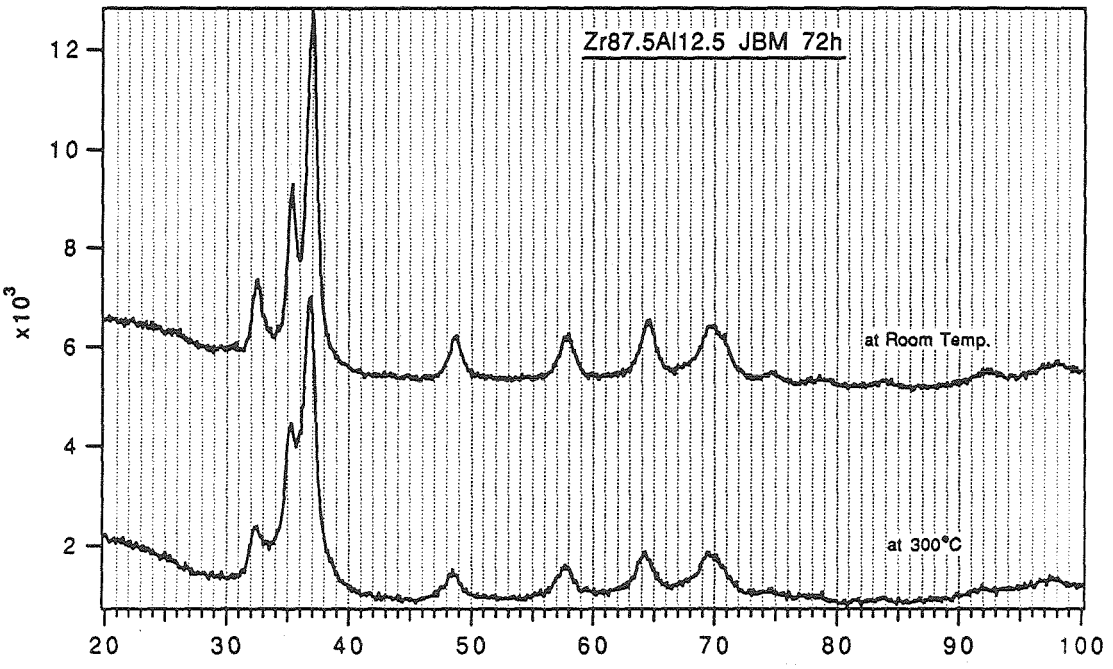

Fig. 5.2 X-ray diffraction results for $Zr_{87.5}Al_{12.5}$ samples after ball milling at room temperature and 300°C.

mechanical alloying at room temperature and 300°C respectively. We can see qualitatively from the scans that the Bragg peaks for the sample milled at 300°C shift to low angle side compared with those for the sample milled at room temperature. This corresponds to a larger lattice parameter or less aluminum solubility. The quantitative analyses of both samples for lattice parameter, grain size, and atomic strain, are listed in TABLE I. From the lattice parameter data, it was estimated that there is about 8 at.% Al in the crystalline grains for the sample milled at 300°C, although the average Al concentration within the whole sample is 12.5 at.%. The average microcrystalline grain size is about 6 nm and the internal atomic strain is about 0.2%. Hence, $Zr_{87.5}Al_{12.5}$ sample after milling at 300°C has less Al concentration in the crystalline grains and smaller grain size as well as less atomic strain by comparison to the sample ball milled at room temperature, although the two vials were filled with the same overall nominal composition each time for the experiment. The lower aluminum concentration found in the crystalline grains indicates chemical inhomogeneity of the sample. It is hard to distinguish where the extra aluminum really is since there are at least two possibilities: at the grain boundaries as solute segregant, or in an amorphous phase with higher Al concentration. No matter which situation is the case, certainly, the inhomogenity of chemical composition rules out the possibility of a polymorphous transition for amorphization by mechanical alloying at 300°C. This demonstrates that at least when the system was subjected to mechanical alloying at 300°C, the Al-Zr system does not amorphize by a polymorphous transition as Ma *et al.* (EM) concluded by mechanical alloying at room temperature. The grain size difference between two

TABLE I. Analytical Results of X-ray Diffraction Experiments

Sample	Lattice Parameter a (Å)	Lattice Parameter c (Å)	Grain Size (Å)	Atomic Strain (%)	X°_{Al}
$Zr_{87.5}Al_{12.5}$ (RT)	3.1918±.0004	5.0940±.0003	100±15	0.6±.02	12.5
$Zr_{87.5}Al_{12.5}$ (300°C)	3.1982±.0003	5.1013±.0003	60±20	0.2±.03	8.0
Pure Zr (RT)	3.2314±.0004	5.1367±.0003	140±10	0.4±.02	
Pure Zr (300°C)	3.2329±.0004	5.1388±.0004	160±15	0.3±.01	

Note: a). X°_{Al} is calculated value by assuming an ideal solution model and fitting the measured lattice parameters. b) The deviation of lattice parameters after ball milling for pure Zr samples must be caused by either iron contamination or the experimental error.

samples may be interpreted in terms of the different chemical homogenities of the samples. If the chemical inhomogeneity is caused by the equilibrium solute segregation at grain boundaries (due to the enhancement of atomic diffusion by milling at high temperature), then the grain boundary energy will be reduced compared with that obtained by milling at room temperature. As a consequence of lower grain boundary energy, we may expect more grain boundaries to exist in this sample than that milled at room temperature. Therefore, the smaller grain size is obtained for the sample milled at 300°C. If the boundaries are thick enough and can be viewed as an amorphous phase, then there are two phases coexisting in the sample. A metastable equilibrium is then predicted by the common tangent rule in the Gibbs free energy diagram. Thus, the amount of amorphous phase would be determined by the equilibrium condition, i.e., following the level rule. The grain size could be controlled by the amount of amorphous phase and the microstructure as we observed in the high resolution TEM images. The HRTEM pictures of $Zr_{87.5}Al_{12.5}$ milled at 300°C and room temperature are shown in Fig. 5.3 and Fig. 5.4 respectively. Different microstructures are seen in the HRTEM images. These are due to the differences in chemical homogenity of the samples. In Fig. 5.3, a thin amorphous layer (about 1.5 to 2.5 nm) is found to be uniformly distributed along the boundaries of crystalline grains. The thickness of this amorphous interlayer exceeds the reported estimates of grain boundary thicknesses of nanophase metals [7] made by cluster-assembled method. In contrast to Fig. 5.3, a uniform mixture of amorphous area and nanocrystalline area is observed in Fig. 5.4. The HRTEM results showed the presence of amorphous areas in the $Zr_{87.5}Al_{12.5}$ sample after MA at room temperature.

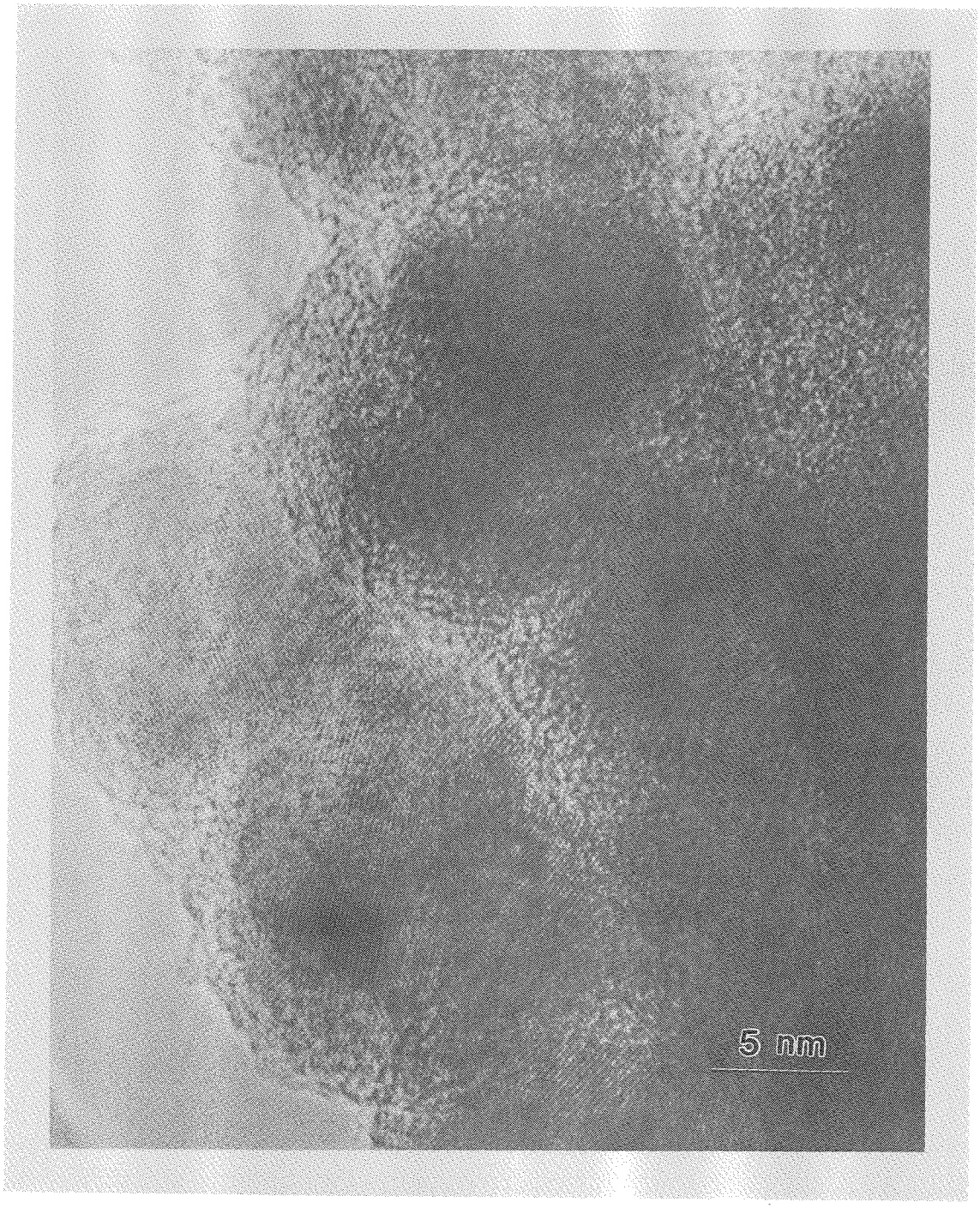

Fig. 5.3 High-resolution TEM image of $Zr_{87.5}Al_{12.5}$ sample by MA at 300°C.

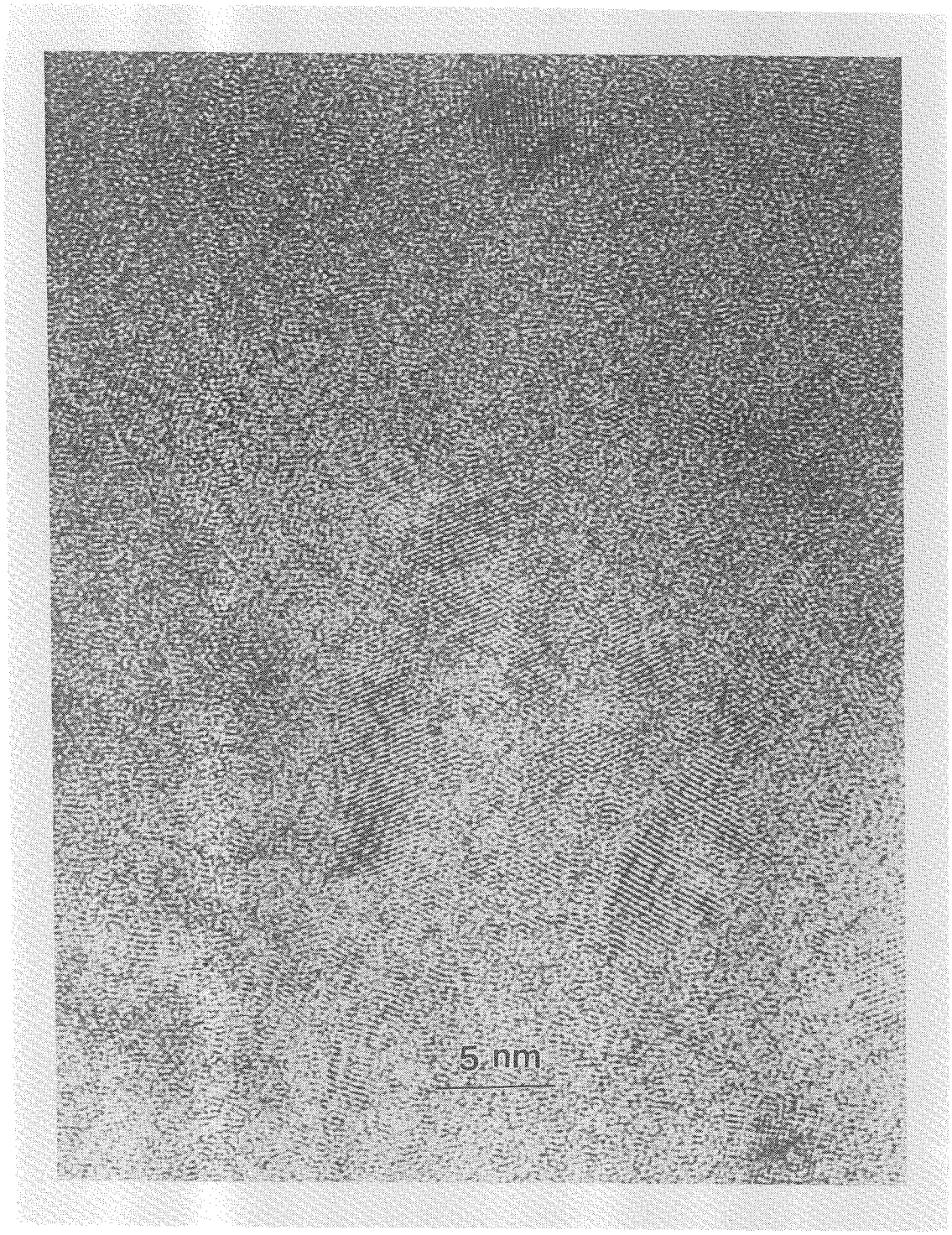

Fig. 5.4 High-resolution TEM image of $Zr_{87.5}Al_{12.5}$ sample by MA at room temperature.

Strictly speaking, the amorphization process of Al-Zr system induced by MA does not occur polymorphously. However, the chemical composition is definitely more homogeneous than that by MA at 300°C which suggests that the transition is indeed much closer to polymorphous in the sense of comparing with the high temperature milling. The atomic strain is directly associated with the structural defects in the sample. The densities of structural defects are determined by the plastic deformation introduced during MA and the recovery behavior of the sample. The lower value of atomic strain observed by MA at 300°C is expected because thermal relaxation and recovery can be enhanced when the ball milling temperature is higher. The above results suggest that the steady state obtained by ball milling at 300°C is much closer to chemical equilibrium state compared with that obtained by milling at room temperature.

Differential scanning calorimetry (DSC) has been utilized to monitor the thermal features of the two samples milled at different temperatures. The thermograms are shown in Fig. 5.5 for comparison. Besides the recovery or relaxation behavior, an exothermic peak appears at slightly different temperatures in the curves for both samples. The final products for both samples after the DSC scans have been analyzed by x-ray diffraction. The stable compound Zr_2Al and equilibrium α-Zr solid solution with sharper Bragg peaks are detected. Therefore, the exothermic peak of DSC scan corresponds to the crystallization of Zr_2Al compound and grain growth of nanometer sized α-Zr solid solution. From the discussion in the previous chapter, we know that the grain sizes of nanocrystalline supersaturated solid solution are stable under the heat treatment until reaching the temperature where the crystallization of the equilibrium

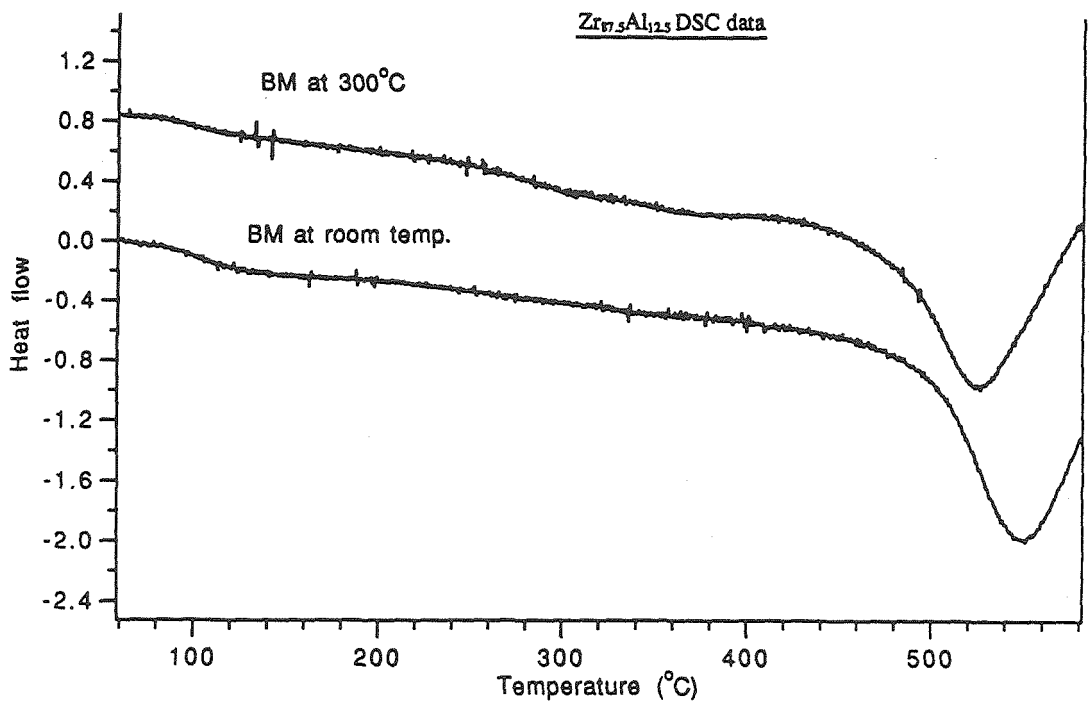

Fig. 5.5 DSC scans of ball milled $Zr_{87.5}Al_{12.5}$ samples at room temperature and 300°C respectively.

compound phase occurs. The observation of amorphous areas in both samples indicated the crystallization of amorphous phase could contribute to the DSC exothermic peak as well. The exothermic peak occurs at 525.3°C and the released enthalpy is 2.2 KJ/mole for the sample milled at 300°C, while the exothermic peak occurs at 549.3°C and the integrated enthalpy is 1.8 KJ/mole for the sample milled at room temperature. The different values of released enthalpies may be simply due to the different amount of amorphous phases existing in the two samples. The difference of peak temperatures show that the sample milled at 300°C has less thermal stability than that milled at room temperature. This may relate directly to the more pronounced phase separation for the sample milled at 300°C since the chemical equilibrium will make it easier to crystallize Zr_2Al compound in the sample portion with higher Al concentration. Therefore, the crystallization temperature of Zr_2Al compound phase appeared at lower temperature for the sample milled at 300°C with respect to the sample milled at room temperature.

5.3 Amorphous phase

To study the temperature effects on the mechanically alloyed amorphous phase, the samples with composition $Zr_{70}Al_{30}$ have been milled at room temperature and 300°C respectively. The x-ray diffractograms after mechanical alloying are shown in Fig. 5.6. The result indicated the amorphous phase can be synthesized at by ball milling at 300°C, although a trace amount of crystalline compound phase was observed from x-ray diffraction pattern. The TEM images with diffraction patterns of the two samples milled at room temperature and 300°C are given in Fig. 5.7 and Fig. 5.8 respectively. In agreement with the x-ray

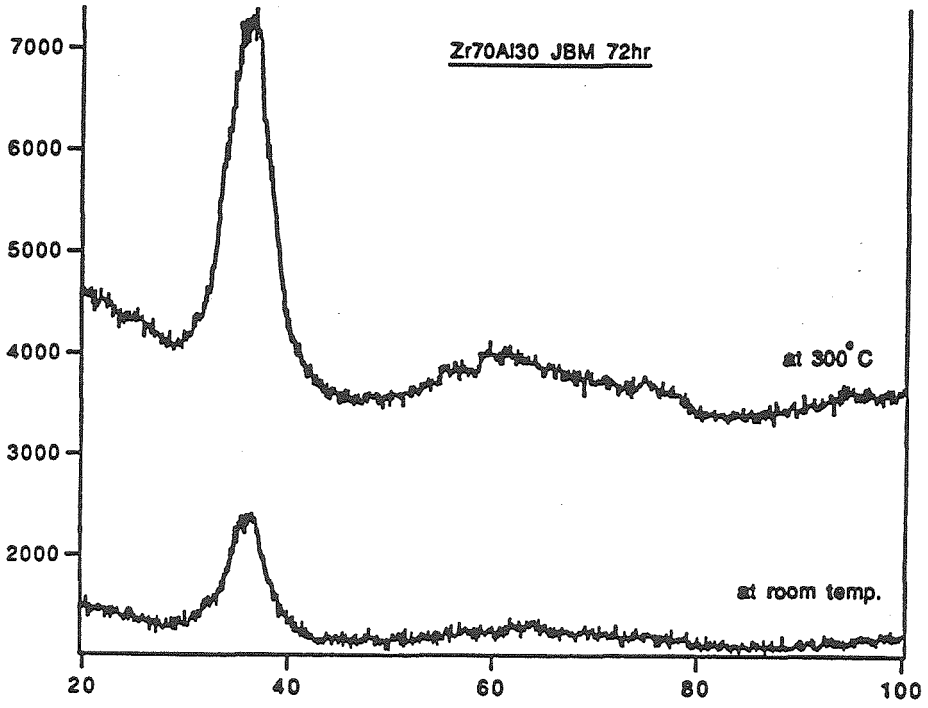

Fig. 5.6 X-ray diffractograms of $Zr_{70}Al_{30}$ samples by MA at room temperature and 300°C. Trace amounts of crystalline phase were detected for the sample milled at 300°C.

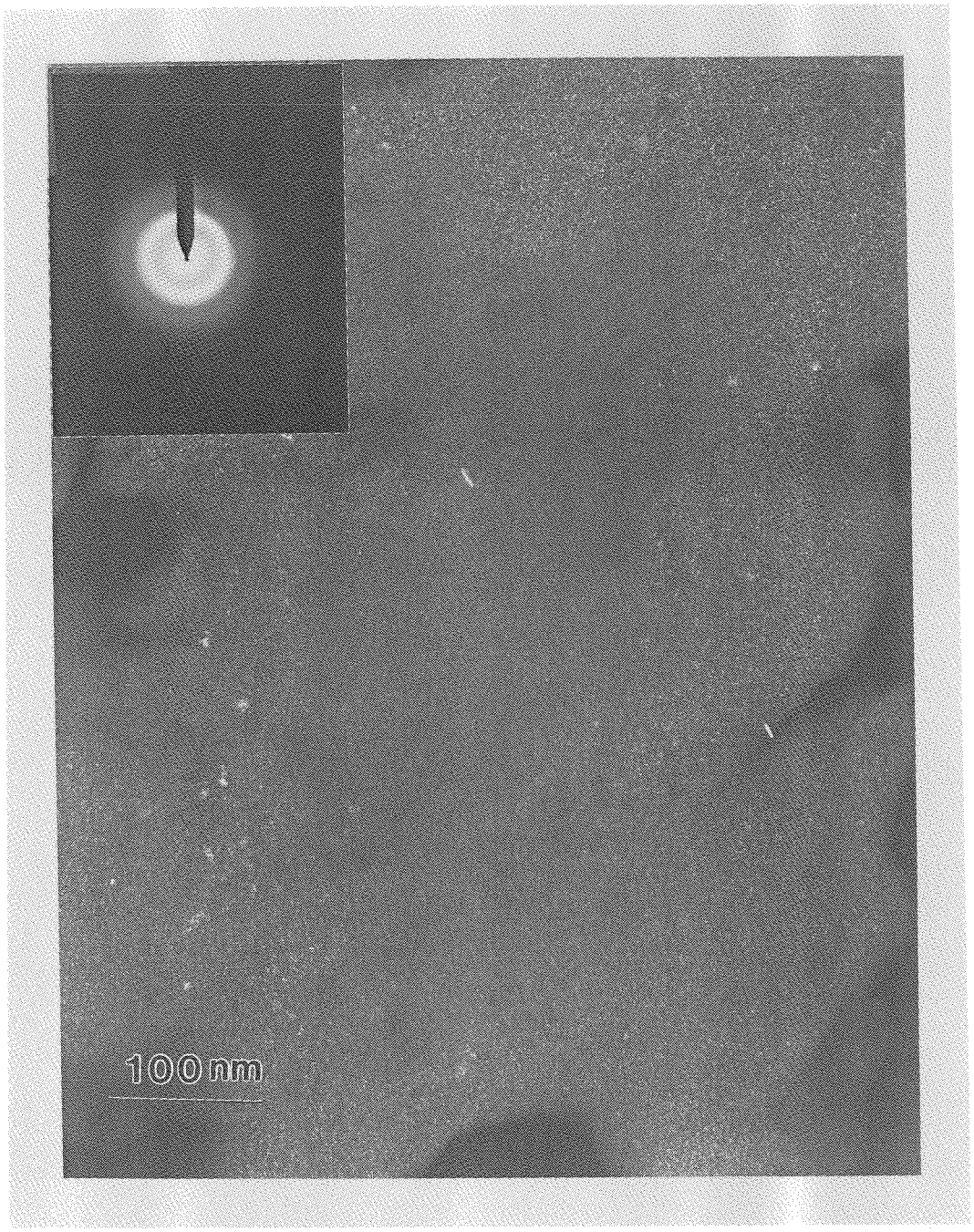

Fig. 5.7 TEM image and diffraction pattern of $Zr_{70}Al_{30}$ specimen by MA at room temperature.

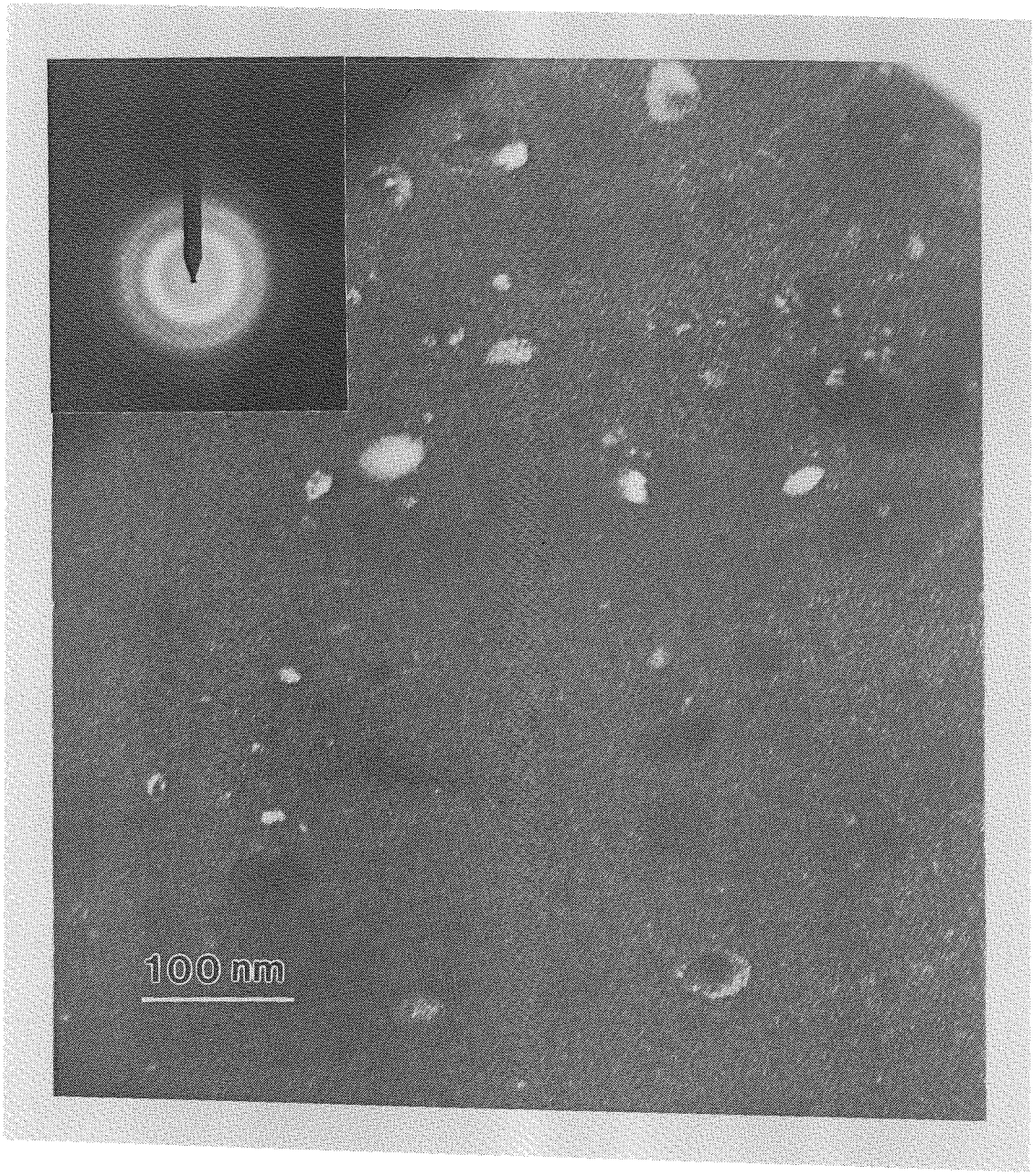

Fig. 5.8 TEM image and diffraction pattern of $Zr_{70}Al_{30}$ sample made by MA at ambient temperature=300°C.

diffraction experiment, some individual crystalline grains appear in Fig. 5.8. As we know, the higher the temperature, the easier atomic diffusion becomes. Thus, it is possible that the equilibrium compound phases are formed by milling at high temperature. On the other hand, the heavy deformation by mechanical milling is a non-equilibrium process and seems to destroy the crystalline phase simultaneously. Therefore, the formation of these crystalline grains by MA is perhaps controlled by the kinetic equilibrium between the above two factors. It is hard for these grains to grow big enough and connect each other due to the heavy mechanical deformation and chemical disordering. The crystalline grains may be created and disappear alternately during ball milling. Thermal analysis using DSC allows us to measure the heat release during the crystallization of amorphous phase. Fig. 5.9 shows the DSC curves of $Zr_{70}Al_{30}$ samples milled at room temperature and 300°C respectively. By analyzing the DSC data, Fig. 5.9(a) gives crystallization enthalpy ΔH = 4.69 KJ/mol and peak position at T = 506.7°C, while Fig. 5.9(b) gives crystallization enthalpy ΔH = 3.63 KJ/mol and peak position at T = 491.5°C. The less enthalpy value for the sample milled at 300°C could be due to the existence of the crystalline grains so that less amorphous phase crystallized during heating. Although the peak positions are different for the two scans, the starting temperatures of crystallization for the two samples are nearly the same. The peak is much more narrow for the sample shown in Fig. 5.9(b) which indicates the amorphous phase formed at 300°C is more homogeneous either in chemical composition or structure (or possibly both) so that more homogeneous nucleation occurs during the crystallization in comparison to the sample milled at room temperature. The kinetics of the crystallization reaction can

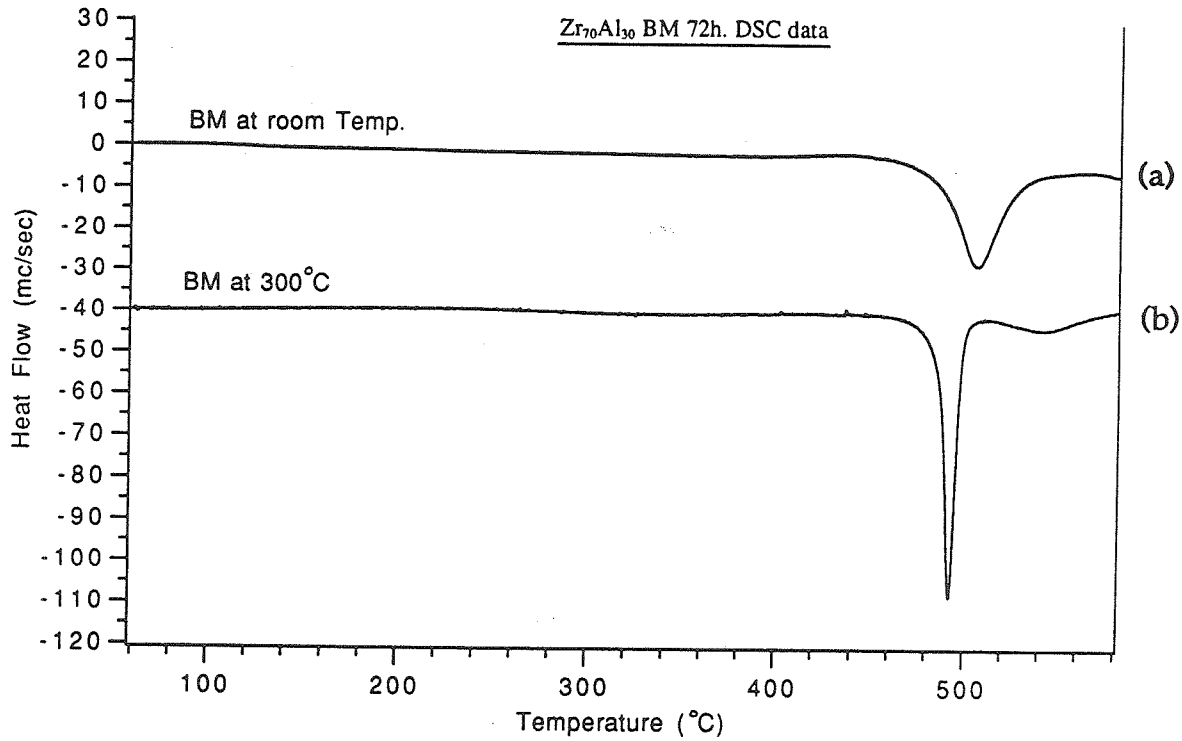

Fig. 5.9 DSC temperature scans at a constant heating rate of 20 K/min for $Zr_{70}Al_{30}$ samples synthesized by MA at (a) room temperature and (b) 300°C.

be examined by the Kissinger analysis [8] based on the peak position changes for DSC curves with different heating rates during temperature scans. The Kissinger analysis gives the activation energies of crystallization for the samples milled at room temperature and 300°C to be 3.14 ev and 3.12 ev respectively. This means that the crystallizations of both samples are basically controlled by the same mechanism. It is noticed that 3 ev is very close to the activation energy of Zr self-diffusion process. Recalling the measured microhardness data shown in Chapter 3 for the samples milled at different temperatures, I believe that a direct relationship between the hardness and the microstructures of the samples is suggested by the experiments. The microhardness of a sample with some nanocrystalline grain in an amorphous matrix has higher value than the single amorphous sample.

5.4 Summary and discussion of temperature effect

The experiments revealed that the ultimate grain size of nanocrystalline solid solution prepared by ball milling is determined by two main factors. One is the densities of structural or topological defects which are governed by the competition between the severe plastic deformation induced during mechanical alloying/milling and the recovery behavior of the materials. Another is the chemical effects of studied materials which correspond directly to the composition of the sample and the interactions among the components. For pure elemental powders, obviously, only the first factor plays a role on the final grain size achieved by mechanical milling. Generally speaking, the higher the temperature, the lower the structural defect densities due to the enhancement of the recovery behavior. Thus, the milling temperature could influence the average grain size of a

nanostructured material. For a binary or multi-component system, the chemical effects such as chemical disorder and solute segregation may also affect the microstructure of the sample. The experiments showed that the chemical effects on the average grain size also change with the milling temperature. The final grain size could be determined by the predominant factor of the above two. Therefore, the grain size of ball-milled materials could either increase or decrease with the increasing of temperature depending on the chemical composition. The experimental grain sizes of nanophase materials milled at room temperature and 300°C as functions of Al concentration are plotted in Fig. 5.10. In agreement with the above argument, the grain size obtained by milling at room temperature is smaller than that milled at 300°C for stable equilibrium solid solution, while the grain size is larger for samples milled at room temperature than that milled at 300°C for supersaturated solid solutions. The amorphous phase appears at lower Al concentration for samples milled at 300°C than those milled at room temperature which is consistent with the T_o line tendency *vs.* temperature. Both x-ray diffraction and TEM data display clearly that the supersaturated solid solution observed by mechanical alloying at 300°C can not sustain chemical homogeneity within the whole sample. This experimental result demonstrates that at least when the system was subjected to mechanical alloying at 300°C, the Al-Zr system does not amorphize by polymorphous transition as Ma *et al.* [6] concluded by MA at room temperature. In summary, the temperature effects by ball milling are: 1) The average grain size of nanocrystalline materials may change with the ball milling temperature. 2) In agreement with C. H. Lee *et al.* [9], a faster alloying reaction rate is observed for metastable phase formation if the

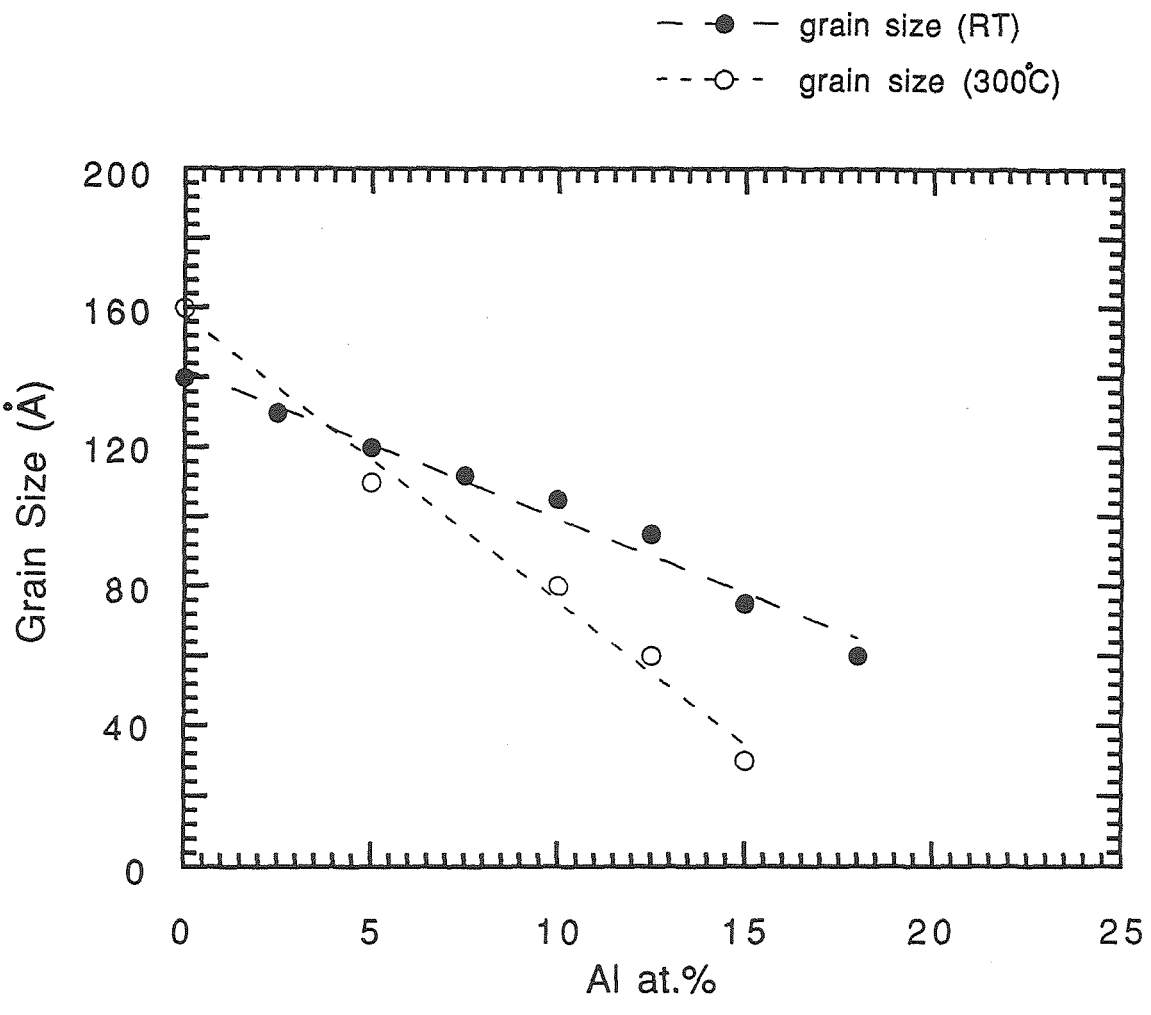

Fig. 5.10 Experimental grain size data for samples milled at room temperature and 300°C were plotted as functions of Al concentrations.

samples are milled at higher temperature. This is consistent with the solid-state reaction mechanism. 3) For the supersaturated solid solution, the steady state obtained by ball milling at higher temperature is closer to the chemical equilibrium state compared with that by milling at room temperature. 3) Amorphous phase can be synthesized by MA of aluminum and zirconium at temperatures up to 300°C, although a trace amount of crystalline compound phase is found in the amorphous matrix. The sharper DSC crystallization peak in Fig. 5.9(b) suggests the more homogeneous nucleation reaction occurs for the amorphous material formed by mechanical alloying at higher temperature.

References

[1] R. B. Schwarz, R. P. Petrich and C. K. Saw, *J. Non-Cryst. Solids* **76**, 281 (1985).

[2] E. Hellstern and L. Schultz, *Appli. Phys. Lett.* **48**, 124 (1986).

[3] C. C. Koch, *J. Non-Cryst. Solids* **117/118**, 670 (1990).

[4] F. Petzoldt, B. Scholz and H.-D. Kunze, *Mater. Lett.* **5** (7/8), 280 (1987).

[5] R. Schulz, M, Trudeau, and J. Y. Huot, *Phys. Rev. Lett.* **62** (24), 2849 (1989).

[6] En Ma and M. Atzmon, *Phys. Rev. Lett.* **67** (9) 1126 (1991).

[7] R. W. Seigle, *Annu. Rev. Mater. Sci.* **21**, 559 (1991).

[8] H. E. Kissinger., *Anal. Chem.* **29**, 1702 (1957).

[9] C. H. Lee *et al.*, *Mater. Sci. and Engin.* **A134**, 1334 (1991).

Chapter 6

Discussions of the Amorphization Mechanism by Mechanical Alloying

In this chapter, I will first review some experimental results related to the mechanism studies of phase transitions by mechanical alloying or mechanical milling, and then discuss the possible mechanisms of amorphization for mechanically alloyed Al-Zr based on the available experimental data. The emphasis is to argue the possibility of polymorphic amorphization.

As I have mentioned in the introduction of this thesis, the mechanisms of mechanical alloying/milling (MA/MM) are poorly understood. Because of the difficulty of *in situ* monitoring the ball milling process, most of the efforts on the mechanism investigations have been done indirectly by characterizing the materials and studying the property changes with ball milling time, composition or other experimental conditions. Some researches studied the possible mechanisms by comparing with a better known technique or through prediction. For examples, Yermakov *et al.*[1] have hypothesized that MA induced amorphization by a process of formation of local melts followed by rapid solidification of these melts to the amorphous phase. In contrast, Schwarz *et al.* [2] and Hellstern *et al.*[3] have argued that a solid-state reaction between ultrafine crystalline particles with fresh surfaces created by MA leads to the amorphization. In the case of amorphization of an intermetallic

compound, Koch *et al.* [4] suggested that the severe plastic deformation provided by MM generates lattice defects which cause the free energy of crystalline phase to rise above that of amorphous phase, resulting in vitrification of the intermetallic compound. More recently, in the study of mechanical milling of A15 type Nb_3Sn and Nb_3Au compounds, Di *et al.* [5] found that there are substantial similarities between the effects of ball milling and irradiation processes. The time-dependence of the change in the superconducting transition temperature is similar to that observed during irradiation by heavy particles. The change in the lattice parameter is also of the same magnitude as that found in an irradiation experiment. Both processes degrade T_c and cause an increase in the lattice parameter in the same way. The observations were in accordance with the suggestions that atomic disorder precedes amorphization. Therefore, they concluded it is very probable that continuous mechanical deformation leads to anti-site disorder as in the irradiation process. By the *in situ* thermal observation for Al-Ni ball milling system, Atzmon [6] found an exothermic, explosive formation of AlNi compound during MA of elemental powders. It was suggested that this process results in the formation of a liquid alloy, followed by cooling and solidification. Therefore, he claimed the suggested planar, gradual solid-state diffusion mechanism is not likely and melting by a chemical reaction mechanism may occur for some composition alloys. In the study of amorphization mechanism of Ni-Zr alloys, Gaffet *et al.*[7] reported there are three amorphous phases with distinct compositions and different nearest-neighbor distances found by ball milling. Two out of these three were formed by the polymorphous transformation from the crystalline compound with the same composition. Namely, the crystalline

compounds were first synthesized during MA and then transform to amorphous phase by further milling. Hence, they concluded that amorphization by mechanical alloying is not only a simple reaction of diffusion-induced amorphization and sometimes amorphization may undergo a polymorphous transition from an intermetallic compound formed by mechanical allying. For the same Ni-Zr system, by probing the Ni content of Zr crystallites as a function of milling time using Auger spectroscopy, Schulz *et al.*[8] reported the direct measurements of the interdiffusion which takes place during amorphization of Ni-Zr by the MA of pure elemental powders. On the basis of the variation of the Ni concentration in Zr and a simple interdiffusion model, an effective local temperature of 180°C is estimated in the powder at the collision site. Therefore, they concluded a solid state amorphization mechanism and suggested the large heat of mixing is indeed the driving force for the reaction. I also did some similar experiments with Ni-Zr for comparison while studying the amorphization of Al-Zr by MA because Ni-Zr is a well-studied system for amorphization [9,7,10] and almost all its thermodynamic data are known [11,12]. The available information makes it possible to interpret the experimental data more efficiently for a better understanding of the transition mechanism. However, the x-ray diffraction analysis indicates the lattice parameters of α-Zr solid solutions are constant after MA for Ni-Zr samples with different average Ni concentrations in the mixed powders. The increasing amount of amorphous phase with the increasing of the average Ni concentration is also seen from x-ray spectra. Therefore, the amorphous phase can be clearly concluded in Ni-Zr by MA under the metastable two-phase equilibrium. In consistency with my x-ray diffraction

experiments for Ni-Zr system, Schultz and Hellstern *et al.*[13] found the almost constant behavior of superconducting temperature T_c for all the alloys with compositions x_{Al}<0.25 which indicates the existence of two-phase equilibrium. From the above-selected reviews of the mechanism studies related experiments, it is quite evident that the phase transition mechanisms by MA process are complex and very often depend on the studied specific system.

It has been noticed that some interesting mechanisms of crystal-to-amorphous phase transition has been reported in recent years for an Al-Zr system with different synthesis methods. For instance, by studying the amorphization of intermetallic compound Zr_3Al during room temperature bombardment with 1.0 Mev Kr^+, Rehn and Okamoto *et al.* [14] found a large (about 50%) elastic softening and dilatation strain (about 3%) due to disordering precedes the onset of amorphization. This experiment provides experimental support to Johnson's [15] idea about an elastic instability as a mechanism of crystal-to-amorphous phase transformation. In comparison with the irradiation induced amorphization, the hydrogen induced crystal to glass transformation in Zr_3Al was studied by Meng *et al.*[16]. They found the predominant effect of hydrogen absorption in ordered Zr_3Al is a substantial lattice expansion with no appreciable loss in the crystalline long-range order. TEM reveals apparent homogeneous nucleation of the amorphous phase, and striking similarities to martensitic microstructure. The same amount of lattice expansion in both irradiation and hydriding before amorphization indicates that volume expansion could be a common measure of the crystal instability induced by solid state techniques. In the following, I would like to discuss the possible mechanisms of

amorphization for Al-Zr system induced by MA based on the Gibbs free energy diagram. Fig. 6.1 is a schematic diagram of Gibbs free energy curves for the Al-Zr binary system. In the diagram, α represents the α-Zr solid solution phase. A, B, and C represent the three intermetallic compound phases Zr_3Al, Zr_2Al and Zr_3Al_2 respectively. The x-ray diffraction data indicated that after MA of aluminum and zirconium powder mixtures, none of the above thermodynamically stable compounds are formed. The Gibbs free energy curve tells us the crystalline α-Zr phase can lower its free energy by incorporating Al-atoms up to a certain concentration C'. At this concentration, the crystal is in metastable equilibrium with the amorphous phase of composition C'' given by the common tangent construction. Increasing the Al concentration C further, the energy of the crystalline α-Zr phase increases and a driving force $\Delta G=\Delta G(C)$ develops for the formation of amorphous phase. So, it is possible that for samples at any given composition $C' \le x_{Al} \le C''$, the final products are the coexistence of α-Zr and amorphous phase. Obviously, the amount of each phase is controlled by the level rule and the lattice parameter of α-Zr solid solution will be a constant determined by the composition C'. If this turns out to be the case during MA, the amorphization processing of the system is under a metastable two-phase equilibrium. To nucleate the amorphous phase, a critical nucleus has to be formed which has a composition different from the crystalline α-Zr solid solution phase. If such compositional fluctuations are prohibited due to the low processing temperature such as MA, the solubility may be extended up to a critical value C^* at which point the free energies of α-Zr phase and amorphous phase become equal and no nucleation barrier exists

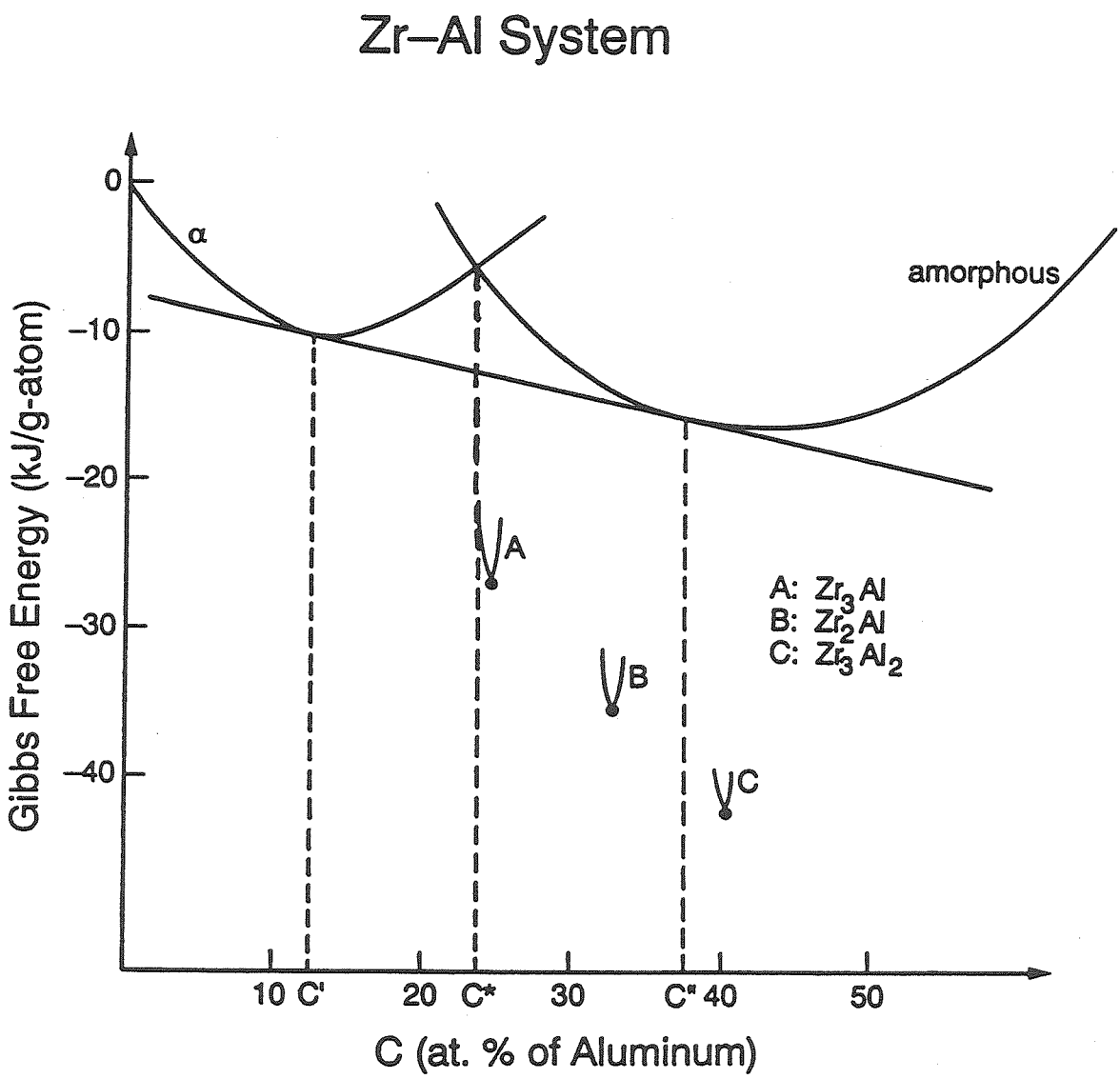

Fig. 6.1 The schematic Gibbs free energy diagram of Al-Zr binary system.

so that the crystal becomes unstable and undergoes a catastrophic transition to a metallic glass[17]. If this turns out to be the case for the formation of an amorphous phase, the mechanism of amorphization by MA undergoes polymorphous constraints. It is easy to distinguish the two amorphization paths schematically. Practically, however, it is often ambiguous to conclude the amorphization mechanism is due to the complexity of the real transformation path and the system error of experiments.

In the earlier studies[18], based on our x-ray diffraction data, experimental specific heat behavior and thermodynamic arguments, we proposed the possibility of amorphization of α-Zr in Al-Zr system by MA may be viewed as a compositionally induced melting transition when the crystal is driven outside of its own stability range. This chemically induced melting transition has been hypothesized by Fecht and Johnson [17] on the basis of polymorphous phase diagrams and kinetic constraints imposed on the system as long as the formation of equilibrium phase is kinetically suppressed. We have also noticed that the observed volume increasing between crystalline and amorphous at the transition composition is about 3% which is the same as that required for glass formation of ion-irradiation and hydriding, suggesting a common feature among different solid state reaction methods. For the same Al-Zr system, based on the lattice parameter changing with composition obtained by x-ray diffraction and the released enthalpy changing with composition measured by DSC, Ma and Atzmon [19] claimed a calorimetric evidence for polymorphous constrains on the amorphization process induced by MA. They believe the mechanism of amorphous phase formation in Al-Zr by MA is determined by polymorphous constraints, not by nucleation and growth under

metastable two-phase equilibrium. Their x-ray spectra for powders ball-milled for 24 hours [20] is shown in Fig. 6.2. As described in their paper, (a) is hcp solid solution $Zr_{90}Al_{10}$ and (b) is amorphous phase $Zr_{80}Al_{20}$. By examining their x-ray diffraction patterns and the released enthalpy discussions in Chapter 3, I suspect there is no convincing evidence to make the conclusion about the polymorphous transition mechanism. For instance, it is hard to determine whether there is a small amount of amorphous phase in the sample shown in Fig. 6.2(a), especially when the three main Bragg peaks of hcp solid solution could overlap with the broad diffused amorphous peak. Even for the amorphous sample shown in Fig. 6.2(b), it seems possible to have a trace amount of crystalline phase in the sample. It is not reliable to conclude the mechanism of phase transition simply by the calorimetric evidence on the basis of both theoretical and experimental concerns. However, the lattice parameter of α-Zr decreases with the increasing of the average Al concentrations of the mixed powders that indicates the increasing of Al solubility in the α-Zr solid solution by MA, although one can not ensure the lattice parameter vs. composition plot does exactly follow the ideal solution model within the whole composition range $x_{Al} < 18 at.\%$ due to the existence of the big error bars of experimental data as discussed in Chapter 3. Very recently, in consistence with our specific heat measurement, Ettl *et al.* [21] have seen quite interesting behavior happen to the Debye temperature of mechanically alloyed Al-Zr materials. The results show the Debye temperature Θ_D drops to a minimum at the boundary between crystalline solid solution and amorphous phase compositions. Thus, not like the above-mentioned Ni-Zr system, the amorphization behavior of Al-Zr by MA is apparently unusual

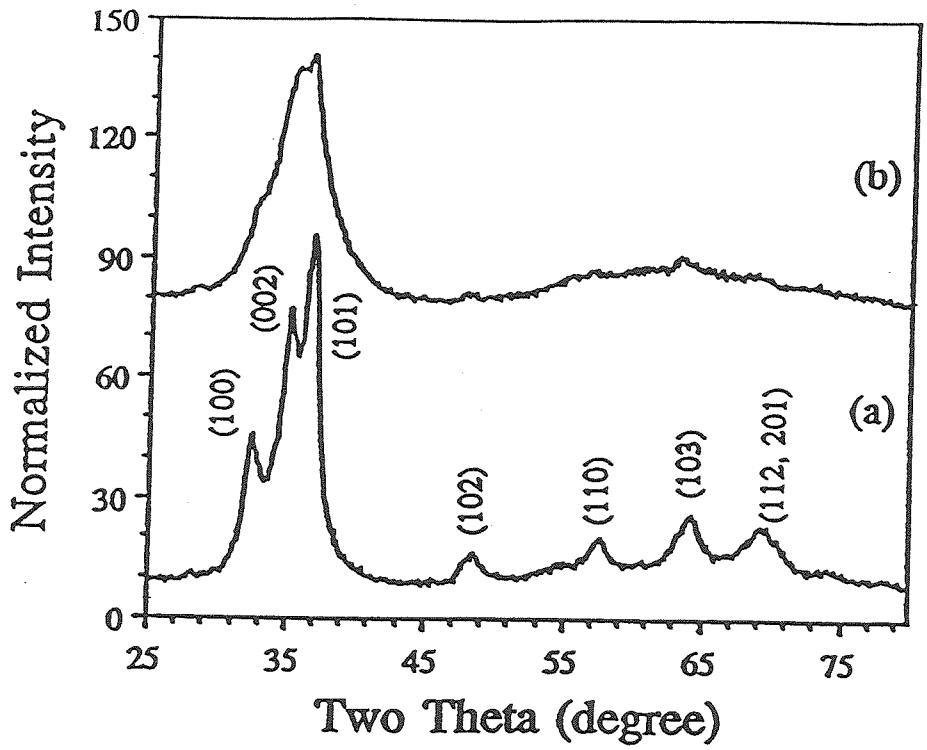

Fig. 6.2 X-ray diffraction spectra for powders ball-milled for 24 hours, showing formation of (a) HCP solid solution in $Zr_{90}Al_{10}$ and (b) amorphous phase in $Zr_{80}Al_{20}$ [20].

and ambiguous. It is hard to conclude the exact mechanism of amorphization by MA with the increasing of Al concentration.

The formation of amorphous phase for solid state samples is often detected by x-ray diffraction first. This method, however, does not always produce unambiguous results for amorphous phase formation studies as the problem has been mentioned above. Transmission electron microscopy (TEM) makes it possible to observe the amorphous phase unambiguously. A high-resolution TEM image of sample $Zr_{87.5}Al_{12.5}$ after ball milling at room temperature is shown in Fig. 6.3 where both nanocrystalline and amorphous phases were observed. Fig. 6.4 shows another amorphous area found in the sample and we see clearly the amorphous phase exhibits a short-range order feature. It is easy to understand the reason for the formation of an amorphous phase. The process starts with the pure Al and Zr elemental powders, so a concentration gradient of Al could exist between the ultrafine crystalline layered samples created by MA. The local composition of the sample may deviate from the average composition of the initially mixed powders. If the local Al concentration is near or larger than 18 at.%, the amorphous phase can be synthesized. The amorphous phase will be relatively stable as long as it is formed. I think, it is time to ask about the exact definition or requirement for the polymorphous transition since the conclusion certainly depends on how big or in what dimension the composition and phase fluctuations can be allowed. If the polymorphic amorphization is defined absolutely from a single nanocrystalline phase to a single amorphous phase at one composition, the above TEM observations rule out the amorphization mechanism by polymorphous constraints. However, it is worth noting that only very small and thin areas can be

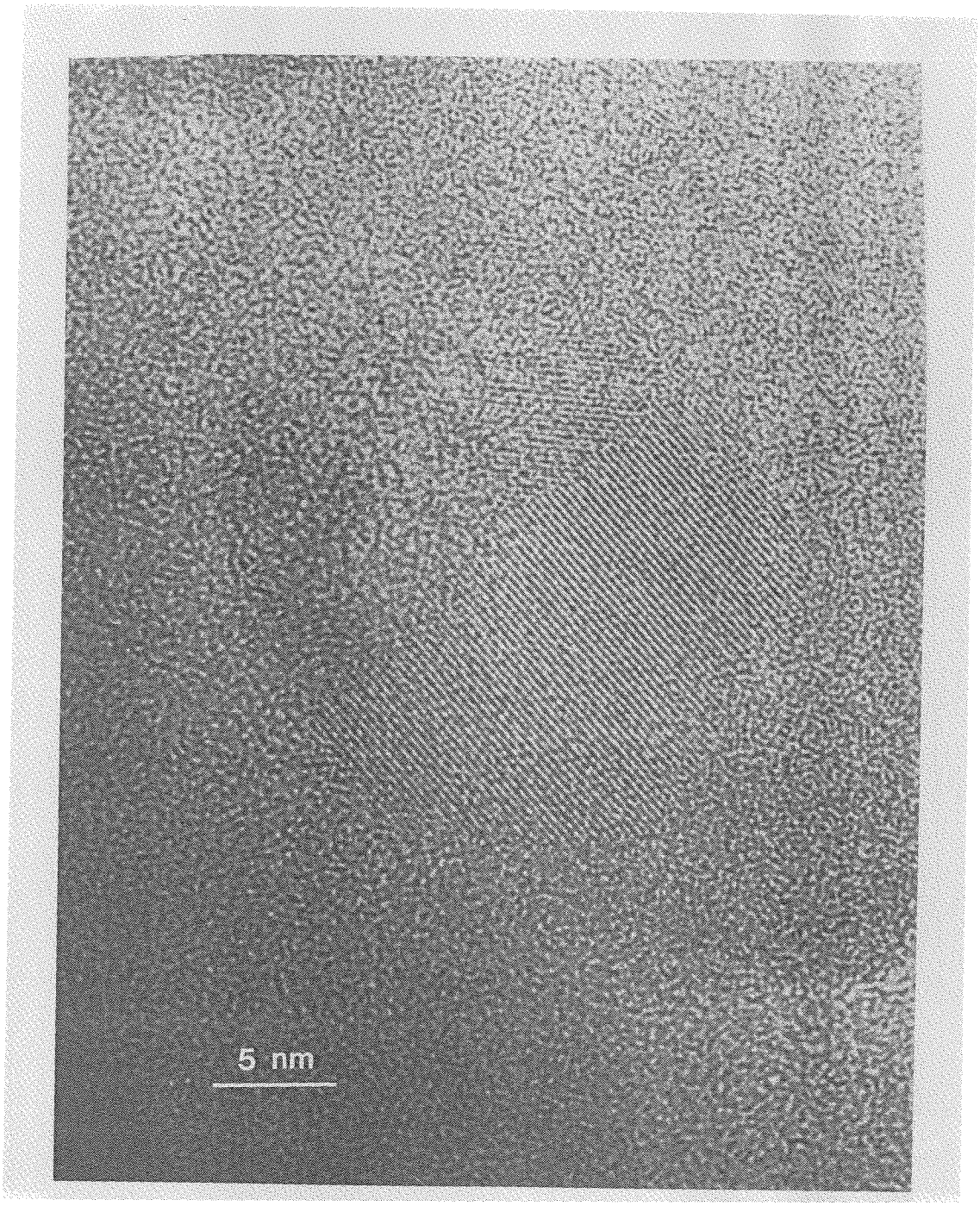

Fig. 6.3 High-resolution TEM image of $Zr_{87.5}Al_{12.5}$ sample after ball milling at room temperature. Both nanophase area and amorphous area were observed.

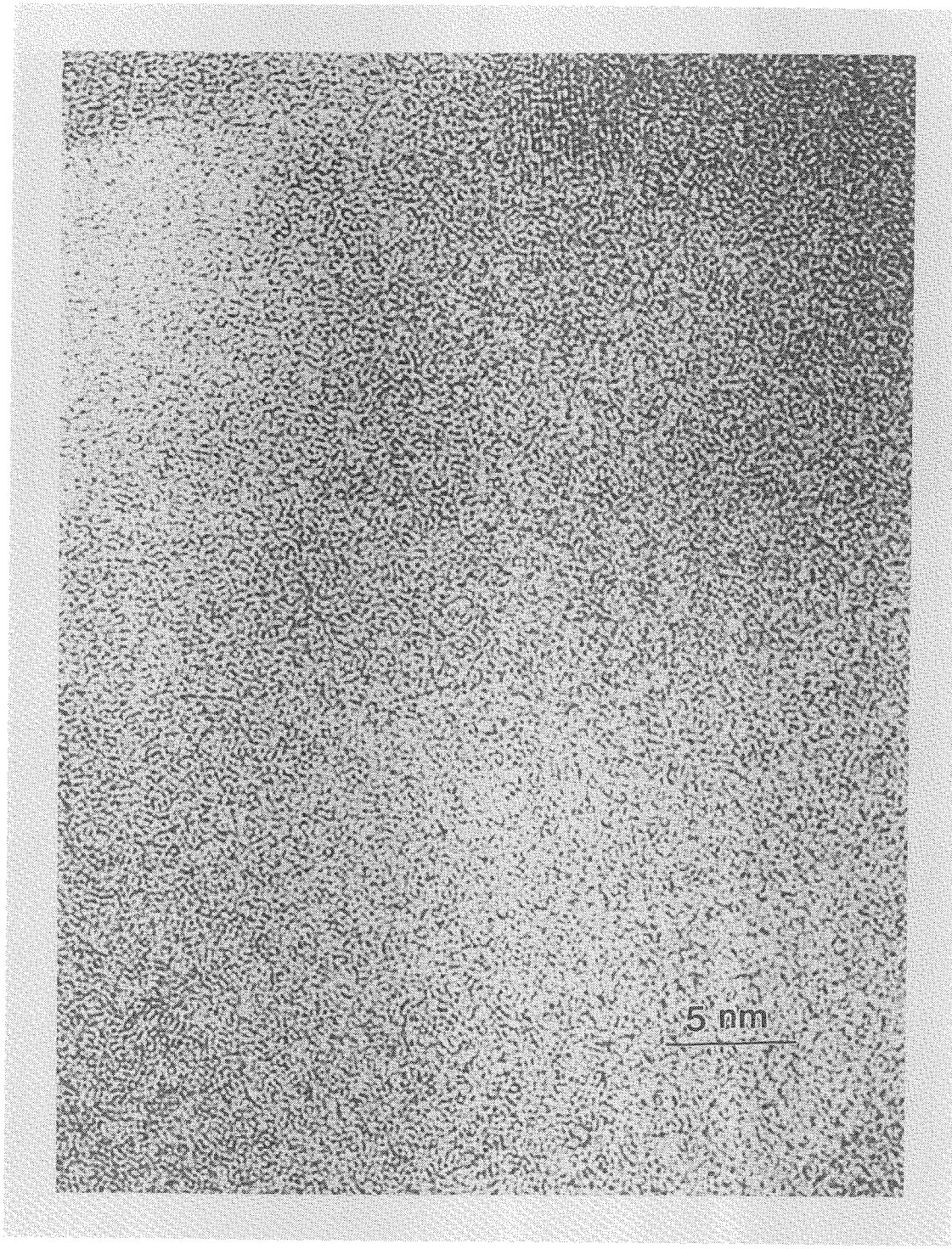

Fig. 6.4 Another amorphous area was found in the same sample as Fig. 6.3.

studied with TEM. It is difficult to obtain a statistical average result for samples prepared by ball milling. The behaviors of the specific heat, the Debye temperature, the lattice parameter, and the released enthalpy at the boundary between solid solution and amorphous phase compositions somehow suggested the tendency of a polymorphous transition, although it is not probable that the entire sample transforms simultaneously to the amorphous phase due to fluctuations of the local Al concentration. Further experiments which could reveal the detail and average information on the microstructure level such as small angle scattering may be helpful for a better understanding on the mechanism of amorphization in this case.

In order to study the mechanism of amorphous phase transformation from α-Zr solid solution by MA systematically, the experiments under different conditions have been performed as well.

6.1 Amorphization vs. composition at 300°C ambient milling temperature

As discussed in Chapter 5, the inhomogenity in the chemical compositions is found for the $Zr_{87.5}Al_{12.5}$ sample after ball milling at ambient temperature 300°C. There is only 8 at.% of Al dissolved in the crystalline α-Zr solid solution phase from x-ray analysis. In Fig. 6.5, the high-resolution TEM image of the $Zr_{87.5}Al_{12.5}$ sample by mechanical alloying at 300°C shows the presence of both the nanocrystalline phase and the amorphous phase. In agreement with the x-ray analysis, the chemical analyses from EDX also find the different Al concentrations within the crystalline grain and the amorphous area. Therefore, it is easy to conclude the amorphization by MA at 300°C can not be a polymorphous transition.

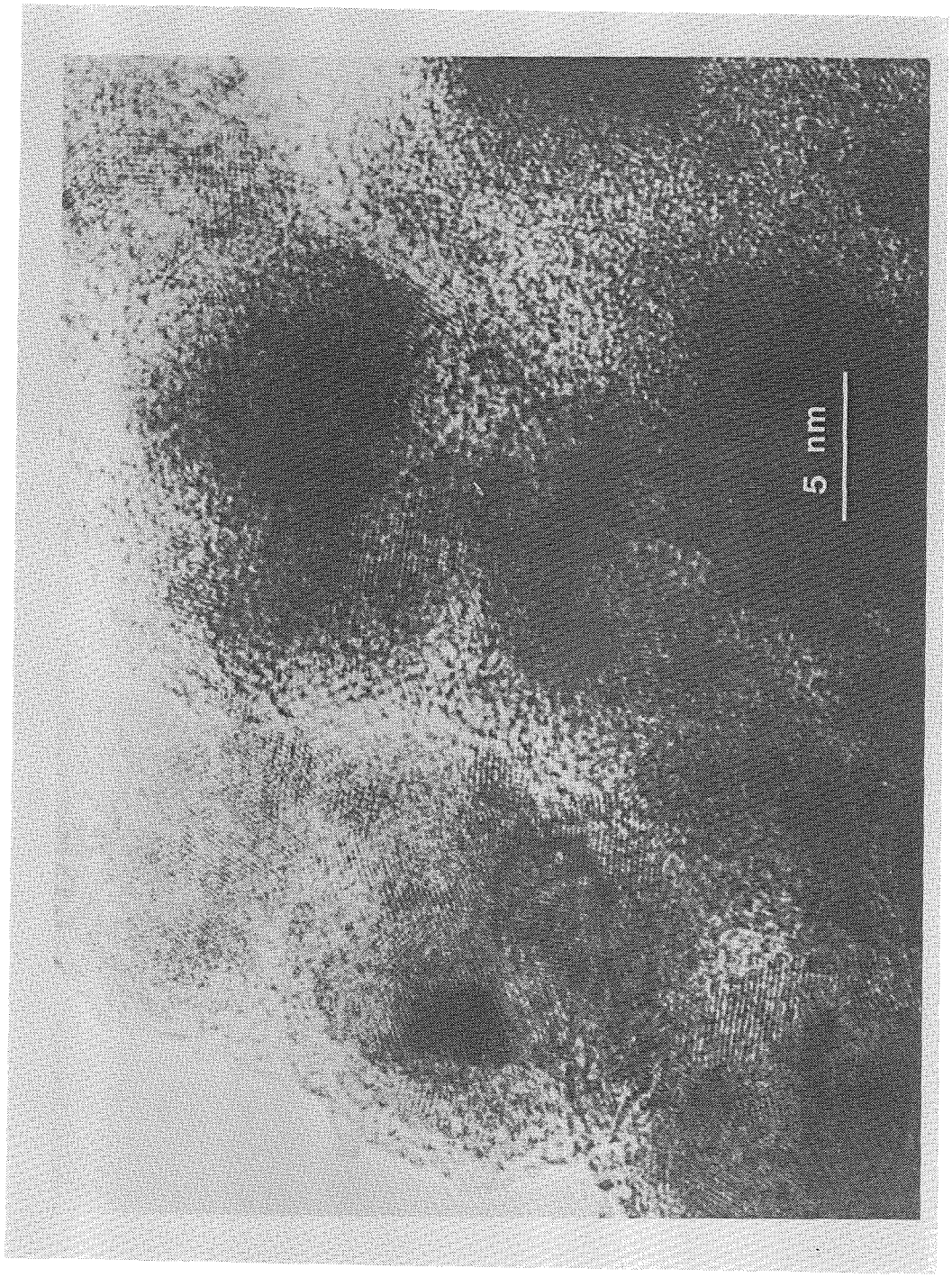

Fig. 6.5 High-resolution TEM image of $Zr_{87.5}Al_{12.5}$ sample after ball milling at 300°C.

By examining the TEM picture, we can suppose there is a mechanism of the crystal-to-amorphous phase transition since it is similar to the other solid state amorphization reactions such as Zr_3Rh hydriding [22] in which the amorphization is seen to form at the grain boundaries and subsequently grow into the crystal grains. As ball milling proceeds, first a layered structure is formed which is refined further with the increased processing time. As indicated by x-ray diffraction, the Al atoms are dissolved in the α-Zr due to the large negative enthalpy of mixing for Al-Zr (about -50 KJ/mole) which leads to the development of a concentration profile of Al in Zr. The high concentration of Al should be at the boundary between Al and Zr powders. Hence, the amorphous phase would like to nucleate heterogeneously at grain boundaries since the local Al concentrations at the boundaries could be higher than that in the α-Zr grains. The high milling temperature 300°C is certainly helpful for the diffusion of Al atoms and the chemical equilibrium may be reached. Therefore, the amorphous phase transition is determined by the metastable two-phase equilibrium. The amount of amorphous phase should be controlled by the level rule. The deviation of Al solubility from the thermodynamic equilibrium value in α-Zr may be due to the existence of various defects in the nanocrystalline solid solution formed by mechanical alloying process.

6.2 Amorphization vs. milling time for a given composition

As we know from Chapter 3, a complete amorphous phase can be synthesized by MA for the samples with compositions $x_{Al} > 18$ at. %. Fig. 6.6 shows the x-ray diffraction results for the samples with compositions $Zr_{78}Al_{22}$ and $Zr_{70}Al_{30}$ after ball milling for 48 hours and 72 hours respectively. I think the two x-ray spectra for $Zr_{78}Al_{22}$ and $Zr_{70}Al_{30}$ after 48

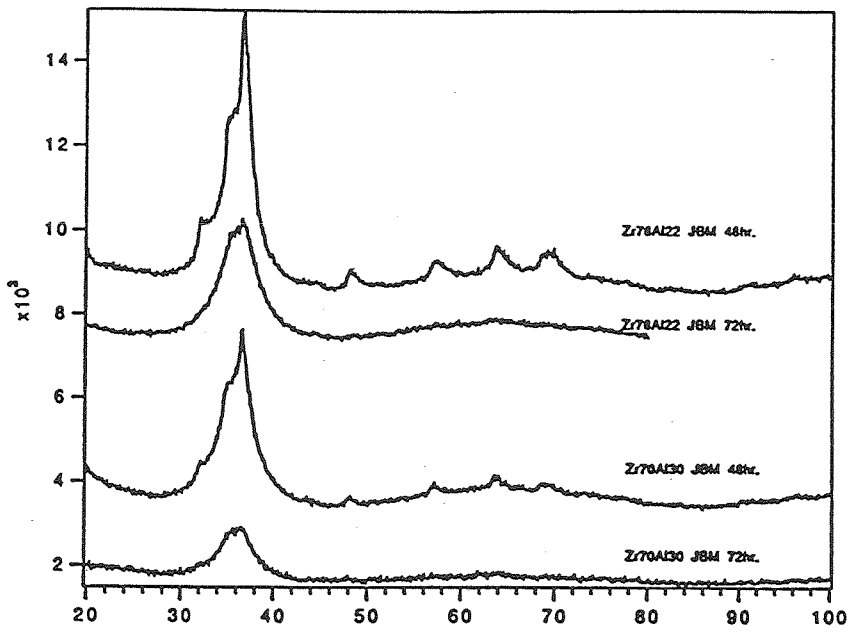

Fig. 6.6 X-ray diffraction results for the samples $Zr_{78}Al_{22}$ and $Zr_{70}Al_{30}$ after ball milling for 48 hours and 72 hours.

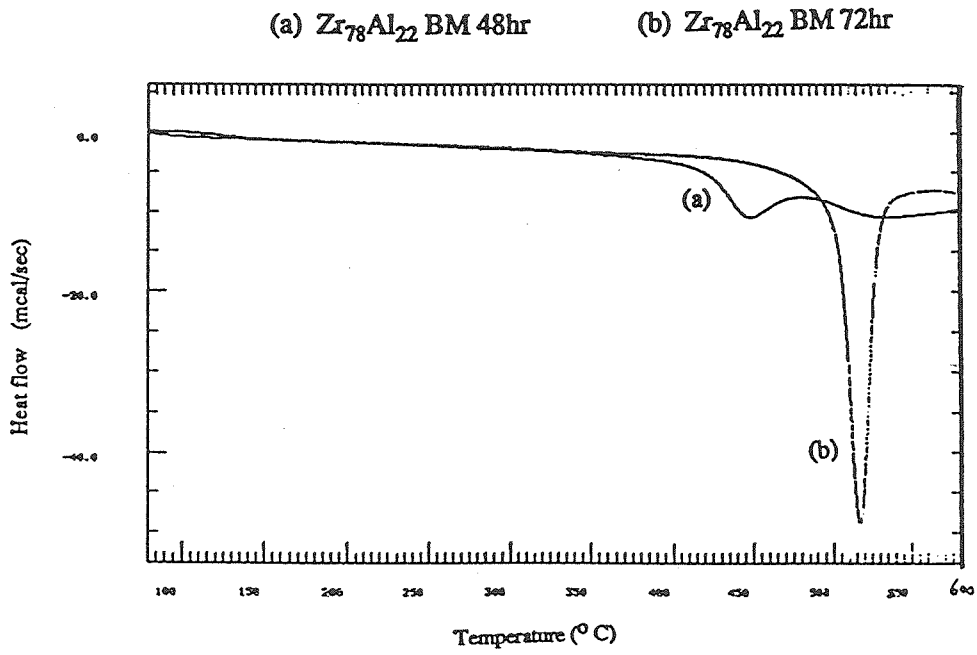

Fig. 6.7 The DSC scans at a constant heating rate of 20 K/min for the $Zr_{78}Al_{22}$ samples after different milling time: (a) 48 hr. and (b) 72 hr.

hours ball milling demonstrate convincingly that there are partial amorphous phases formed in both samples. The DSC scans at constant heating rate (20 K/min) for $Zr_{78}Al_{22}$ samples after 48 hours and 72 hours mechanical milling are shown in Fig. 6.7. Two exothermic peaks are seen in the DSC curve upon heating to 600°C for the partially amorphized sample as shown in Fig. 6.7(a). The structure analysis indicated the first peak is corresponding to the crystallization of amorphous phase and the second is related to the grain growth of nanocrystalline solid solution. After the sample becomes complete amorphous phase, the DSC scan has only one sharp exothermic peak which is associated with the crystallization of amorphous phase as shown in Curve (b). The DSC results agreed well with the x-ray diffraction data. It was noticed that the crystallization peaks in curves (a) and (b) appear at different temperatures. The different nucleation mechanism for amorphous phase in the two samples may be responsible for the temperature difference. For the sample with two phases, the nucleation of amorphous phase could be heterogeneous due to the existence of grain boundaries or phase interfaces in the materials so the crystallization occurs at lower temperature. Another influence for the crystallization temperature could come from the composition differences of amorphous phases in the two samples. The experiment suggested in this case that the amorphization doesn't occur simultaneously by the polymorphous transition. The amorphous phase is formed by nucleation and growth to the whole sample through the two-phase equilibrium.

In conclusion, it is perhaps impossible for the MA process to obtain a strictly polymorphic amorphization due to the concentration gradient existing between the pure elemental powders (or the fluctuation of local

composition). It also turns out that the mechanisms of phase transition by MA/MM process are complex and often depend on not only the particular studied materials but also the exact experimental conditions.

References

[1] A. Y. Yermakov, Y. Y. Yurchikov and V. A. Barinov, *Phys. Met. Metallogr.* **52**, 50 (1981).

[2] R. B. Schwarz, R. P. Petrich and C. K. Saw, *J. Non-Cryst. Solids* **76**, 281 (1985).

[3] E. Hellstern and L. Schultz, *Appli. Phys. Lett.* **48**, 124 (1986).

[4] C. C. Koch, O. B. Cavin *et al.*, *Appl. Phys. Lett.* **43**, 1017 (1983).

[5] L. M. Di, *et al.*, J. Less-Common Metals **168**, 183 (1991).

[6] M. Atzmon, *Phys. Rev. Lett.* **64** (4), 487 (1990).

[7] E. Gaffet, N. Merk *et al.*, *J. Less-Common Metals* **145**, 251 (1988).

[8] R. Schulz, M, Trudeau, and J. Y. Huot, *Phys. Rev. Lett.* **62** (24), 2849 (1989).

[9] L. Schultz, E. Hellstern and A. Thoma, *Europhys. Lett.* **3** (8), 921 (1987).

[10] W. Meng, Ph. D. Thesis, California Institute of Technology, (1988).

[11] P. Nash and C. S. Jayanth, *Bull. Alloys Phase Diagrams* **5** (2), 144 (1984)

[12] J. G. Gachon, M. Dirand and J. Hertz, *J. Less-Common Metals* **92**, 307 (1983).

[13] L. Schultz, E. Hellstern and A. Thomä *et al.*, *Europhy. Lett.* **3**, 921 (1987).

[14] L. E. Rehn, P. R. Okamoto *et al.*, *Phys. Rev. Lett.* **59**, 2987 (1987).

P. R. Okamoto, L. E. Rehn *et al.*, *J. Less-Common Metals* **140**, 231 (1988).

[15] W. L. Johnson, *Prog. Mater. Sci.* **30**, 81 (1986).

[16] W. J. Meng, P. R. Okamoto *et al.*, *Appl. Phys. Lett.* **53** (19), 1820 (1988).

[17] H. J. Fecht and W. L. Johnson, *Nature* **334**, 50 (1988).

[18] H. J. Fecht, G. Han, Z. Fu and W. L. Johnson, *J. Appl. Phys.* **67** (4) 1744 (1990).

[19] En Ma and M. Atzmon, *Phys. Rev. Lett.* **67** (9) 1126 (1991).

[20] E. Ma and M. Atzmon, Presented at the International Symposium on Mechanical Alloying, May 7-9, Kyoto, Japan, (1991).

[21] C. Ettl et al., *Universität Augsburg, Germany,* Private communication.

[22] X. Yeh, Ph. D. Thesis, California Institute of Technology, (1986).